

ULTRA HIGH SPEED RAINBOW SCHLIEREN DEFLECTOMETRY  
FOR WHOLE FIELD ACOUSTIC MEASUREMENTS  
IN SUPERSONIC JETS

by

WILLIAM DANIEL MITCHELL

AJAY K. AGRAWAL, COMMITTEE CHAIR  
ROBERT P. TAYLOR  
SEMIH M. OLCMEN

A THESIS

Submitted in partial fulfillment of the requirements  
for the degree of Master of Science  
in the Department of Mechanical Engineering  
in the Graduate School of  
The University of Alabama

TUSCALOOSA, ALABAMA

2013

Copyright William Daniel Mitchell 2013  
ALL RIGHTS RESERVED

## ABSTRACT

The goal of this research is to advance the field of noise measurement techniques to better understand the fundamental guiding principles of noise generation. This is accomplished in this study by demonstrating the capabilities of Ultra-High Speed Rainbow Schlieren Deflectometry (UHS-RSD) technique to visualize and quantify, in real-time, sound waves propagating from a supersonic cold air jet. Basic optical theory states that light rays passing through varying density transparent medium undergo deviations from their original paths because of refraction. An experimental setup was developed to direct parallel white light rays through a supersonic air jet. UHS-RSD technique employs aforementioned phenomena and enables mapping the light deflection angles, a measure of deviation of a light ray from its original path. Ray deflection angle mapping process is realized through variation in color (hue) between a schlieren image with and without test medium. Since all information in the field of view can be acquired in real time, this technique provides a means to determine full field of view scalar properties of any transparent flow. The current experiment captures sound waves emanating from a supersonic cold air jet at high spatial and temporal resolution, while still maintaining the hue sensitivity needed to detect the small pressure fluctuations characteristic of sound waves. The sound probe data showing general maximum sound generation could be employed to support the visual UHS-RSD data where pressure gradient waves are seen propagating from the same jet noise source. Initial analysis reveals the UHS-RSD system to

capture the acoustic field properties matching previous studies. Mach wave fronts are generated in small packets of 2 to 10 waves with small intermittency window. This research has shown that the UHS-RSD technique has the capability of capturing acoustic waves emanating from supersonic jets. A detailed discussion is presented on how the RSD system has been optimized to significantly improve sensitivity and the signal to noise ratio.

## DEDICATION

This thesis is dedicated to my mother, “Katherine Sharp Kirkpatrick”.

## LIST OF ABBREVIATIONS

LDV	Laser Doppler Velocimetry
PIV	Particle Image Velocimetry
OD	Optical Deflectometry
RSD	Rainbow Schlieren Deflectometry
UHS	Ultra high-speed
$\varepsilon$	Transverse deflection angle
$\delta$	Normalized refractive index difference
$f_1$	Focal length of collimating lens
$f_2$	Focal length of de-collimating lens
RGB	Color format that is based on color level of red, green, or blue present
HSI	Color format that is based on color hue, saturation, and intensity
$\Theta$	Transverse deflection angle
x,y,z	Global coordinates
r	Radial coordinate

$t$	Time
$\eta$	Local refractive index
$\eta_o$	Refractive index of the surroundings
$D_{ij}$	Geometric coefficient
$K$	Gladstone-Dale constant
$T$	Normalized Temperature along jet centerline
$P$	Normalized Pressure along jet centerline
$\rho$	Density of jet fluid
$T_e, P_e, \rho_e$	Thermodynamic property at orifice exit
$\gamma$	ratio of specific heats
$X$	Transverse position
$H$	Hue value
$H_b$	Hue value of background image
RMS	Root mean square
FFT	Fast Fourier transform
dB	Sound decibel level
C-D	Converging-Diverging [Nozzle]

Z/D axial location normalized by the jet diameter

R/D radial location normalized by the jet diameter

LED Light emitting diode

## ACKNOWLEDGMENTS

I am pleased to have this opportunity to thank my family, friends, colleagues, and faculty members who have lent their support and encouragement. I am very grateful of Dr. Ajay K. Agrawal, the chairman of this thesis, for sharing his expertise in his technical field. I would like to thank The Graduate Assistantship in Areas of National Need (GAANN) fellowship for supporting me during the course of my master's studies.

## CONTENTS

ABSTRACT.....	ii
DEDICATION.....	iv
LIST OF ABBREVIATIONS.....	v
ACKNOWLEDGMENTS .....	viii
LIST OF TABLES.....	xii
LIST OF FIGURES .....	xiii
1 JET NOISE RESEARCH .....	1
1.1 Introduction.....	1
1.2 Overview and Objectives.....	4
2 RAINBOW SCHLIEREN DEFLECTOMETRY.....	8
2.1 Rainbow Schlieren Theory and Methodology .....	8
2.2 Key Mathematical Equations.....	11
2.3 Rainbow Filter and Filter Calibration.....	13
2.4 Basic Analysis of Experimental Images .....	15

2.5	Past Applications of RSD .....	15
3	EXPERIMENTAL SETUP.....	34
3.1	Overview.....	34
3.2	Diagnostic Challenges .....	35
3.3	Equipment Details, Specification, and Setup.....	36
	3.3.1 <i>Flow System</i> .....	36
	3.3.2 <i>UHS-RSD System</i> .....	38
3.4	UHS-RSD System Optimization.....	40
	3.4.1 <i>Light Source</i> .....	40
	3.4.2 <i>Slit Aperture</i> .....	41
	3.4.3 <i>Collimating Lens</i> .....	41
	3.4.4 <i>De-Collimating Lens</i> .....	42
	3.4.5 <i>Filter Selection</i> .....	43
	3.4.6 <i>Camera Lens Selection</i> .....	43
	3.4.7 <i>Framing Rate</i> .....	43
3.5	Optical Procedures .....	44
	3.5.1 <i>Optical Alignment</i> .....	44
	3.5.2 <i>Light Source and Camera</i> .....	46
	3.5.3 <i>Calibration Curve Capture and Generation</i> .....	47
	3.5.4 <i>Capturing Background and Experimental Images</i> .....	47
3.6	Experimental Procedure.....	48
	3.6.1 <i>Flow System</i> .....	48

4	RESULTS AND DISCUSSION .....	64
4.1	Overview .....	64
4.2	Visual Observations .....	65
4.3	Hue Statistics .....	68
4.4	FFT Analysis.....	71
5	CONCLUSION AND RECOMMENDATIONS .....	118
5.1	Conclusion .....	118
5.2	Recommendations.....	119
	REFERENCES .....	121
	APPENDIX A.....	124
	APPENDIX B.....	136

## LIST OF TABLES

3.1	Refractive index difference change due to sound pressure level .....	36
-----	--	----

## LIST OF FIGURES

1.1	Schematic diagram showing the large turbulence structures of a high-speed jet, the sound fields from the fine-scale turbulence and the Mach wave radiation from the large turbulence structures (Figure 4 of Tam et al, [ <sup>5</sup> ]).....	6
1.2	Schematic of the Optical Deflectometry Setup used by Veltin et al [ <sup>20</sup> ] .....	7
2.1	Schematic of the Optical Deflectometry Setup used by Veltin et al [ <sup>20</sup> ] .....	19
2.2	Schematic diagram representing an axisymmetric refractive index field by Kolhe and Agrawal [ <sup>27</sup> ].....	20
2.3	Experimental set up with Schlieren apparatus, supersonic jet, and rainbow filter .....	21
2.4	Schematic diagram illustrating the flow configuration and coordinate system.....	22
2.5	Filter calibration curves based on average image hue and hue at a pixel from Kolhe and Agrawal [ <sup>28</sup> ].....	23
2.6	Contours of angular deflection during the flicker cycle. The plots are 1/60th of a second apart. The contour levels are in 1/100th of a degree.....	24
2.7	Temperature profiles at $z/d = 15$ . Mean and RMS .....	25
2.8	Radial profiles of temperature at the axial plane $Z = 5$ mm. ....	26
2.9	Radial profiles of oxygen mole percent at the axial plane $Z = 5$ mm.....	27
2.10	Temporal evolution of the temperature field for 1000 fps, $Re = 300$ . (Contour levels are 1:400 K, 2: 800 K, 3: 1200 K, 4: 1600 K, 5: 2000 K and 6 :2300 K.) .....	28
2.11	Instantaneous schlieren images during an oscillation cycle ( $Re = 1550$ , $Ri = 3.76 \times 10^{-4}$ , $Gr = 93.6$ , $d = 4.2$ mm, $V = 37.5$ m/s).....	29
2.13	Details of lab burner (left). Crop of viewing area (right). ....	31

2.14	Calculated mean hue of combustion frame over entire duration of experiment.....	32
2.15	Calculated root mean square of hue in combustion frame over entire duration of experiment.....	33
3.1	Air system block diagram. ....	50
3.2	Schematic diagram of the stagnation chamber. ....	51
3.3	Photograph of stagnation chamber.....	52
3.4	Photograph of mounted stagnation chamber assembly.....	53
3.5	C-D nozzle schematic. ....	54
3.6	Experimental set up with schlieren apparatus, supersonic jet, and rainbow filter.....	55
3.7	Optical System Setup.....	56
3.8	Energetiq LDLS Light source controls (bottom left), Lazer and power supply (right), and light distribution box (left).....	57
3.9	Performance spectrum of the Energetiq LDLS system.....	58
3.10	Asymmetric 0.5 mm rainbow filter.....	59
3.11	Rainbow filter and camera setup.....	60
3.12	Alignment guide example .....	61
3.13	Example of background schlieren images at different traversing distances across the filter. ....	62
3.14	Filter calibration curves based on average image hue at a pixel.....	63
4.1	Actual image captures from the UHS-RSD technique. From left to right is single frame progression equal to 5 microseconds a) $Z/D$ between 19 and 27, more interference from small scale turbulent structures propagating upstream and downstream. b) $Z/D$ between 9 and 18, dominate wave in downstream direction from large scale turbulent structures.....	73
4.2	Actual schlieren image captures from the UHS-RSD technique. from left to right is single frame progression equal to 3.8 microseconds. $Z/D$ between 0 and 15, dominate wave in positive direction from large scale turbulent structures. ....	74

4.3	Actual image captures from the UHS-RSD technique. from left to right is single frame progression equal to 3.8 microseconds. $Z/D$ between 15 and 30, dominate wave in positive direction from large scale turbulent structures. ....	75
4.4	Schlieren images acquired at various random time steps used to illustrate intermittency. ....	76
4.5	Mean Hue of background images. Images captured with no flow to help determine uniformity of background image. ....	77
4.6	Standard deviation from the mean hue of background images. Images captured with no flow to help determine relative background noise. ....	78
4.7	Mean hue difference over the total field of view at $Z/D$ direction from 0 to 15. Course hue difference range spans 100 degrees hue ....	79
4.8	Mean hue difference over the total field of view at $Z/D$ direction from 15 to 30. Course hue difference range spans 100 degrees hue ....	80
4.9	Mean hue difference over the total field of view at $Z/D$ direction from 0 to 15. Fine hue difference range spans 20 degrees hue to see hue difference variation in acoustic regime ....	81
4.10	Mean hue difference over the total field of view at $Z/D$ direction from 15 to 30. Fine hue difference range spans 20 degrees hue to see hue difference variation in acoustic regime ....	82
4.11	Standard deviation from mean hue difference over the total field from $Z/D = 0$ to 15. Course degree deviation range spans 50 degrees. ....	83
4.12	Standard deviation from mean hue difference over the total field from $Z/D = 15$ to 30. Course degree deviation range spans 50 degrees. ....	84
4.13	Standard deviation from mean hue difference over the total field from $Z/D = 0$ to 15. Fine degree deviation range spans 15 degrees. ....	85
4.14	Standard deviation from mean hue difference over the total field from $Z/D = 15$ to 30. Fine degree deviation range spans 15 degrees. ....	86
4.15	RMS values of the OD signals along the axial direction in a fully expanded, $M_j = 1.75$ jet presented in Veltin (2011). ....	87
4.16	Hue difference RMS values of UHS-RSD along the lipline ( $R/D = 2$ ) for the axial locations of $Z/D = 0$ to 15. ....	88

4.17	Hue difference RMS values of UHS-RSD along the lipline ( $R/D = 2$ ) for the axial locations of $Z/D = 15$ to $30$ .....	89
4.18	$M = 1.75$ jet power spectral density measured at different radial location an at $x/D$ ( $Z/D$ ) = $5.5$ presented by Veltin (2011) .....	90
4.19	Frequency spectrum at $Z/D = 0$ .....	91
4.20	Frequency spectrum at $Z/D = 2.5$ .....	92
4.21	Frequency spectrum at $Z/D = 5$ .....	93
4.22	Frequency spectrum at $Z/D = 7.5$ .....	94
4.23	Frequency spectrum at $Z/D = 10$ .....	95
4.24	Frequency spectrum at $Z/D = 12.5$ .....	96
4.25	Frequency spectrum at $Z/D = 15$ .....	97
4.26	Frequency spectrum at $Z/D = 17.5$ .....	98
4.27	Frequency spectrum at $Z/D = 20$ .....	99
4.28	Frequency spectrum at $Z/D = 22.5$ .....	100
4.29	Frequency spectrum at $Z/D = 25$ .....	101
4.30	Frequency spectrum at $Z/D = 27.5$ .....	102
4.31	Frequency spectrum at $R/D = 1.5$ for $Z/D = 2.5$ to $15$ .....	103
4.32	Frequency spectrum at $R/D = 2$ for $Z/D = 2.5$ to $15$ .....	104
4.33	Frequency spectrum at $R/D = 2.5$ for $Z/D = 2.5$ to $15$ .....	105
4.34	Frequency spectrum at $R/D = 3$ for $Z/D = 2.5$ to $15$ .....	106
4.35	Frequency spectrum at $R/D = 4$ for $Z/D = 2.5$ to $15$ .....	107
4.36	Frequency spectrum at $R/D = 5$ for $Z/D = 2.5$ to $15$ .....	108
4.37	Frequency spectrum at $R/D = 5.5$ for $Z/D = 2.5$ to $15$ .....	109
4.38	Frequency spectrum at $R/D = 6$ for $Z/D = 2.5$ to $15$ .....	110

4.39	Frequency spectrum at $R/D = 3$ for $Z/D = 15$ to $27.5$ .....	111
4.40	Frequency spectrum at $R/D = 3.5$ for $Z/D = 15$ to $27.5$ .....	112
4.41	Frequency spectrum at $R/D = 4$ for $Z/D = 15$ to $27.5$ .....	113
4.42	Frequency spectrum at $R/D = 4.5$ for $Z/D = 15$ to $27.5$ .....	114
4.43	Frequency spectrum at $R/D = 5$ for $Z/D = 15$ to $27.5$ .....	115
4.44	Frequency spectrum at $R/D = 5.5$ for $Z/D = 15$ to $27.5$ .....	116
4.45	Frequency spectrum at $R/D = 6$ for $Z/D = 15$ to $27.5$ .....	117

# CHAPTER 1

## JET NOISE RESEARCH

### Introduction

Noise generated by exhaust gas expelling from aviation gas turbines can create various health and hearing related problems for individuals in near proximity to the engine, and nearby communities that experience the high power sound shock waves while aircraft is in transit. Several passive techniques based on mechanical chevrons and fluidics have been developed to reduce the noise generation, but at the cost of lower engine performance. Active techniques can be utilized to control the noise generation, however they require the ability to determine the origin of noise sources and real-time control systems. Previous research has tracked the occurrence of jet noise to be a direct relation of turbulent structure interactions in the near-field (less than 20 nozzle diameters of the jet exit) and their propagating effect in the far-field. Velocity, pressure, and density fluctuations in the jet flow have been measured in numerous past experiments to gain understanding of the jet noise generation process. Conventional sound measuring techniques involve inserting a sound probe to obtain local sound measurements. Over the past few decades several techniques have been developed to provide direct means of measuring flow characteristics within, and in the near- and far-field of the jet to develop fundamental aero-acoustic models. Recent research has shown that non-intrusive acoustic

measurements can be made locally by correlating the time response data of two spatially separated optical sensors.

As early as in the 1950s investigations of near-field pressure fluctuations of unbound supersonic jets by Lighthill [1] led to attempts to understand the relationship between flow field dynamics, sound production mechanisms, and the process for acoustic wave propagations from the jet flow field to the far-field. This study identified small scale turbulent eddies in the shear layer of jet flows as the source of the sound generation. Early experimental work was carried out exclusively with hot-wire anemometry in subsonic jets by Davies et al.[2], Bradshaw et al.[3], and Crow and Champagne[4], and others. These studies led to the understanding that additional large scale turbulent structures also develop in the flow field and are a source of highly directional noise generation. (Tam et al.) [5] These large scale structures become more intense at high jet speeds and the combination effect of both large and small scale turbulence eddies makes it difficult to measure and quantify noise generation in supersonic jets.

Figure 1.1 taken from Tam et al [5] attempts to represent the two noise sources and their effective acoustic fields. Both acoustic fields originate from the shear layer of the jet flow where turbulent eddies form due to the jet / ambient environment interactions. The small scale eddies form at all locations along the jet shear layer and they result in non-uniform acoustic wave signatures to propagate away from the jet in all directions. The large eddies are formed in the jet shear layer within a narrow band downstream of the nozzle exit. Acoustic waves from these large scale eddies have a very directional path.

Many jet noise studies employ microphone arrays positioned outside the jet flow field to measure the acoustic field. (Panda et al) [6,7] Thus, the acoustic field is measured by sound probes separated by a set increment along the jet flow field path. This technique can determine

the net result of complex turbulent jet flow or noise locally by means of direct measurements, but the underlying turbulent interactions in the jet flow and acoustic field cannot be resolved, because the turbulence produced in the jet flow cannot be detected by sound probes. In order to develop accurate aero-acoustic models of supersonic and subsonic jets direct measurements of the jet flow must be related to the near- and far-field sound measurements.

McLaughlin et al [8] and Troutt and McLaughlin [9] used hot-wire anemometry to measure turbulence in supersonic jets by conducting experiments in a reduced density anechoic chamber. The hot-wire technique introduces a wire directly in the flow field for each measurement location. This intrusive nature not only affects measurement accuracy but prevents simultaneous data collection at multiple locations. Lau [10] and Kerherve et al [11] used laser Doppler velocimetry (LDV), but uncertainties related to non-uniform seeding of particles failing to track the high speed jet flow cause difficulties in accurately identifying noise generation sources. Recently, Bridges [12] and Kastner et al [13] used Particle Image Velocimetry (PIV) to characterize turbulence in high-speed jet flows. High spatial resolution is attainable in these experiments, but there are still issues with seeding, and the temporal resolution to accurately measure turbulence is poor because of the limited pulse rate of high-power lasers needed for the setup.

Seasholtz et al [14, 15] was able to develop a fully non-intrusive molecular Rayleigh scattering apparatus with the capabilities of obtaining density and velocity fluctuation measurements simultaneously in high speed flows. Subsequently, Panda and Seasholtz [16] and Panda et al [17] applied this technique and discovered correlation between jet flow density measurements and acoustic pressure measurements. This was the first time that direct evidence of the two distinct noise sources illustrated in figure 1.1 was obtained.

Recently, Doty and McLaughlin [18] used Optical Deflectometry (OD) to conduct measurements on supersonic jets to correlate turbulent flow properties with the acoustic field. This work was continued by Papamoschou et al [19] and Veltin et al [20] to show that the flow field data measured by the OD technique can be correlated with direct acoustic measurements in the near- and far- fields. The OD technique is based on the schlieren principle which utilizes the fact that light rays deflect as they pass through a test media of varying density gradients as illustrated in Figure 1.2. (Veltin et al) [20] The technique uses a parabolic mirror to collimate light rays through the test media. Deflected light rays are decollimated by a second parabolic mirror to form the source image at the focal point, where a knife-edge is placed. The knife edge converts light ray deflection into light intensity gradations, which are detected by a photodiode positioned to map a specific point location in the flow field. Only a few photodiode arrays can be used, and thus, the OD technique is limited to simultaneous local measurement at only a few discrete locations of the jet flow.

### Overview and Objectives

The previous section outlined the advances in the aero acoustics field involving the study of supersonic and subsonic gas jets. Significant insights have led to a better understanding of the fundamental guiding principles of jet noise generation. However, detailed understanding of the correlation between turbulence developed within the jet flow field and the propagating pressure field that produce an acoustic signature in the far field is still lacking. The reason for this gap in the understanding results from the fact that the near field jet flow and the far field acoustic signature are measured separately from one another. Current efforts only allow for the correlation of measurements attained by sound probe arrays in the acoustic field and specialized

flow measurements techniques discussed in the previous section in the flow field. These two techniques must be separated spatially and any conclusions are drawn only from the correlation between the two data sets obtained.

Recent advances involving technology utilized in the rainbow schlieren deflectometry (RSD) technique offer a solution to the limitations experienced in previous aero acoustic research. Advances in ultra-high speed (UHS) digital photography allow excellent temporal resolution while still allowing large field of views to simultaneously capture near and far field data in high speed jets. Also, advances in precision optics have provided a means for the RSD technique to measure very small pressure fluctuations in acoustic waves. The objective of this research is to combine the previously mentioned technologies to develop an Ultra High Speed RSD (UHS-RSD) system. This system will be used to demonstrate the capabilities of the UHS-RSD technique to capture sound wave propagations from supersonic air jets. The next objective of this research is to optimize the UHS-RSD system design to acquire quantitative data to bridge the understanding of noise generation in turbulent jet flows with the acoustic signatures detected away from the flow field.

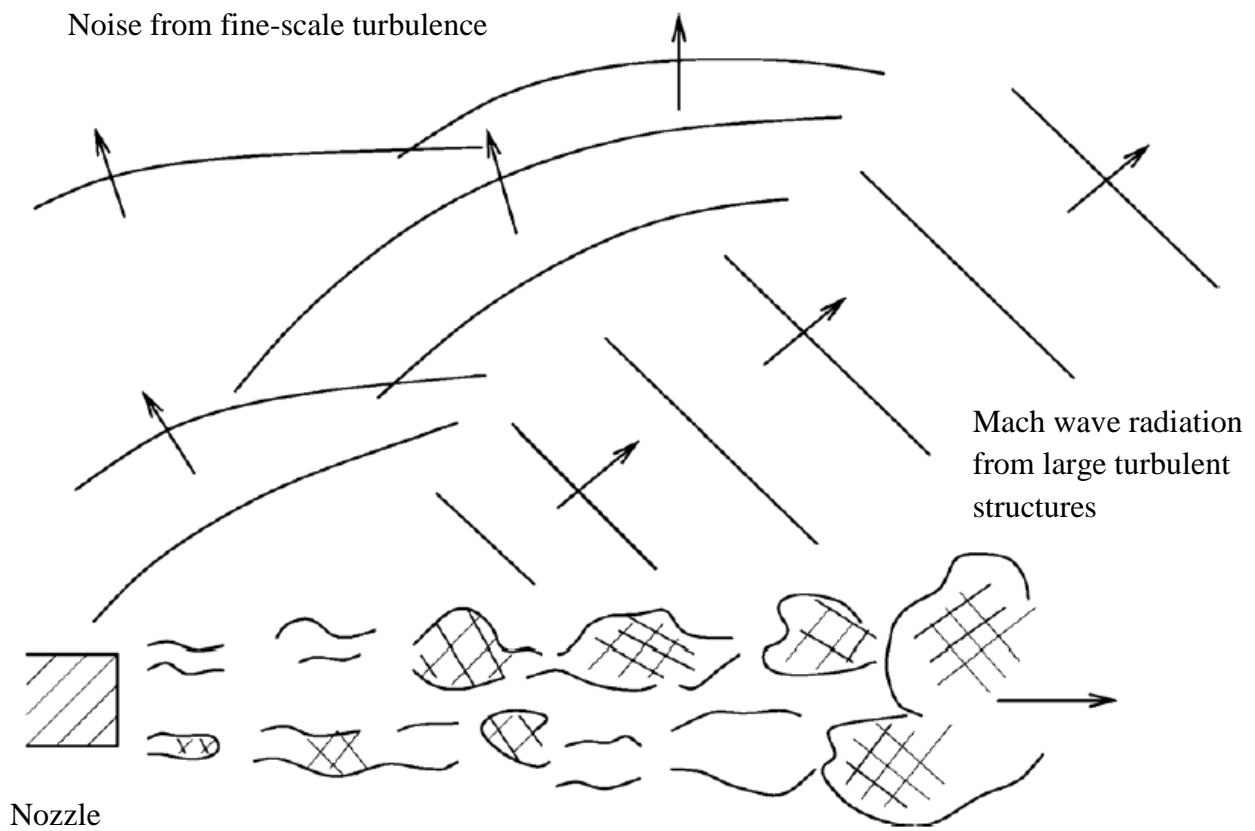


Figure 1.1 Schematic diagram showing the large turbulence structures of a high-speed jet, the sound fields from the fine-scale turbulence and the Mach wave radiation from the large turbulence structures (Figure 4 of Tam et al, [5])

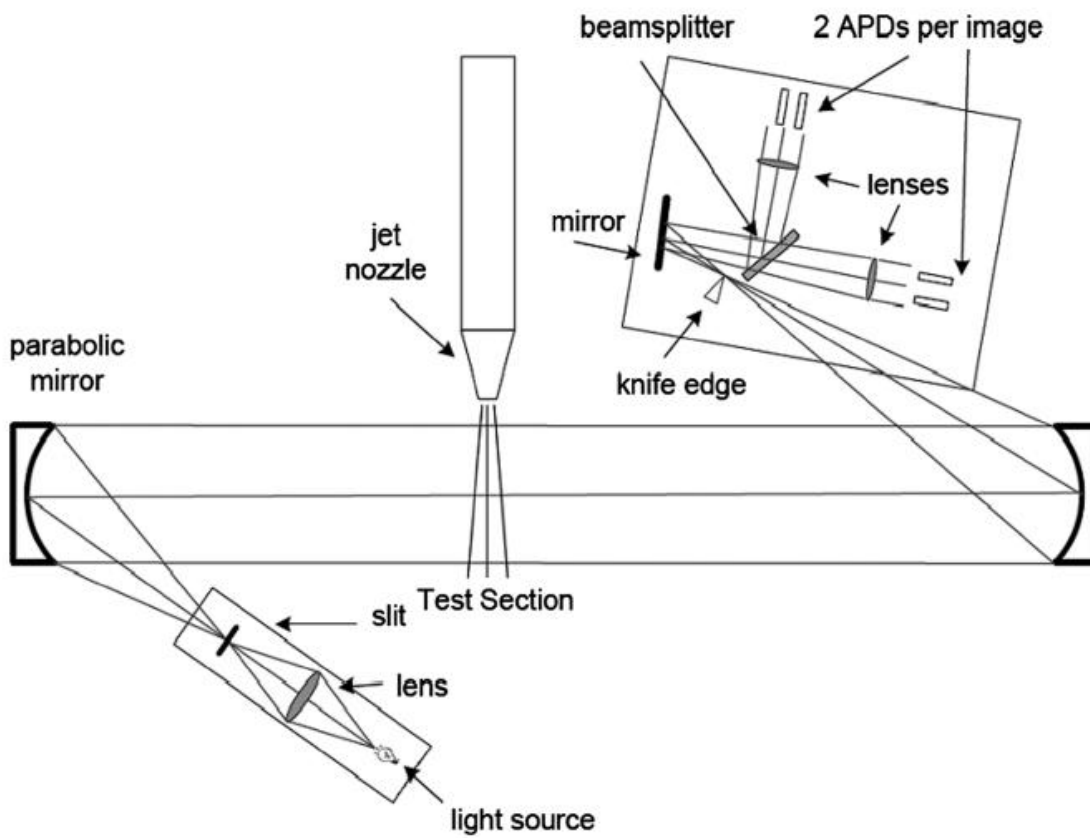


Figure 1.2 Schematic of the Optical Deflectometry Setup used by Veltin et al [20]

## CHAPTER 2

### RAINBOW SCHLIEREN DEFLECTOMETRY

#### Rainbow Schlieren Theory and Methodology

Optical techniques used in flow field diagnostics have significant advantages over other competing methods. First, they are a non-intrusive technique because probes do not have to be inserted into the flow field to make measurements. Second, due to recent innovations in UHS photography and precision optics high spatial and temporal resolutions can be obtained with these setups. Two types of techniques are used for transforming the image data received by the camera depending on the methods used to acquire the data. Methods that acquire measurements locally can calculate local field variables. However, line of sight methods produce path integrated measurements. The path integrated measurements must be deciphered using inversion and de-convolution algorithms to obtain local field information. The schlieren technique is a line of sight technique i.e. it acquires path integrated measurements.

The Rainbow Schlieren Deflectometry (RSD) technique is the primary flow visualization and diagnostic technique utilized for this study of supersonic cold air jets and is the focus of this research. The RSD technique is based on the schlieren principle which utilizes the fact that light rays will deflect as they pass through a test media of varying density gradients. Historically a Z type configuration like the one presented in Figure 2.1 is used to acquire black and white schlieren images of the flow field. The setup utilizes a parabolic mirror to collimate light rays

passing through the test media. Deflected light rays are decollimated by a second parabolic mirror to form the source image at the focal point, where a knife-edge is placed. The knife edge converts light ray deflection into light intensity gradations, which are detected by a camera or photodiode sensor positioned to map a specific point in the flow field. To translate the deflection angle to quantifiable local data, a coordinate system must be set up to take in account that this technique is a line of sight technique. Figure 2.2 shows how the coordinate system for this technique is set up. Here  $\varepsilon$  is considered the transverse deflection angle of the light ray. It is related to the local field i.e.  $\delta$  or the normalized refractive index difference.

Similar to the schlieren technique described previously, Greenberg [21] developed the RSD technique which relies on light ray deflection. This technique uses an intense white light source at the source aperture, collimation and de-collimation optics utilize achromatic lenses to minimize chromatic aberration, the knife-edge is replaced by a continuously graded color filter, and the filtered image of the test media is acquired by a digital camera. An experimental setup of the thus described approach is presented in Figure 2.3. Greenberg's approach was significant in determining a way to quantifiably measure deflection angle and its statistics from color schlieren images. The use of a color filter allowed an accurate measuring device to quantify deflection angle of the light rays by comparing the background image color detected by the filter with no flow compared with the color detected when flow is present. Traditional methods utilizing a knife edge relied on light intensity data and were therefore arbitrary and no accurate calibration method could be developed to compare flow and no flow conditions. Greenberg showed that by representing color in terms of hue value, a calibration method could be employed to quantifiably determine the deflection angle and hence scalar field properties related to it.

In a typical RSD system a broadband white light source is contained within a mounting box that is centered down the path of the system setup. At the exit of this mounting box is a rectangular source aperture. The aperture is positioned at the focal point of an achromatic collimating lens. Light projected on the lens is redirected into parallel light rays passing through the test media. The test media causes a slight deflection in the light rays because of the variations in refractive index of the flow field. The refractive index difference is the result of the density gradients experienced by the flow field. The deflected light rays pass through the test media, and then through the de-collimating lens aligned parallel to the collimating lens. The light rays are de-collimated causing convergence onto a rainbow filter placed at the focal point of the de-collimating lens. The image size of the source aperture on the filter is directly related to the source aperture size and the focal points of the achromatic lenses used. Equation 2.1 shows how the focal lengths of achromatic lenses affect the magnification of the source aperture image created on the filter plane.

$$\text{Filter Image Dimensions} = \frac{f_2}{f_1} \cdot \text{Source Aperture Dimensions} \quad (2.1)$$

The rainbow filter is continuously graded color filter printed on a 35 mm slide film. The filter can be designed with a symmetric or asymmetric color gradation. An example of an asymmetric color range filter is shown in the bottom right of Figure 2.3. In this filter the colors vary linearly along the transverse direction, and the source image is centered within this hue range to achieve the best sensitivity of the resulting image on the digital camera. The image passing through this filter is detected by a camera sensor with camera lens positioned as close to the filter as physically possible. The camera lens focuses the test media onto the camera sensor. Schlieren images are captured by a digital camera and the images are downloaded in the RGB (red green blue) format as TIFF files onto a computer. The images can then be processed with

several different analytical approaches. The main advantage here as compared to the traditional schlieren technique is that the color filter allows for quantitative measurements of transverse deflection angle, which can be related to density, pressure, or temperature in the local flow field.

### Key Mathematical Equations

The rainbow schlieren technique requires the deconvolution of path integrated data to obtain local scalar fields in a coordinate system set up to relate the two data sets. Figure 2.4 shows the flow configuration and coordinate system utilized for the RSD technique. Here the line of sight measurements are integrated along the path of the refractive index difference gradient normal to the line of sight. The gradient direction can either be in the axial or transverse directions. Therefore, two equations can be set up to obtain either transverse deflection angle or axial deflection angle. Equation 2.2 gives transverse deflection angle and Equation 2.3 gives axial deflection angle.

$$\varepsilon_{xy}(x, t) = \frac{1}{\eta_o} \int_{-\infty}^{\infty} \left\{ \frac{\partial \eta}{\partial x}(x, y, z, t) \right\} \cdot dy \quad (2.2)$$

$$\varepsilon_{zy}(x, t) = \frac{1}{\eta_o} \int_{-\infty}^{\infty} \left\{ \frac{\partial \eta}{\partial z}(x, y, z, t) \right\} \cdot dy \quad (2.3)$$

where  $\eta$  is the local refractive index and  $\eta_o$  is the refractive index of the surroundings.

The RSD technique measures the small angle resulting from light rays deflection through a medium with varying refractive indexes caused by density gradients. When the light rays are de-collimated and focused on the filter plane, the rays produce transverse and axial displacements that show up as a color shift from the original color when no flow is passing through the viewing area. The transmitted color is detected by a camera downstream of the filter. The rainbow schlieren image depends on the location that a light ray focuses on the filter plane.

Thus the rainbow filter serves as a fine ruler to accurately measure the ray displacement at the filter plane. The density varies in both the transverse and axial directions. However, the rainbow filter is sensitive only to the transverse displacements if color strips and source aperture are both aligned and parallel to the axial direction. In the following experiments the rainbow filter is positioned to detect deflection angles in the transverse direction only.

For steady laminar flows the test media can be considered as axisymmetric. Therefore, a simplification can be made to the equation of the instantaneous transverse ray deflection angle. In the case for axisymmetric steady laminar flow, the transverse ray deflection angle is

$$\varepsilon(y) = 2y \cdot \int_y^\infty \frac{\partial \delta}{\partial r} \frac{dr}{\sqrt{r^2 - y^2}} \quad (2.4)$$

where  $r$  is the radial coordinate,  $y$  is the offset distance from the jet axis and the local field variable is the normalized refractive index difference represented in equation 2.5

$$\delta = \left( \frac{\eta}{\eta_o} - 1 \right) \quad (2.5)$$

The transverse deflection angle is related to transverse displacement measured by the RSD apparatus. These two quantities are related by equation 2.6.

$$d(y) = \varepsilon(y) \cdot f \quad (2.6)$$

where  $f$  is the focal length of the de-collimating lens, and  $d(y)$  is the transverse ray displacement on the filter plane. A filter calibration process is necessary to obtain the transverse ray displacement on the filter plane from hue measured in the color schlieren image and will be discussed in more detail in the next section.

Utilizing the transverse deflection angle on the filter plane, the normalized refractive index difference for axisymmetric flow can be determined by the Abel inversion given by equation 2.7.

$$\delta(r) = \frac{-1}{\pi} \int_r^\infty \varepsilon(y) \cdot \frac{dy}{\sqrt{y^2 - r^2}} \quad (2.7)$$

Equation 2.7 can be discretized and solved numerically as

$$\delta(r_i) = \sum_{j=1}^{n+1} D_{ij} \epsilon_j \quad (2.8)$$

where  $D_{ij}$  are geometric coefficients and are discussed in great detail by Agrawal et al. [22]

The scalar thermodynamic properties can then be determined by first relating the normalized refractive index difference to density by the Gladstone-Dale relationship given as

$$\rho = \frac{\delta}{K} \quad (2.9)$$

where  $K$  is the Gladstone-Dale constant.

For an isentropic flow the density can be related to pressure and temperature by thermodynamic relations shown in equations 2.10 and 2.11.

$$\frac{T}{T_e} = \left( \frac{\rho}{\rho_e} \right)^{(\gamma-1)} \quad (2.10)$$

$$\frac{P}{P_e} = \left( \frac{\rho}{\rho_e} \right)^\gamma \quad (2.11)$$

### Rainbow Filter and Filter Calibration

Since the method to obtain refractive index difference is based on the color difference experienced by deflected light, a means to acquire meaningful parameters has previously been developed to quantify the color in the schlieren images. The color images are stored in the RGB format. In this format the levels of red, green, and blue at a particular pixel location are used to represent the color. A single color parameter is more desirable for quantification and therefore the RGB formatted image is converted to HSI format image. The HSI or Hue Saturation Intensity model has the advantage of specifying color by a single parameter, hue, unlike the three attributes required in the RGB color model [for additional details refer Greenberg et al. [23]].

Once hue information is extracted from the color schlieren image, it is related to the displacement of the light ray on the filter plane. Therefore a rainbow filter calibration curve must be developed. The filter calibration curve is generated by acquiring the background schlieren images obtained without the test medium. The filter is traversed by equally spaced intervals in the transverse direction to acquire images at different transverse filter positions. Figure 2.5 shows a typical filter calibration curve. Once the calibration images are captured, schlieren images with the test media can be acquired. Care must be taken during the calibration step to prevent disturbances to the optical setup or any other part of the experimental setup and surrounding environment. This practice ensures that a given pixel in the schlieren image maps the same physical location with or without the test medium.

The transverse position on the filter calibration curve for an image pixel with hue  $H$  can be calculated by using interpolation between the background and experimental images and the calibration curve. Equation 2.12 is used to perform this interpolation to obtain the transverse position on the filter plane.

$$X(H) = X_i + \frac{X_{i+1} - X_i}{H_{i+1} - H_i} \cdot (H_{i+1} - H) \quad (2.12)$$

where  $(X_i, H_i)$  and  $(X_{i+1}, H_{i+1})$  are the filter calibration coordinates closest to the measured hue  $H$ .

Referring back to Equation 2.6 the transverse deflection angle can be found by

$$\varepsilon(y) = \frac{d(y)}{f} = \frac{X(H) - X(H_b)}{f} \quad (2.13)$$

where  $X(H_b)$  is the transverse position on the filter calibration curve pertaining to the background hue  $H_b$  or the hue value at the pixel location in the schlieren image without the test

medium. A filter calibration curve is generated at each pixel location in the field of view to ensure that hue measurement errors at a pixel location are not introduced into the transverse deflection angle calculations.

### Basic Analysis of Experimental Images

Once the hue and hue difference at each pixel location over the field of view is obtained, an in-depth analysis can be performed. However, basic statistical data can be calculated to provide insight into the flow characteristics. For example the mean hue at each pixel location in the background images indicates alignment accuracy and background uniformity. The standard deviation (STD) of hue at each pixel location in the background image helps with determination of measurement noise. STD of hue difference of the experimental images offers insight into the relative turbulence in different regions of the flow field. For example, the shear layer region of the flow field is expected to generate large turbulent fluctuations. Therefore, STD of hue would be larger in these regions. Spectral analysis of hue and/or deflection angle data provides even greater insight into the flow field. In particular, fast Fourier transform (FFT) can offer insight into the frequency content of the turbulent flow and acoustic fields.

### Past Applications of RSD

Research utilizing the RSD technique for quantitative measurements of fluid flow fields has been extensively studied. Early work focused on laminar hydrogen jets and flames. The RSD technique has proven to give the capabilities of measuring temperature, density, and concentration fields in these flows. Further research has attempted to calculate turbulence in

unsteady reacting and non-reacting flows. A cross beam correlation algorithm has been developed utilizing the RSD technique.

Albers and Agrawal [<sup>24</sup>] used the RSD technique to study a flickering hydrogen gas-jet diffusion flame. This research showed that global oscillation frequency in the flow field of the flame varies linearly with operating pressure. Contours of the angular deflection were plotted and are reproduced in figure 2.6. Deflection angle information was used to obtain statistical information on the temperature profiles of the diffusion flame. Figure 2.7 represents the mean and RMS temperature profile at an axial location of  $z/d = 15$ . They showed that the mean temperature profiles had a shape characteristic of a typical steady diffusion flame. The RMS temperature profiles show peaks in the inner shear layer and in the oxidizer-side of the flame surface.

Alammar and Agrawal [<sup>25</sup>] demonstrated that quantitative measurements of scalar profiles in reacting flows can be obtained by the RSD technique. In this study, the state relationship based on chemical equilibrium was used to relate the refractive index difference to temperature and oxygen concentration in a hydrogen gas-jet diffusion flame. Figure 2.8 shows the temperature profile obtained by the RSD technique compared to thermocouple measurements. Figure 2.9 shows comparison of oxygen concentration obtained by the RSD technique and a calibrated oxygen gas analyzer. Results show that the RSD technique provides accurate results when compared to measurements obtained via intrusive probes.

Agrawal and Wong [<sup>26</sup>] applied high-speed RSD for quantitative measurements in unsteady flames. The flame shapes were compared to the visual flame boundaries of the steady flame. The scalar properties of the hydrogen jet diffusion flame were quantified. In this study the flames were assumed to be axisymmetric, therefore tomographic inversion based on a single

field of view was sufficient to obtain the local distributions of the scalar flow properties. As presented in figure 2.10 the temporal evolution of the temperature field for the flame could be determined at high framing rates.

The RSD technique has been utilized to investigate transitional jet diffusion flames to identify interactions of shear layer instabilities and how they affect the flame structure, Agrawal and Kolhe [27]. Focus was placed on buoyancy effects in hydrogen jet flames with momentum-dominated fuel jet at the injector exit. Figure 2.11 shows contours of the instabilities developed within the flame during an oscillation cycle.

Complex interactions among shock waves were studied utilizing miniature-RSD in supersonic micro jets, Agrawal and Kolhe [28]. These experiments provided high-resolution measurements to help explain the flow field of an under-expanded micro jet from an orifice, relevant to leakage from a compressed gas storage facility. Figure 2.12 shows the schlieren image and the reconstructed density and deflection angle fields in the jet flow.

A cross beam correlation algorithm was developed to reconstruct turbulent flow fields utilizing the RSD technique, Agrawal and Kolhe [29]. Scalar turbulence measurements in momentum dominated turbulent helium jets have been obtained using RSD and spectral analysis algorithms, Kohle and Agrawal [7]. Here the mean, variance, integral length scale, autocorrelation function, power spectral density, and dissipation power density of local scalar field are obtained to characterize the turbulent flows. This study shows a decrease in variance of deflection angle as the jet spreads radially in the flow direction.

So far qualitative measurements of turbulent reacting flows are beyond the scope of the current RSD capabilities; however several insights could be gained from experimental observations. Figure 2.13 shows a basic experimental setup for such a reacting flow in a swirl

stabilized combustor initially utilized by the author. The image on the right side of figure 2.13 is an instantaneous image of the premixed reacting flow field. Mean and RMS hue data were acquired with this setup and a basic analysis was performed based on these results.

Figure 2.14 represents the mean hue and it can be shown that there is a slight skew in the hue value from left to right, because of the asymmetry of the rainbow filter. The image represented in figure 2.15 illustrates regions of high and low turbulence. Toward the bottom center of the test area it is observed that the turbulence is very high. Further upstream it is observed that the flame is less turbulent.

The RSD technique has been utilized in a variety of applications to perform quantitative measurements of non-reacting and reacting fluid flow field. This technique has proven very accurate at acquiring local field parameters over a wide range of operating conditions and turbulence levels.

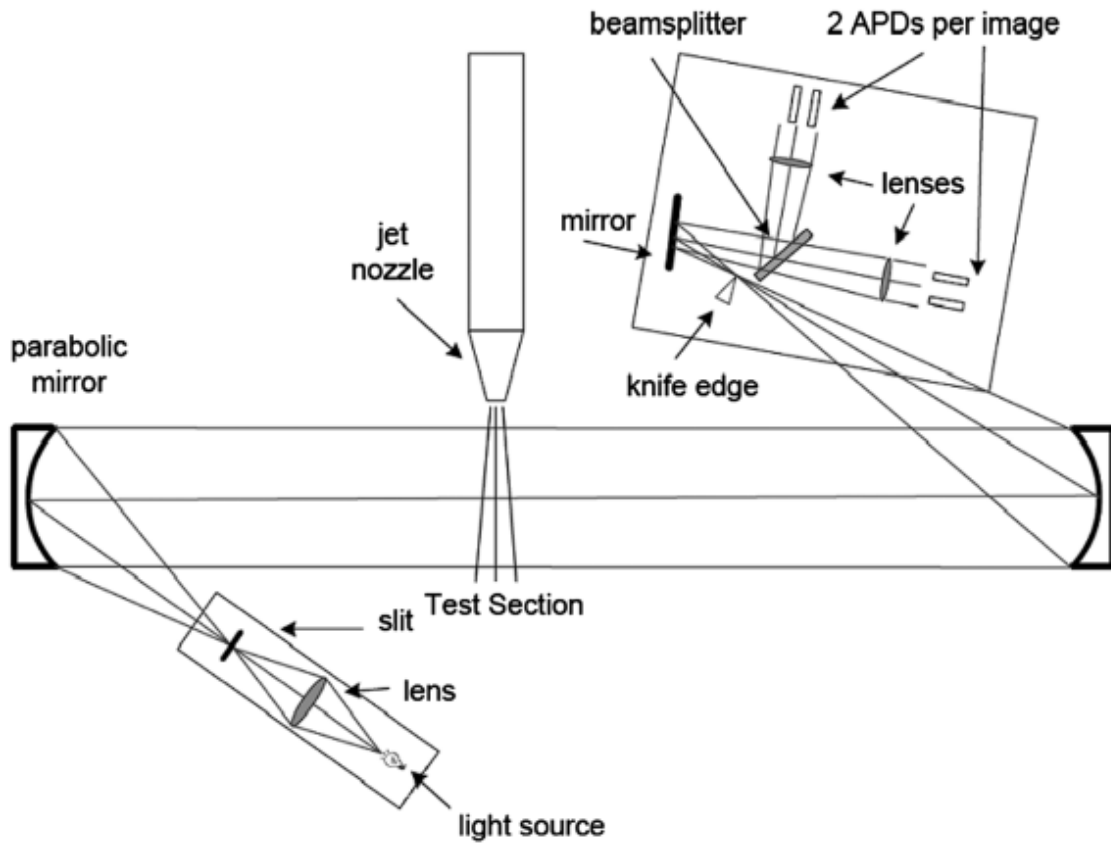


Figure 2.1 Schematic of the Optical Deflectometry Setup used by Veltin et al [20]

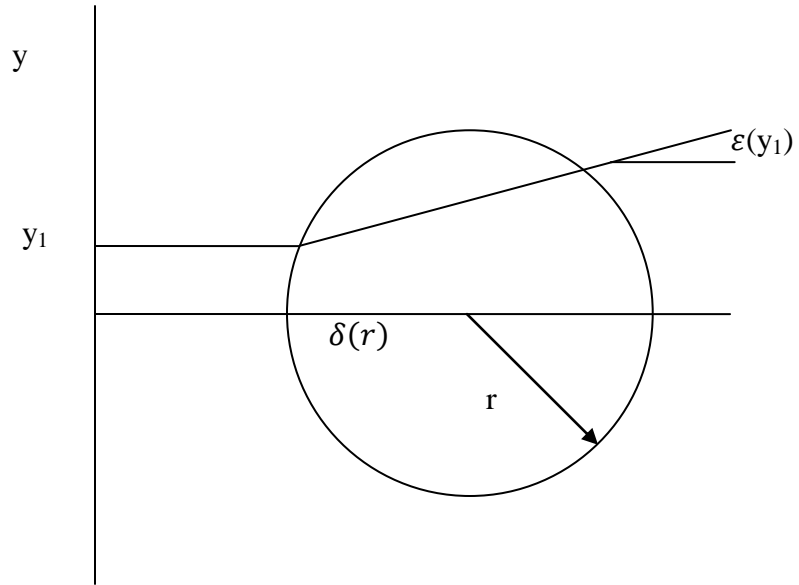


Figure 2.2 Schematic diagram representing an axisymmetric refractive index field by Kolhe and Agrawal [<sup>27</sup>]

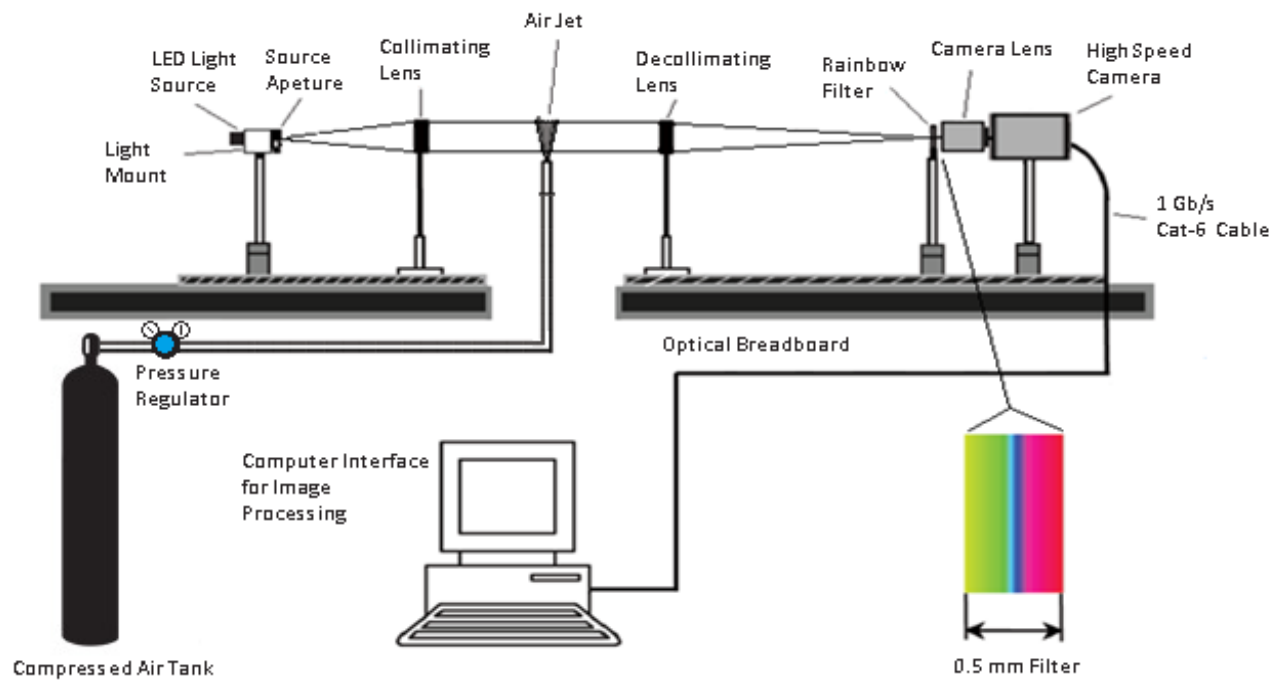


Figure 2.3 Experimental set up with Schlieren apparatus, supersonic jet, and rainbow filter

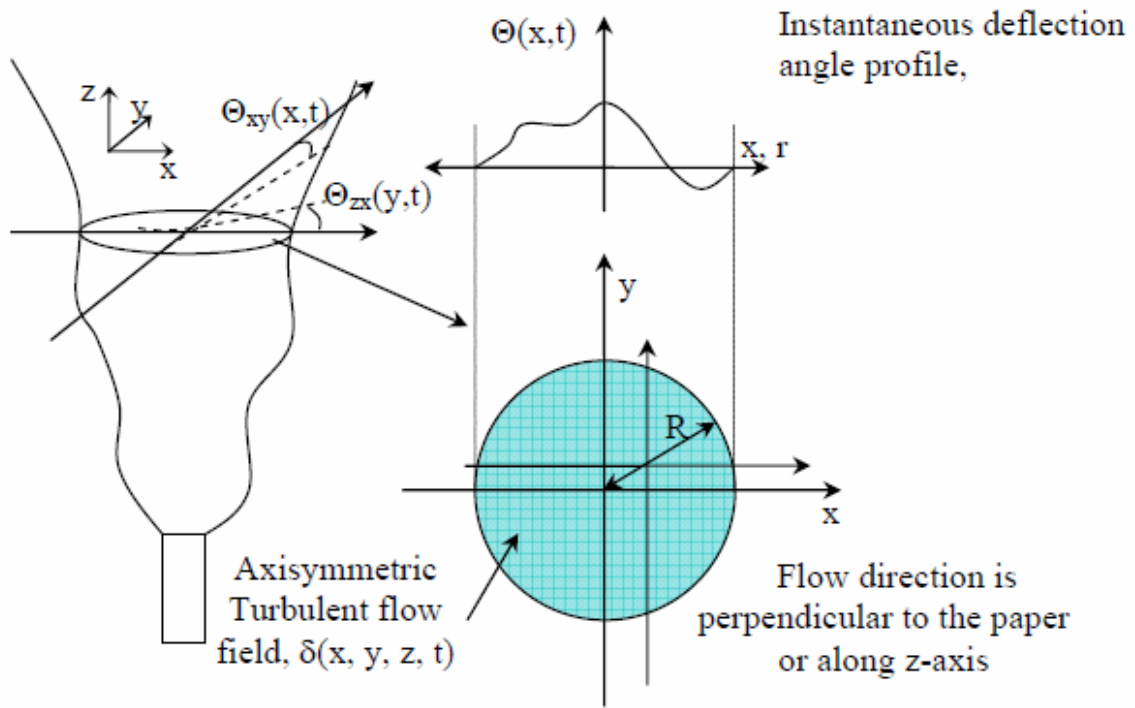


Figure 2.4 Schematic diagram illustrating the flow configuration and coordinate system.

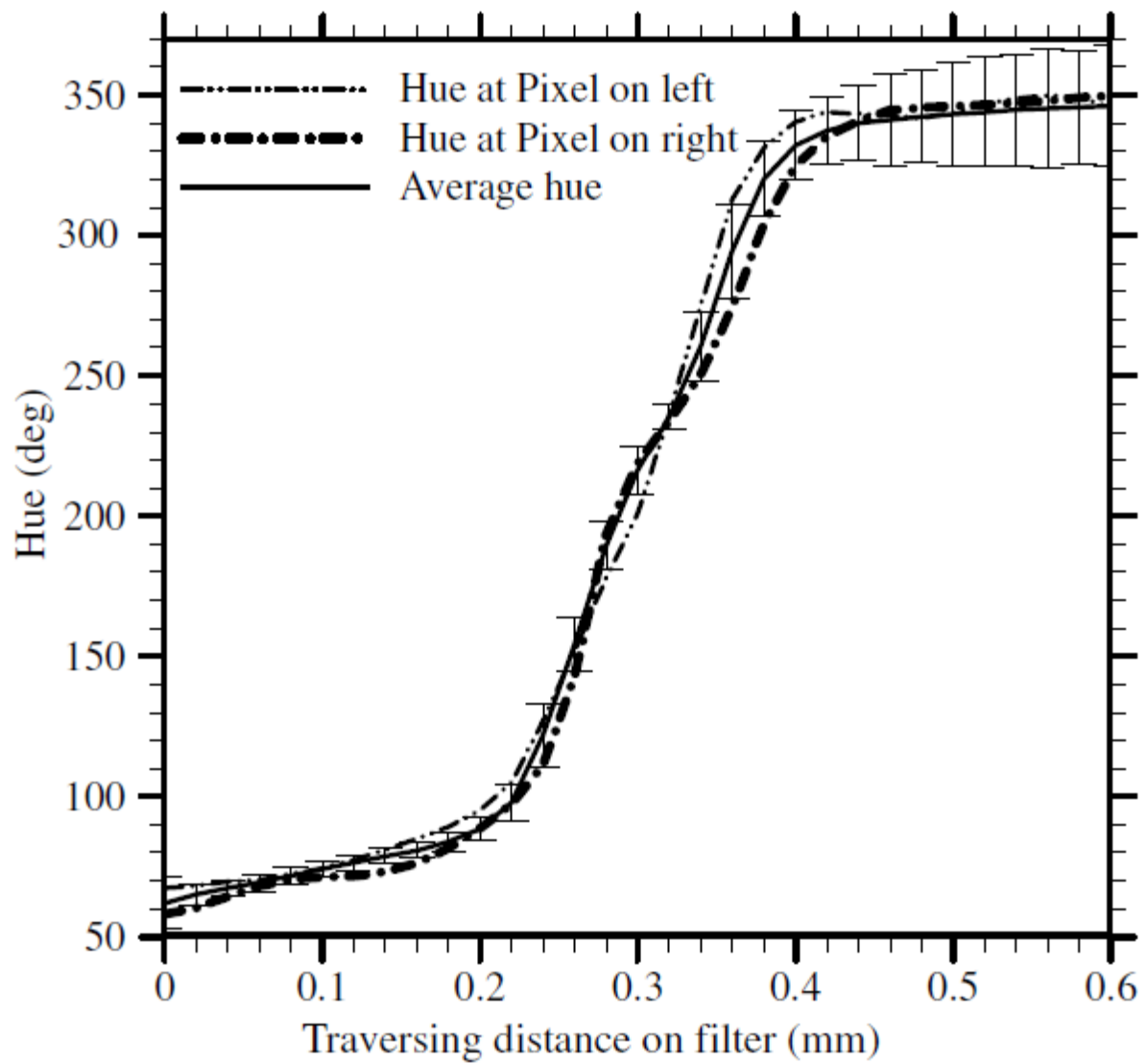


Figure 2.5 Filter calibration curves based on average image hue and hue at a pixel from Kolhe and Agrawal [28].

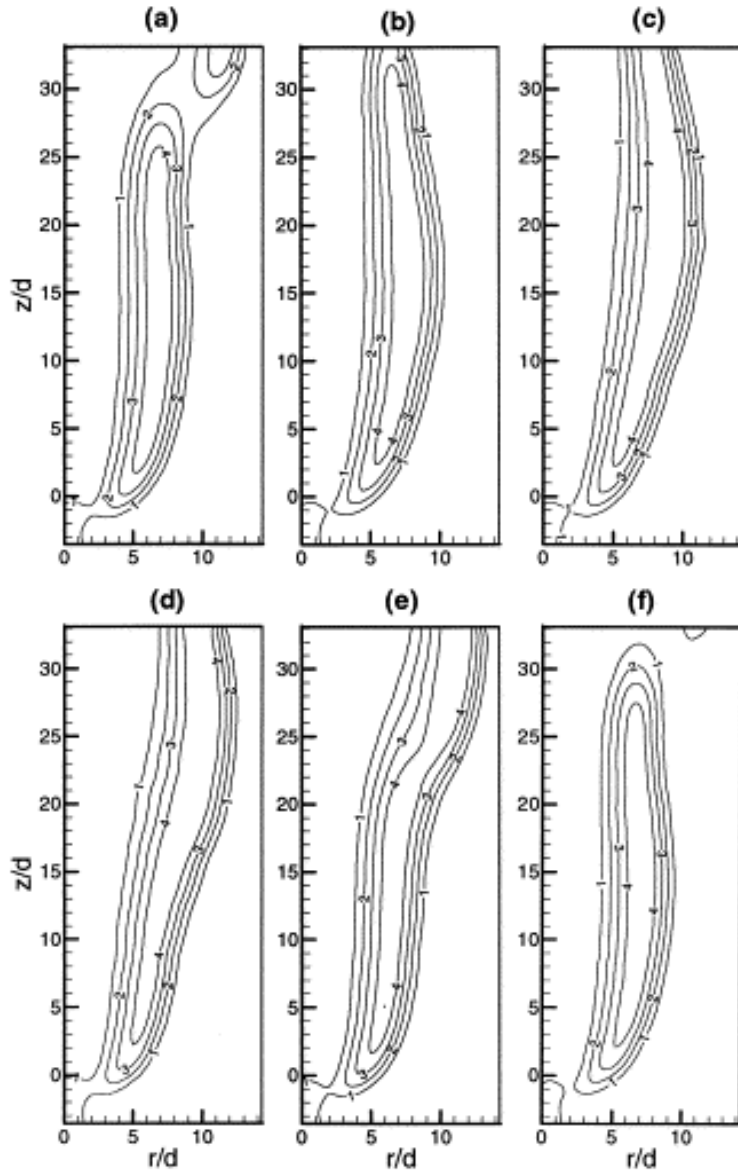


Figure 2.6 Contours of angular deflection during the flicker cycle. The plots are  $1/60$ th of a second apart. The contour levels are in  $1/100$ th of a degree.

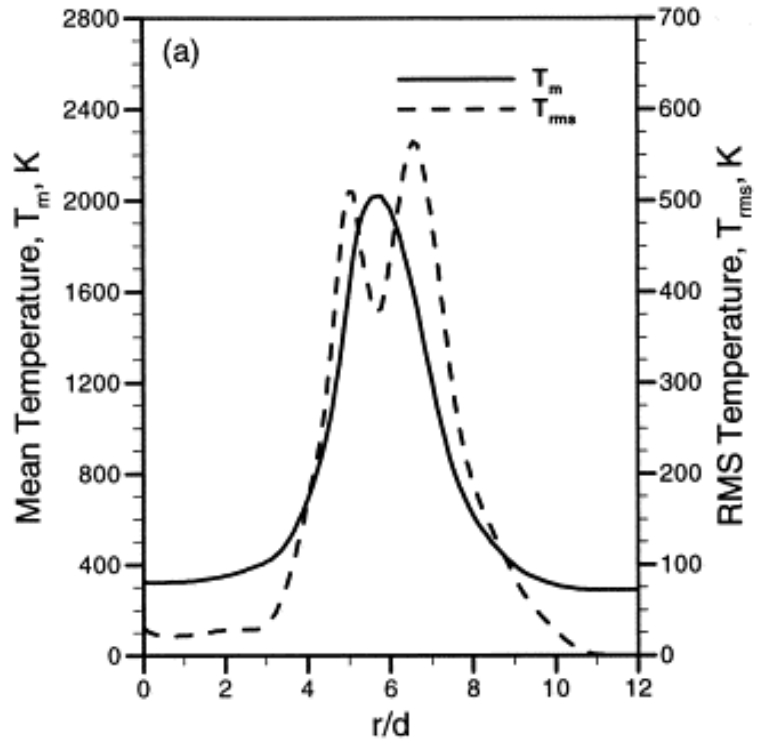


Figure 2.7 Temperature profiles at  $z/d = 15$ . Mean and RMS

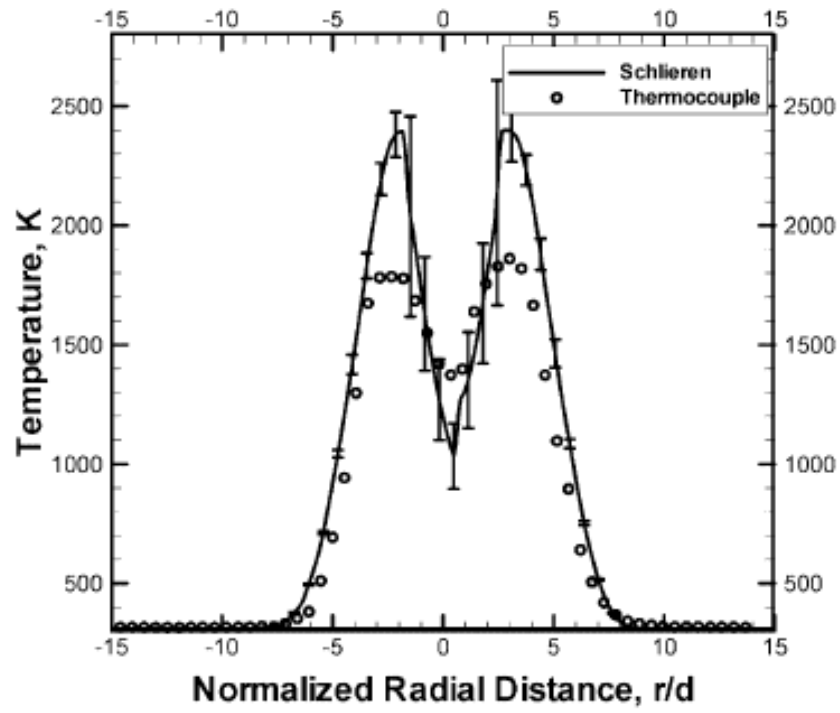


Figure 2.8 Radial profiles of temperature at the axial plane  $Z = 5$  mm.

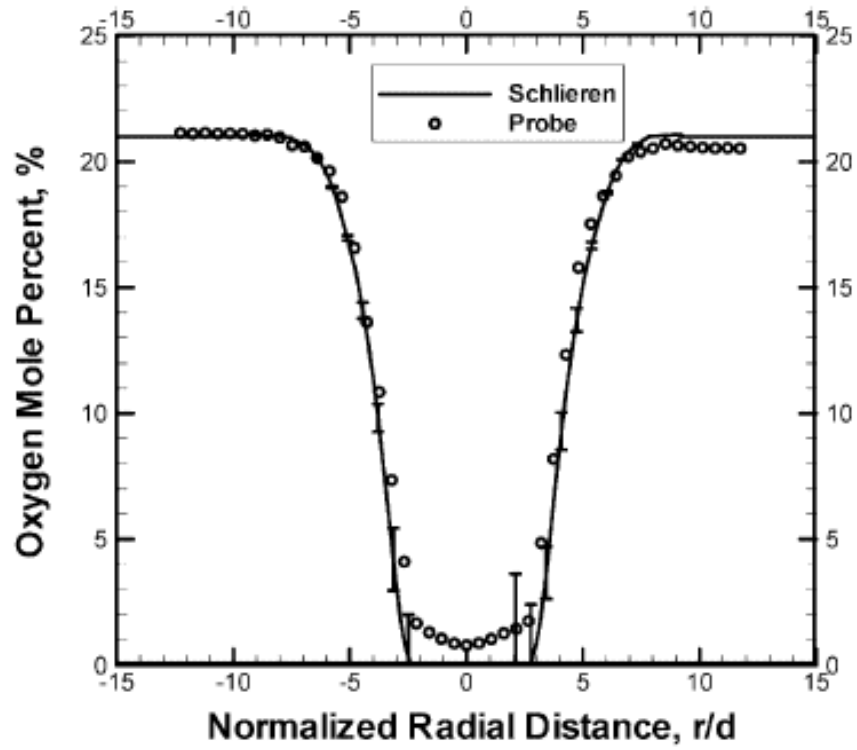


Figure 2.9 Radial profiles of oxygen mole percent at the axial plane  $Z = 5$  mm.

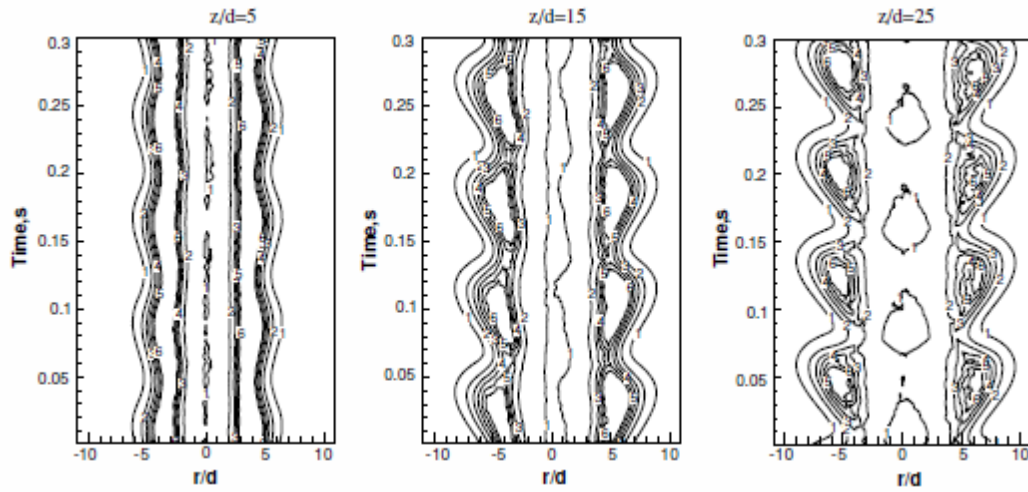


Figure 2.10 Temporal evolution of the temperature field for 1000 fps,  $Re = 300$ . (Contour levels are 1:400 K, 2: 800 K, 3: 1200 K, 4: 1600 K, 5: 2000 K and 6 :2300 K.)

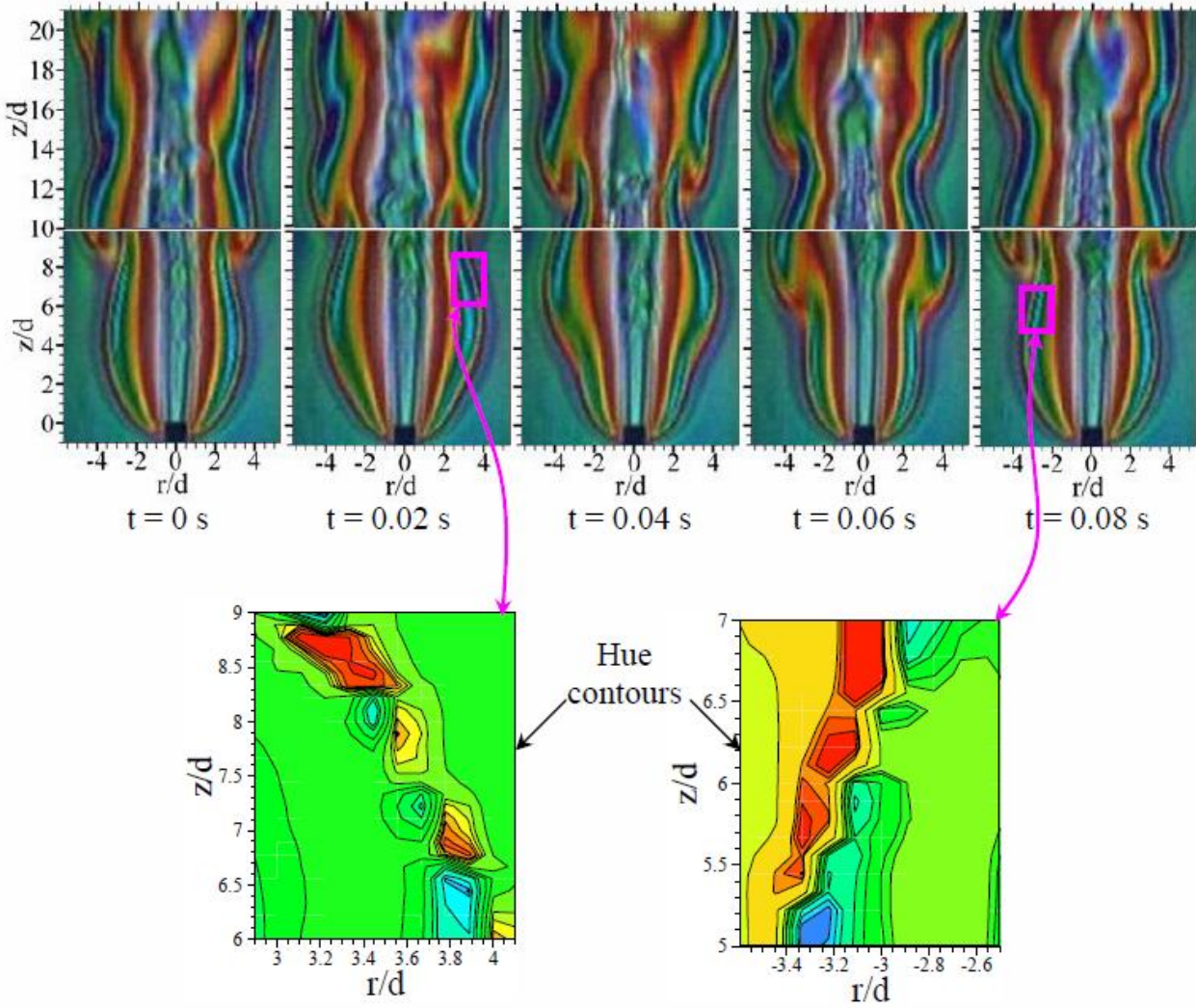


Figure 2.11 Instantaneous schlieren images during an oscillation cycle ( $Re = 1550$ ,  $Ri = 3.76 \times 10^{-4}$ ,  $Gr = 93.6$ ,  $d = 4.2$  mm,  $V = 37.5$  m/s)

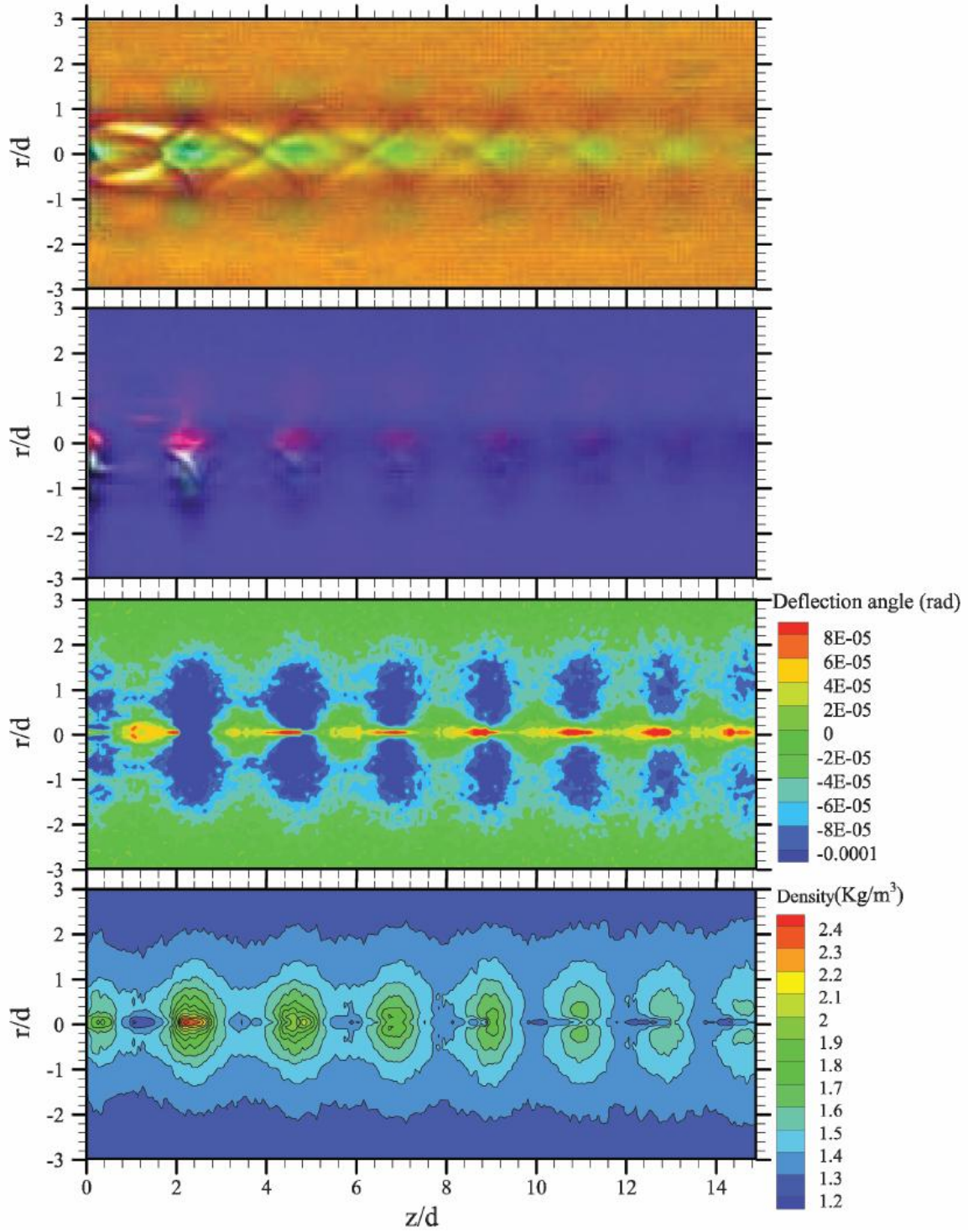


Figure 2.12 Test results for  $P_s = 860$  kPa showing a) rainbow schlieren image using a symmetric filter, b) rainbow schlieren image using an asymmetric filter, c) contour plot of deflection angle, and d) contour plot of density field.

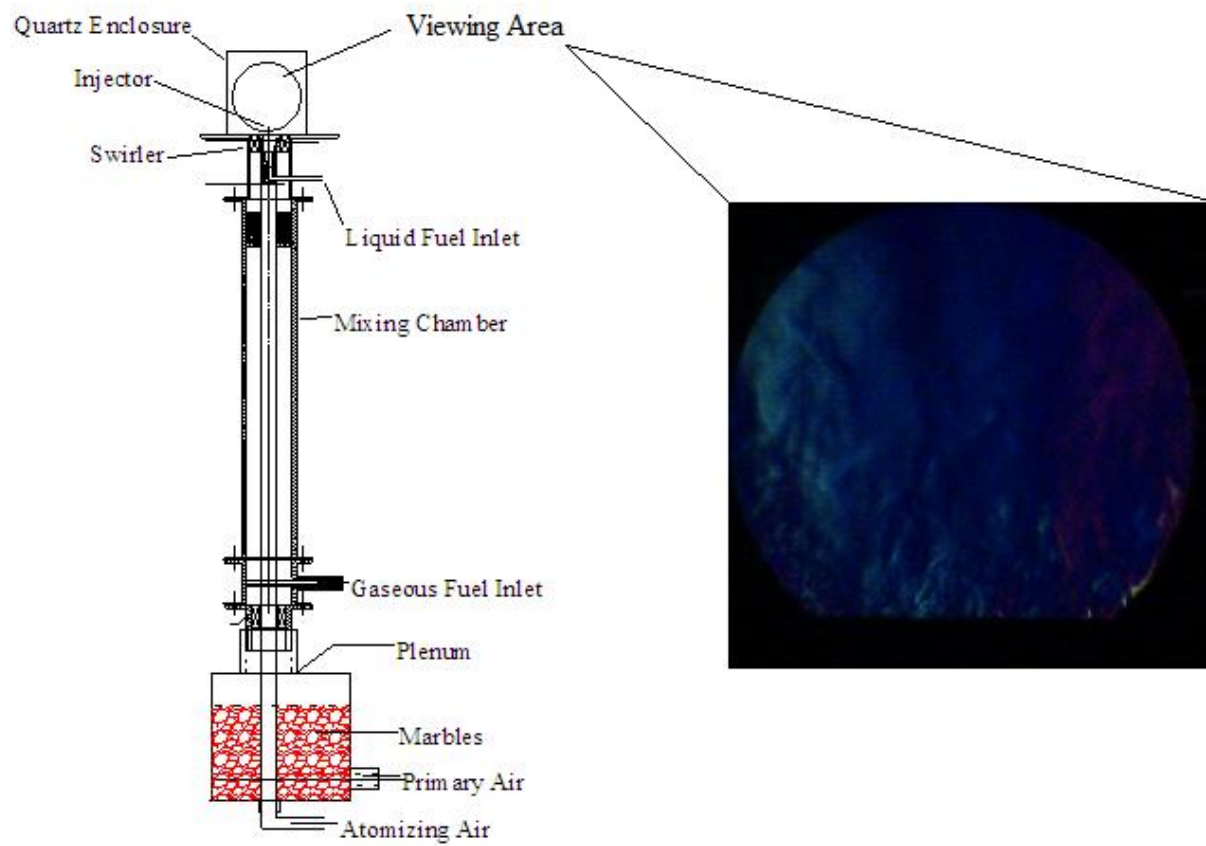


Figure 2.13 Details of lab burner (left). Crop of viewing area (right).

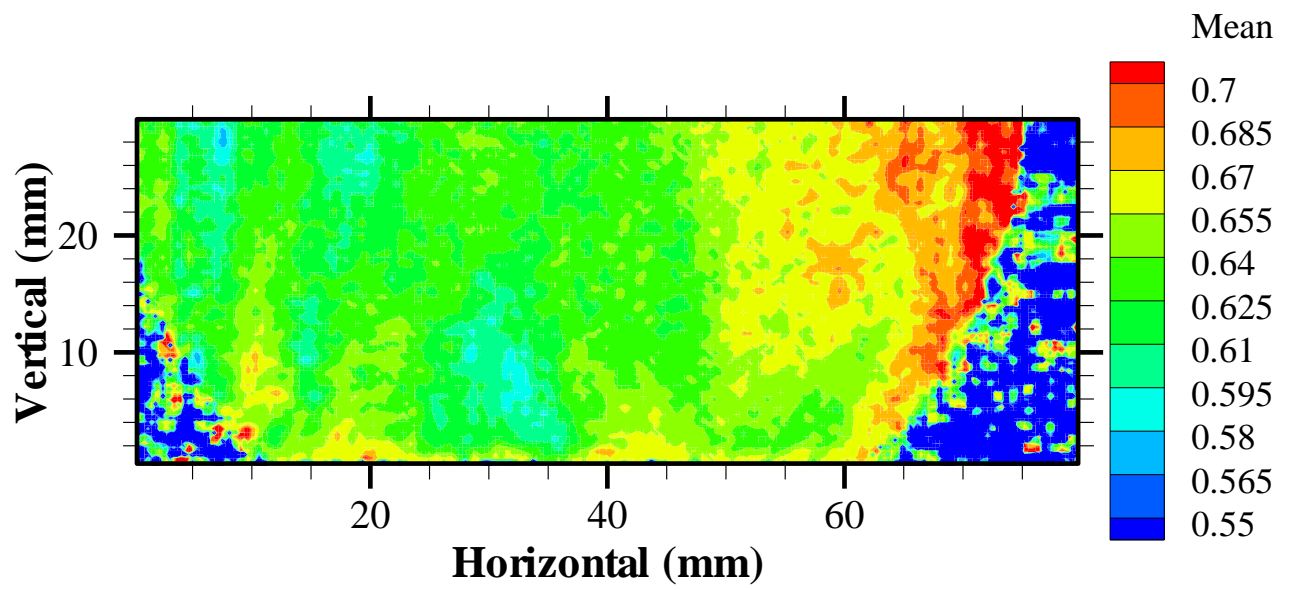


Figure 2.14 Calculated mean hue of combustion frame over entire duration of experiment

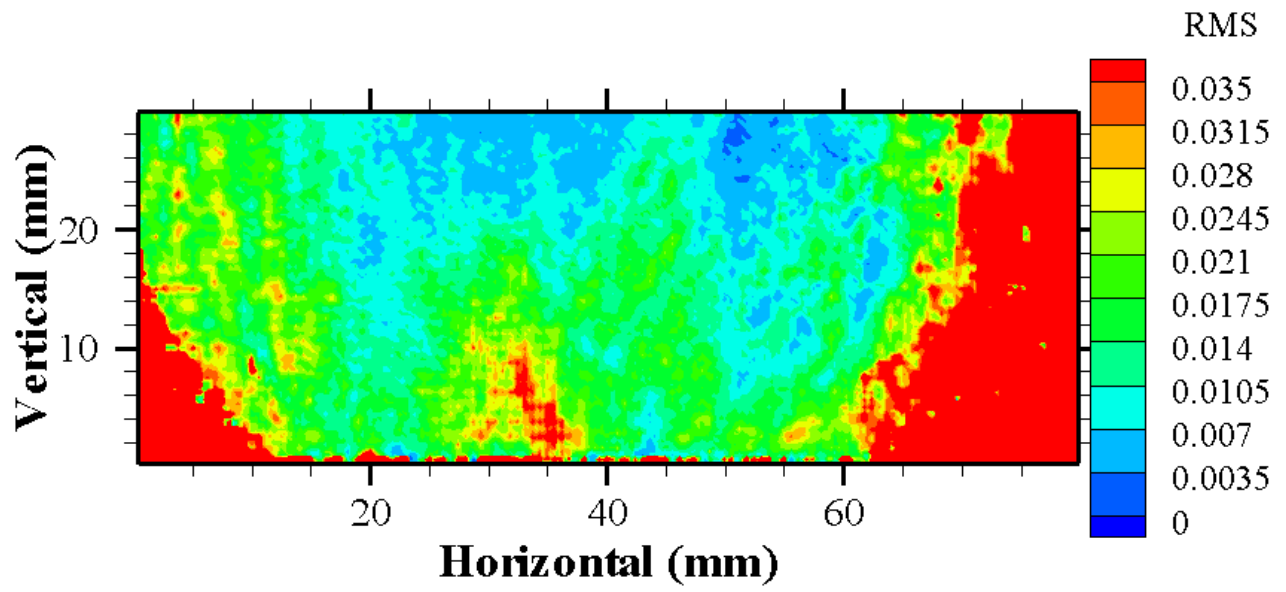


Figure 2.15 Calculated root mean square of hue in combustion frame over entire duration of experiment

## CHAPTER 3

### EXPERIMENTAL SETUP

#### Overview

The RSD technique has proven to provide accurate quantifiable measurements of density within steady and unsteady flow fields. These measurements have been obtained with high spatial and temporal resolutions. The RSD technique has previously never been applied to detect the small density variation resulting from pressure fluctuations in acoustic waves. However, with recent advances in ultra-high speed digital video photography and availability of precision optics, the possibility of capturing sound wave propagations has now been made possible. The current study describes an experimental setup that has overcome the challenges of detecting acoustic waves emanating from supersonic jets. Thus ultra-high speed rainbow schlieren deflectometry (UHS-RSD) can provide a non-intrusive way to detect acoustic signatures that previously could only be obtained with intrusive sound probe arrays at much lower spatial resolution.

The UHS-RSD method has key advantages over conventional techniques for measuring sound. First, the information from the flow field is obtained non-intrusively, which prevents interferences from the measuring devices. Second, data are obtained across the whole flow field and in real-time. The current research utilizes the capabilities of the UHS-RSD technique to characterize the acoustic field across the whole field of view. Information obtained can then be used to relate the flow characteristics in the near and far acoustic fields in supersonic jets.

This chapter first examines the challenges faced in optically detecting acoustic sound waves. Then details and specifications on the equipment used to develop UHS-RSD technique are discussed. Experimental processes for both the UHS-RSD system and the flow system are discussed. Finally, optimization techniques are examined to best utilize the optical components.

### Diagnostic Challenges

There are several diagnostic challenges to overcome to design an RSD experimental setup to capture sound wave phenomena from supersonic jets. First challenge involves the measurement sensitivity to pressure waves. Sound propagates as a pressure wave, however these pressure waves affect the refractive index difference. For very intense sound level of 150 decibel (dB) we can expect variation in refractive index difference of only 0.65 %. Table 3.1 presents the refractive index difference change for various sound pressure levels. Appendix B shows the calculation method to determine the refractive index difference change. Thus, a UHS-RSD system must be able to measure very slight changes in the refractive index difference.

Another design challenge involves the propagation speed of sound waves. The average speed of sound in ambient air under normal pressure and temperatures is 340 m/s. Sound waves are visualized within the field of view limited by the diameter of achromatic doublet lens employed, which is around 80 mm. Thus, a sound wave would travel from one end of the viewing area (lens) to the other in just under 240 microseconds. To perform a detailed analysis, multiple waves must be captured within the field of view. Thus the challenge of acquiring images at high temporal resolution must to be addressed. Image acquisition rate exceeding 150,000 Hz with over 200,000 image captures is desired for detailed analysis. Smaller framing rates result in sound wave fronts propagating large distances between consecutive images.

Table 3.1

Refractive index difference change due to sound pressure level

Sound Pressure ( dB )	Refractive Index Difference Change ( % )
160	1.974%
150	0.624%
140	0.197%
130	0.062%
120	0.020%
110	0.006%
100	0.002%
90	0.001%

The third challenge is based on the wave length of sound waves. For available acoustic wave frequency range of 20 to 100,000 Hz, the sound wavelength varies from 17 meters to 3.4 millimeters. In order to track the smallest wavelength a resolution twice the smallest wavelength is needed. Thus, to capture and track high frequency wave fronts a high spatial resolution system must be developed.

### Equipment Details, Specification, and Setup

#### *Flow System*

In this study, the supersonic jet is created by using a high pressure pneumatic system exhausting compressed air into the atmosphere through a converging-diverging nozzle. Figure 3.1 shows a block diagram of the compressed air system. Industrial grade compressed air is stored in a Size 300 Airgas cylinder storage tank. Connected to the CGA590 cylinder outlet valve is a 2,450 kPa (500 psi) Airgas pressure regulator. (note: the regulator pressure output allowed up to 5,200 kPa (750 psi) outlet pressure by adjusting a set screw on the pressure regulator). The output pressure from the regulator valve is set up to 4,830 kPa (700 psi), and the

air is allowed to fill the system controlled by a globe valve near the nozzle exit where measurements are acquired. Approximately 2.5 meters of metal 19 millimeter diameter flexible tubing is used to supply the air to the experimental testing area. A vertically positioned Velmax traversing rail is used at the end of the tubing to provide vertical movement of the nozzle exit. An easy access globe valve is used after the traversing rail to quickly open or close the air pressurized system.

To supply air to the nozzle a stagnation chamber was constructed which also provided accurate pressure reading after the globe valve and upstream of the nozzle exit. Figure 3.2 shows a drawing of the stagnation chamber and Figure 3.3 shows a photograph of the stagnation chamber. Figure 3.4 shows how the stagnation chamber is connected to the compressed air system. The bottom inlet is the intake for the compressed air. The upper inlet is to connect a pressure gage to read the stagnation pressure in the chamber. At the top of the stagnation chamber is the location to screw-in the C-D nozzle. The C-D nozzle has a throat diameter of 2 mm and an exit diameter of 3 mm. Figure 3.5 shows a detailed diagram of the C-D nozzle. Using the area ratio of the exit to the throat of the nozzle an exit Mach number can be calculated. This nozzle configuration gives a exit Mach number of 1.85.

The globe valve is opened to obtain each set of experimental data. The duration for the opened valve lasts approximately a few seconds. Schlieren images were captured at several different axial field of views along the jet flow. A traversing mount was used to adjust the Z direction (Stream wise distance from the jet exit) between experimental runs. A range of Z/D (Z direction normalized by nozzle exit diameter) from 0 to 25 was used to acquire near field data. In order to achieve the desired span, two separate experiments were conducted. At each successive run the nozzle exit is traversed downward to provide image data further downstream of the exit.

There was a 60 minute waiting period between runs to allow transfer of image data from the camera to the computer. Care was taken to make sure that ambient conditions were strictly regulated in an attempt to achieve fixed operation conditions.

### *UHS-RSD System*

The small scale pressure fluctuations that result from the turbulence interactions in the jet result in small pressure fluctuations that can be difficult to detect. Therefore, care must be taken in the experimental setup to assure that each optical component is appropriately utilized. Since sound waves traverse at high speed and high frequency, an experimental setup must be employed that can provide the sensitivity and spatial and temporal resolutions needed to resolve the acute air density fluctuations. Figure 3.6 shows a schematic of the experimental setup for the UHS-RSD system. Presented in Figure 3.7 is a photograph of the rail system positioned on an optical table that is utilized for UHS-RSD experimentation. The rail system is setup on a pneumatic optical table to maintain optical alignment and reduce vibrations experienced from nearby equipment. This reduction in ambient vibrations is critical, because vibrations from HVAC systems can cause disruptions in the flow field.

An Energetiq air cooled EQ-99-FC-S LDLS (Laser-driven light source) system was used to provide steady broadband white light for the UHS-RSD experimental setup. This is a class of solid state plasma light sources where a laser focuses on a gas enclosure creating a plasma that acts as an intense and highly stable light source. Figure 3.8 shows a photograph and description of all the assemble parts to the light source. The LDLS system provides broadband white light in the 170 to 2,100 nm range. The advantage of this light source compared to standard light sources is the even power distribution over the entire spectrum of emitted light. Figure 3.9 shows the

spectral performance of this system over the emitted spectral range. The light source assembly is positioned away from the table to prevent vibrations from its electronics affecting the experimental setup. From this light source a 600 micrometer single strand fiber optic cable is connected to a mounting box that is radially centered down the path of the system setup.

At the exit of the mounting box is a 5  $\mu\text{m}$  wide by 3 mm high source aperture. The aperture is positioned at the focal point of an achromatic collimating lens with a diameter of 82 mm and focal length of 300 mm. Thus light captured by the lens is redirected into parallel light rays passing to the jet flow forming the test media. The source aperture is oriented such that its height is aligned with the streamwise direction of the flow field. Light passing through the test media (flow field area) causes deflection in the light rays due to density gradients present in the jet flow field. Deflected light rays exit the test media to reach the de-collimating lens of 102 mm diameter and 1000 mm focal length. The light rays are converged onto a rainbow filter placed at the focal point of the de-collimating lens. This setup results in a source aperture magnification factor of 3.33 based on Equation 2.1. Therefore, the source aperture image on the filter plane will be 16.7  $\mu\text{m}$  wide. The height of the source aperture image is not important for analysis because the deflection angles are measured in the transverse direction only. The rainbow filter is a continuously graded color filter printed on a 35 mm slide film. This filter is a 0.5 mm wide color strip with hue varying from 40 to 320 degrees. An asymmetric color range filter was used and an example is shown in Figure 3.10. The colors vary linearly along the transverse direction of the rainbow film, and the light source is centered within this hue range to provide the best sensitivity of the resulting image on the camera. The light rays passing through this filter are focused onto a camera sensor with a camera lens positioned as close to the filter as physically allowed.

Figure 3.10 shows a photograph of the rainbow filter and camera setup for the UHS-RSD experimental setup. The camera lens, a Sigma 105 mm lens, is used to focus the test media onto the camera sensor. The camera is a Photron Fastcam SA5 high speed digital camera. Each acquired image is a 128x128 pixel resolution frame that is digitized and stored as a 16-bit color TIFF file. This resulted in a spatial resolution of 406 microns/pixel. Video images are captured at 262,500 frames/second with a temporal resolution of 3.81 microseconds. The acquired images are downloaded by a 1 Gb/s cat6 cable to a computer for further processing.

### UHS-RSD System Optimization

Each component in the schlieren setup affects the overall measurements. Months of testing have helped to determine best practices for optimizing an experimental setup based on the needs of the experimenter. The following sections describe the different equipment tested and how it affected the overall measurement capabilities.

#### *Light Source*

The light source is the primary piece of equipment that affects the UHS-RSD setup capabilities. Since the color filter used in the UHS-RSD technique is in the visible light spectra broadband white light is required. Many light sources were tested and it was determined that the light sources with a flat power spectra over the visible light range provided the best results.

The first tested light sources were basic light emitting diodes (LED) lights. After testing with LED lights it was determined that the light intensity was inadequate to acquire images at temporal resolutions needed to capture sound pressure wave propagations.

A LIFI high powered solid state plasma light source was tested. This light provided high intensity light that allowed framing rates of 300,000 frames per second to be achieved. However, the light power spectrum was non-uniform and the high heat of the light source would melt and warp the optical fibers and slit aperture.

A LDLS solid state plasma light source provided the best (most even) light spectra across the visible light range. The spectrum for this light source is presented in figure 3.9 and was discussed previously. The LDLS light source provided high light intensity needed to acquire quality images at up to 265,500 frames per second.

### *Slit Aperture*

The slit aperture width along with the focal length of the collimating and de-collimating lenses is a major factor in determining the color resolution of the experimental setup. The larger the slit aperture dimensions the larger would be the source image on the filter plane. For measuring very slight pressure fluctuations in sound waves a high color resolution is needed, which requires a small aperture width. After several trials, a 5 micrometer width slit aperture was determined to be the best because it was the smallest available aperture, which still allowed sufficient light throughput.

### *Collimating Lens*

The collimating lens diameter affects the light throughput in the system. The important factor to consider is the ratio of focal length to the diameter of the lens. Light leaves the slit aperture and diverges conically outward. Therefore, a small focal length / diameter lens tends to

maximize light collection and throughput. However, excess light outside of the lens surface is wasted light.

Several focal length lenses were tested. A 250 mm focal length lens was tested, but the lens quality was poor and significant lens abrasions prevented accurate measurement data. A 500 mm focal length lens was tested but the lens was too far from the slit aperture and light throughput through the system was significantly reduced. Finally an 82 mm diameter lens with a 350 mm focal length was tested. It has been determined that this lens provides the best light throughput with minimum optical aberrations.

#### *De-Collimating Lens*

The de-collimating lens has a large impact on the system sensitivity. Large focal length results in large ray displacements on the filter plane needed for high measurement sensitivity. Several focal length de-collimating lenses were tested. Initial predictions suggested that a larger focal length lens would improve sensitivity. Thus a 52 mm diameter lens with a 2,000 mm focal length was tested. However with this larger focal length lens, chromatic aberration produced greater color non-uniformity in the background image compared to smaller focal length lenses available. It is also believed that with the larger focal length lenses inaccuracies exist in the focus point of individual light rays depending on the wavelength of the light ray. After several trials a 101 mm diameter achromatic lens of 1000 mm focal length was tested. Selection of this lens reduced sensitivity to light ray deflection, but provided a benefit to increased surface quality. The larger diameter of the lens also provided a larger field of view. This lens was selected for de-collimation.

### *Filter Selection*

Narrow width color filters provide the greatest sensitivity to pressure fluctuations. However, printing techniques limit the smallest color strip possible. Filter sizes below 0.5 mm introduce poor color accuracy. 1.0 mm and 0.75 millimeter wide filters with a hue range of 30 to 250 were tested. These filters did not provide the color resolution needed for a highly sensitive experimental setup. A 0.5 mm wide filter with hue varying from 30 to 250 degrees was finally created and selected. This filter provided the best color resolution for high sensitivity measurements.

### *Camera Lens Selection*

Several different camera lenses were tested. A camera lens with a wide field of view, small f-stop, and a high depth lens is desirable. A 105 mm Sigma fixed focal length lens was tested. This provided the best field of view and pixel resolution; however the light throughput through the lens was poor. A Pentax 50 mm lens was tested, but the resulting pixel resolution was poor. A Sigma 105 mm lens provided the best performance. This lens provided high pixel resolution and allowed high light throughput through the lens.

### *Framing Rate*

To measure pressure waves in the acoustic regime high temporal resolution must be achieved. Different framing rates were utilized. However, at higher framing rates the field of view is reduced by the digital camera. The lowest framing rate that allowed visualization of a moving sound wave front was around 150,000 Hz. However, wave fronts would change by large increments of up to 10 pixels between captures. This would reduce the accuracy of the analysis

procedure. Thus, the framing rate was increased while the light throughput was adequate to acquire good quality images. The maximum image framing rate achieved was 265,500 Hz.

## Optical Procedures

### *Optical Alignment*

Care must be taken when optically aligning the RSD system. Small misalignments on the order of a millimeter can completely derange the system and produce images that will not provide meaningful results. Systematic placement of optical components starting at the light source and progressing towards the camera results in the desired optical alignment. The optical components were mounted on an optical breadboard placed on top of a level correcting pneumatic table. Some of the components were placed on an optical rail mounted on the breadboard to assure perfect alignment.

The light source and slit aperture are the first items to place. A single mounting assembly was constructed so an optical fiber screws into a mount and a slit aperture is placed at the front of the assembly. Here the light source was placed behind the slit aperture to maximize light throughput to the system. The closer the light source optical fiber outlet is placed to the aperture the better the light throughput. However, the metal on the source aperture can be very sensitive to pressure exerted by direct contact with the optical fiber. If contact is made between the slit and the point of light emission the metal on the slit can be warped and deformed. This has adverse effect on the whole system. Further the end of the optical fiber where the light is emitting can produce high temperature. Direct contact of the fiber with the slit can heat up the slit and cause deformation. The light mount assembly is held in a vertical optical pole post holder that allows fine adjustments in the vertical direction. The post holder is mounted on two single axis crossed

roller translation stages that allow micrometer adjustments parallel and perpendicular to the optical path.

The collimating lens is then placed so that the focal point of the lens is exactly at the slit aperture surface. The lens is held in a metric bar-type holder and mounted on the breadboard by a vertical adjustment post holder. This mount is adjusted vertically so that the center point of the lens is at the same height as the slit aperture while the horizontal distance between slit and lens is equal to the focal length of the lens. To verify that the lens is placed at the correct location observations are made to ensure parallel light rays; i.e. the diameter of the bright image formed by the lens remains the same in the downstream direction. To accurately measure lens image diameter an alignment guide was created by drawing two concentric circles equal to the diameter of each achromatic lens as shown in Figure 3.12. The guide is placed at several locations along the optical path to check if the lens image is of the same diameter. This check continues till the wall of the lab is reached. At any point that the diameter of the light falls inside or outside of the guide an adjustment is made to the location of the slit aperture mount or lens mount to correct the diameter of the image and thus, proper positioning of the lens.

The de-collimating lens is then placed in the optical path so that the light passing through both lenses is concentric. The mounting setup for the de-collimating lens is similar to that used for the collimating lens. The horizontal distance between the two lenses is determined by the test media placed in-between.

The rainbow filter film is then placed at the focal point of the de-collimating lens. The mount for the rainbow filter is similar to the mount for the light fiber, however a rail mount guide is used to traverse the filter. The de-collimating lens is subject to manufacturing inaccuracies in the actual focus point of the lens. Thus visual observations are used to assure that

the filter is at the correct location. The filter is at the correct location when the image size of the slit aperture at the filter plane is the minimum.

The high speed camera and camera lens assembly is then mounted behind the filter mount. The camera is connected to a vertical adjustment post holder secured to a rail mount. The camera lens should be positioned as close to the rainbow filter as possible without making physical contact with the filter. The camera is connected to a computer via a one GB/s CAT-6 cable.

### *Light Source and Camera*

The light source is controlled via a control switch attached to the main laser housing case as shown in figure 3.8. A switch is flipped to operate the light source and a waiting period of up to two minutes must be observed before light at full intensity emits through the 600 micron fiber optic cable. With light turned-on the power button on the camera is switched on and the PFV camera software is started on the computer. A circular image of the field of view will appear on the screen. With the dimension of the smallest diameter achromatic lens used, the spatial resolution of the system setup can now be determined. The pixel selection tool is used to determine the number of pixels in the image on the display. The spatial resolution is found by dividing the lens diameter by the number of pixels in the image. The spatial resolution remains constant for a given optical setup.

The image framing rate, exposure time, and image size are then selected from the appropriate control buttons in the PFV software. When these parameters are set or anytime these parameters are changed the camera must be re-calibrated. To calibrate the camera, the camera lens is covered by a thick cardboard cutout to prevent light passing to the camera sensor. Next,

the shading button on the PFV software is selected and calibration is performed. The camera cover can now be removed.

### *Calibration Curve Capture and Generation*

A calibration curve for the experimental setup must be generated to relate image hue measurements with ray deflection angle. The calibration process relates transmitted hue to the transverse position on the filter plane. With no flow in the test area, the rainbow filter is traversed in the transverse direction until only the color on the edge of the filter strip is present in the background image. This image is captured as a single snapshot image by selecting the snapshot button in the PFV software. Next, by using the micrometer adjustment knob on the filter's single axis crossed roller translation stage the rainbow filter is traversed by a desired amount, typically 0.1 mm. In doing so the color in the background image changes by a small amount. The background image is again acquired for this filter position. The process is repeated until the other edge of the filter is reached. The filter calibration curve for each pixel can then be generated by plotting the hue value at each pixel location with the transverse distance on the filter plane. Figure 3.14 shows a typical filter calibration curve for pixel to pixel calibration.

### *Capturing Background and Experimental Images*

Two sets of image videos must be acquired for each experiment. One set of images pertains to background images or images with no flow field. The second set of images is the experimental images with a flow field present. The camera can take up to three hours to download a full data set. Thus, care must be taken to ensure that each video capture is performed without disturbing the optical system alignment or the experimental setup.

A background location on the filter plane must be determined to acquire both sets of images. This can be determined by examining the filter calibration curve generated previously. The location on the filter calibration curve that was most sensitive to changes in transverse location is chosen as the background location for the experiment. This is the steepest part of the calibration curve. The filter is traversed to the desired background location on the filter plane and a video of the background image is acquired. Figure 3.13 shows an image of a background image acquired. The full data set is then saved to the computer via the PFV software interface. The TIFF image file format is used and the images are saved as 16 bit color image files. After the image transfer is complete, the experimental data are now acquired. The globe valve near the exit nozzle is opened to initiate the flow field. After a brief transient period the experimental images are acquired and downloaded to the computer hard disk.

## Experimental Procedure

### *Flow System*

The maximum pressure of the system is set at the pressure regulator at the exit of the Airgas compressed air cylinder. The largest pressure differential between the supply air and the ambient air around the C-D nozzle is desirable for obtaining the highest exit Mach number and thus stronger acoustic signatures from the jet flow. Thus the Airgas pressure regulator is typically adjusted to the highest set point pressure before the experiment is performed. While the near exit globe valve is closed the air line is checked for leaks.

Once any major leaks are taken care of in the line, calibration of the Velmax traversing rail must be done to assure accurate measurements. Calibration of the vertical traversing rail is started by first turning on the Photron high speed camera. The system must be properly aligned as discussed in the previous section. The field of view of the experimental test medium region is

displayed on the screen. Next, the rail is moved up or down until the nozzle exit is seen in the field of view on the computer screen. Any fine adjustments to the focus of the camera are made on the 105 mm Sigma camera lens. A base image is acquired to distinguish the start of the nozzle transversal. The nozzle is traversed in the vertical direction by turning the Velmax traversing rail's vertical adjustment knob. After one complete rotation of the adjustment knob clockwise or counter clockwise another image is acquired. Several images were acquired at different axial locations while recording the number of knob rotations it takes to achieve a particular nozzle exit location on the computer screen. The nozzle exit was then returned back down to the bottom of the image. This location represents a Z direction (axial location) of 0. All other locations could be determined based on the number of rotations of the traversing knob used to arrive at a particular axial location.

With the system under pressure, the globe valve is opened for sufficient duration to obtain experimental images. The globe valve is closed after the video capture process is complete. This period last approximately a few seconds. A range of  $Z/D$  from 0 to 25 was used to acquire acoustic field data from the jet exit. In order to achieve the desired span two separate experiments were run. At each successive run, the nozzle exit is traversed vertically downward to provide image data farther downstream of the nozzle exit. For each experiment, a background image set is acquired with flow and no flow. There was a 60 minute waiting period between runs to allow data to be transferred from the camera to the computer hard disk. Care was taken to make sure that ambient conditions were strictly regulated in an attempt to maintain constant operation conditions.

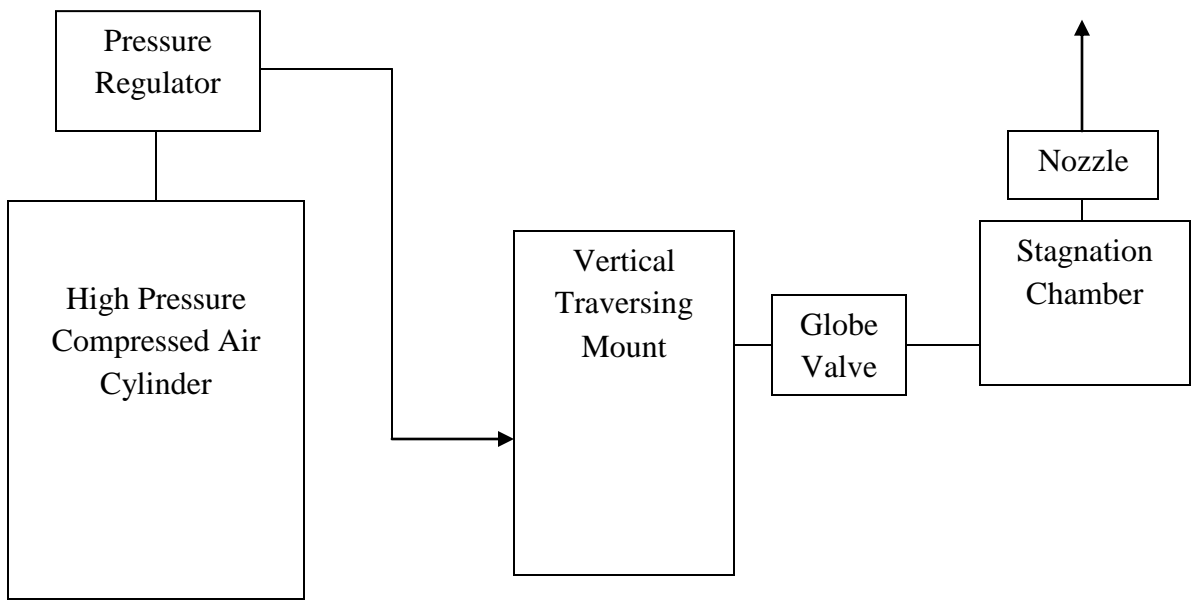


Figure 3.1 Air system block diagram.

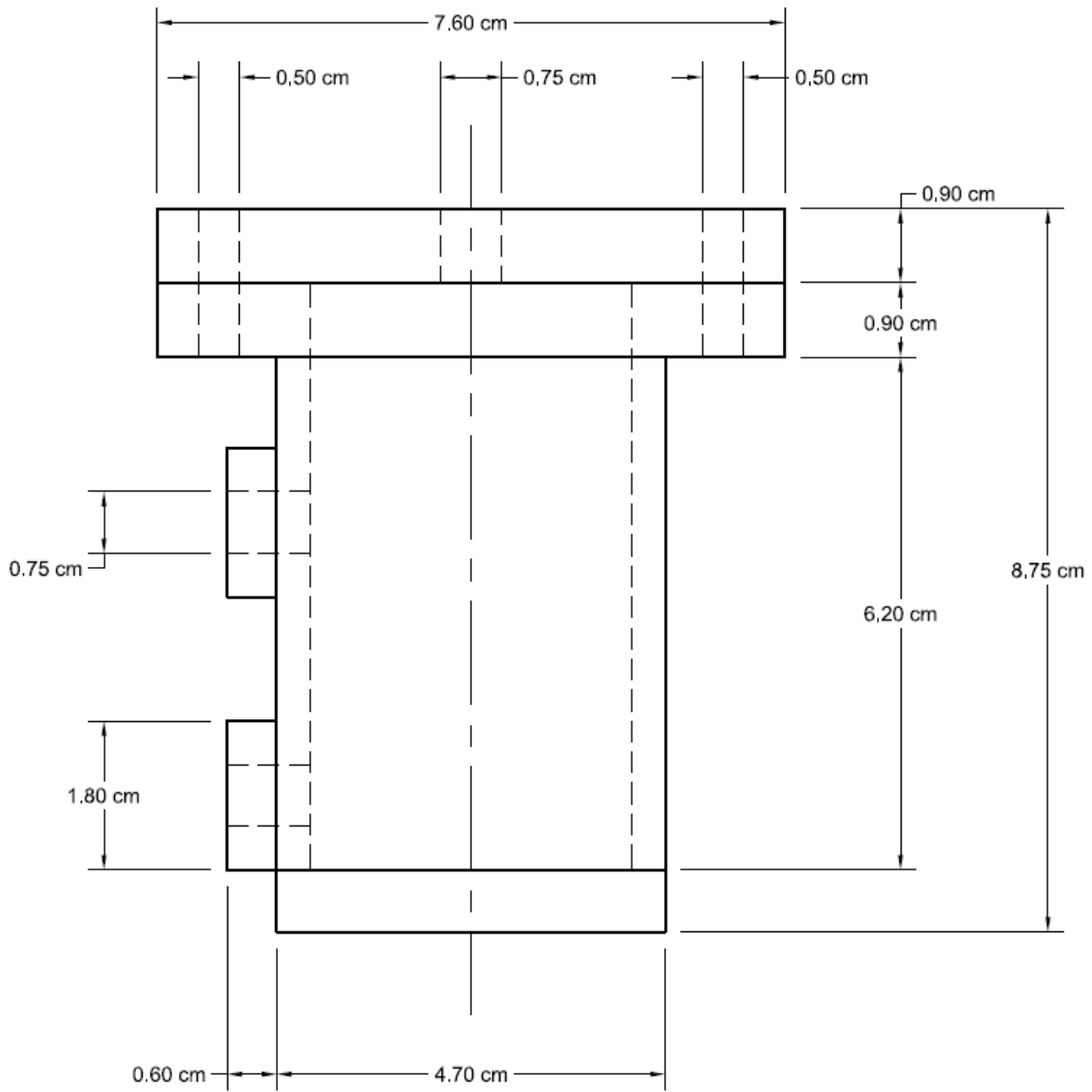


Figure 3.2 Schematic diagram of the stagnation chamber.

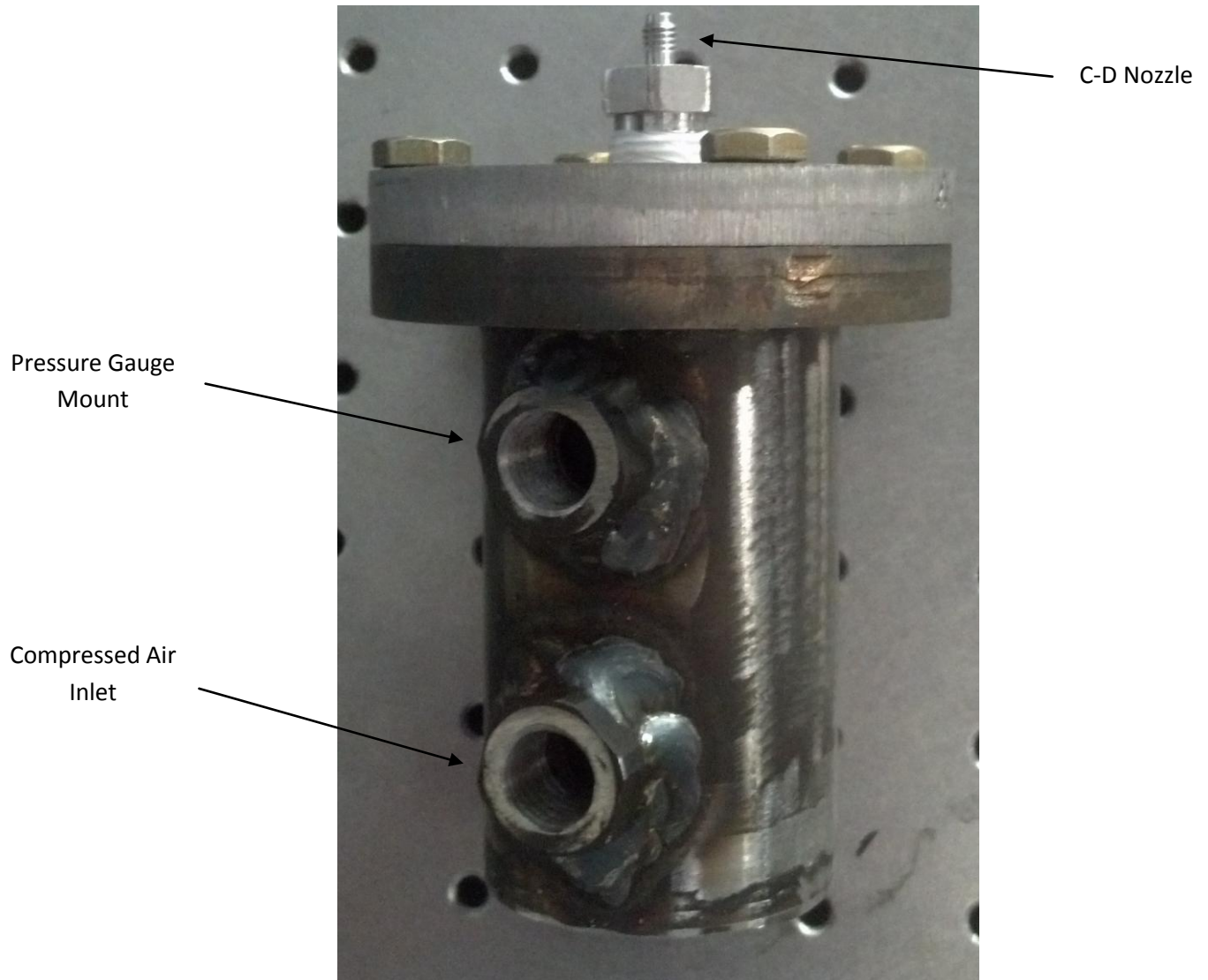


Figure 3.3 Photograph of stagnation chamber.

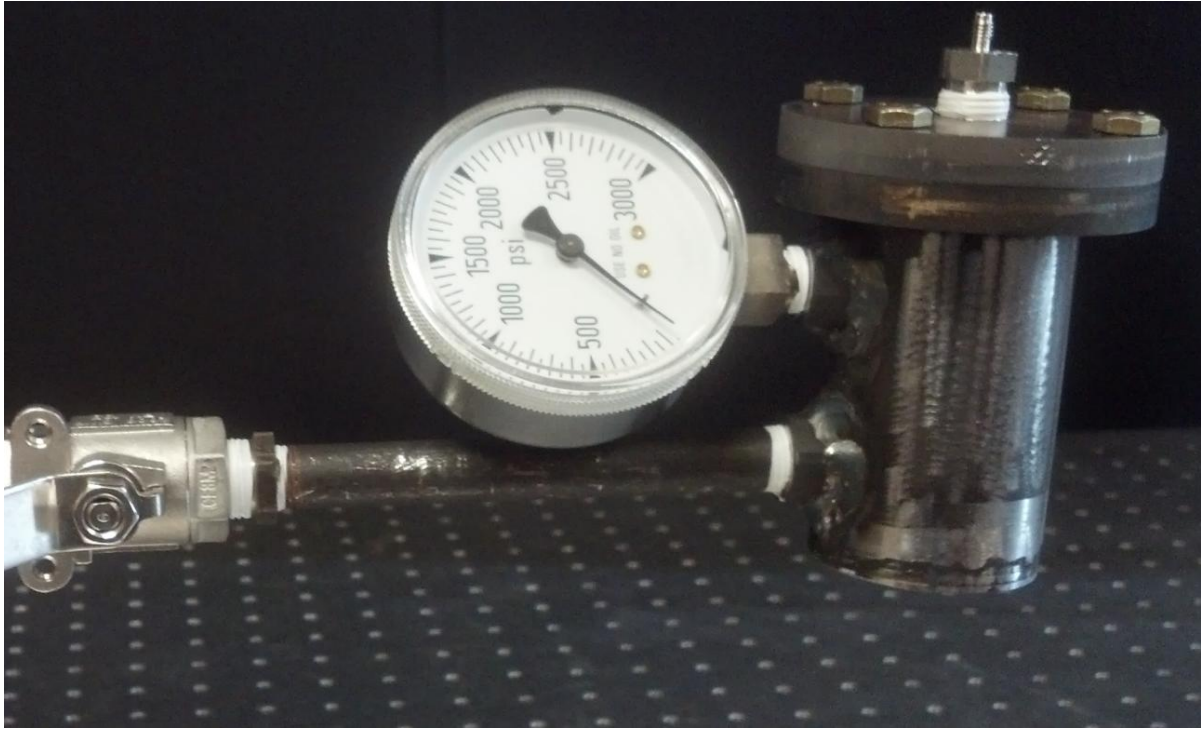


Figure 3.4 Photograph of mounted stagnation chamber assembly.

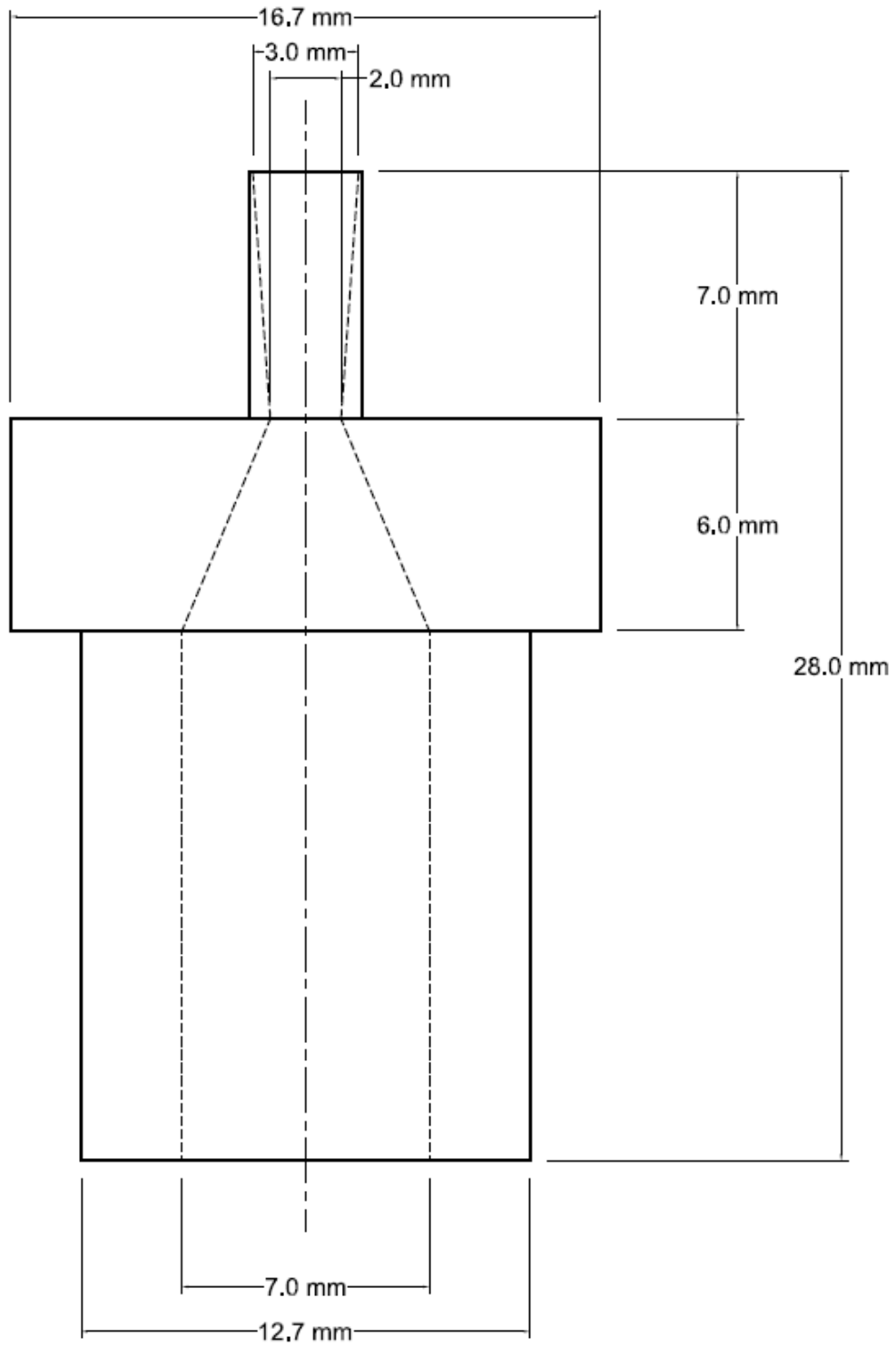


Figure 3.5 C-D nozzle schematic.

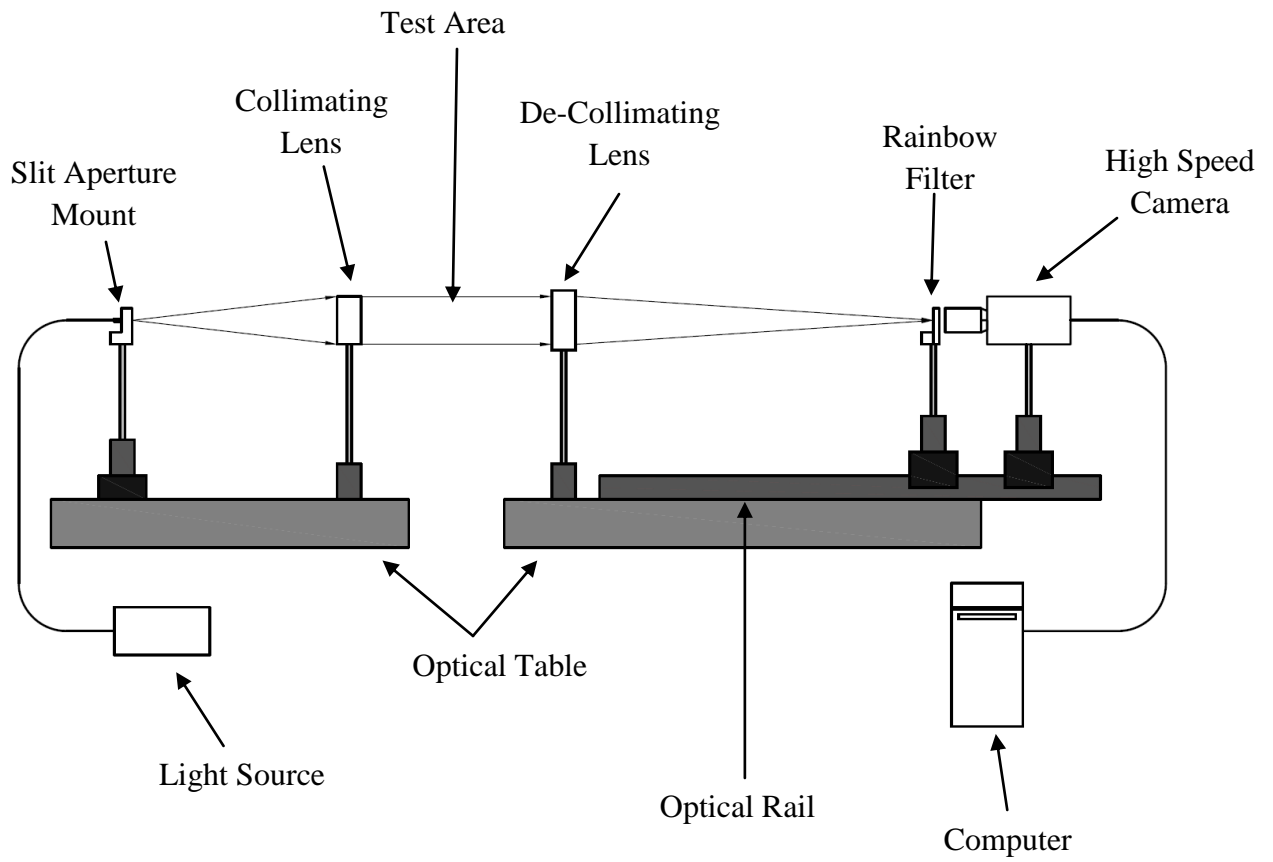


Figure 3.6 Experimental set up with schlieren apparatus, supersonic jet, and rainbow filter.

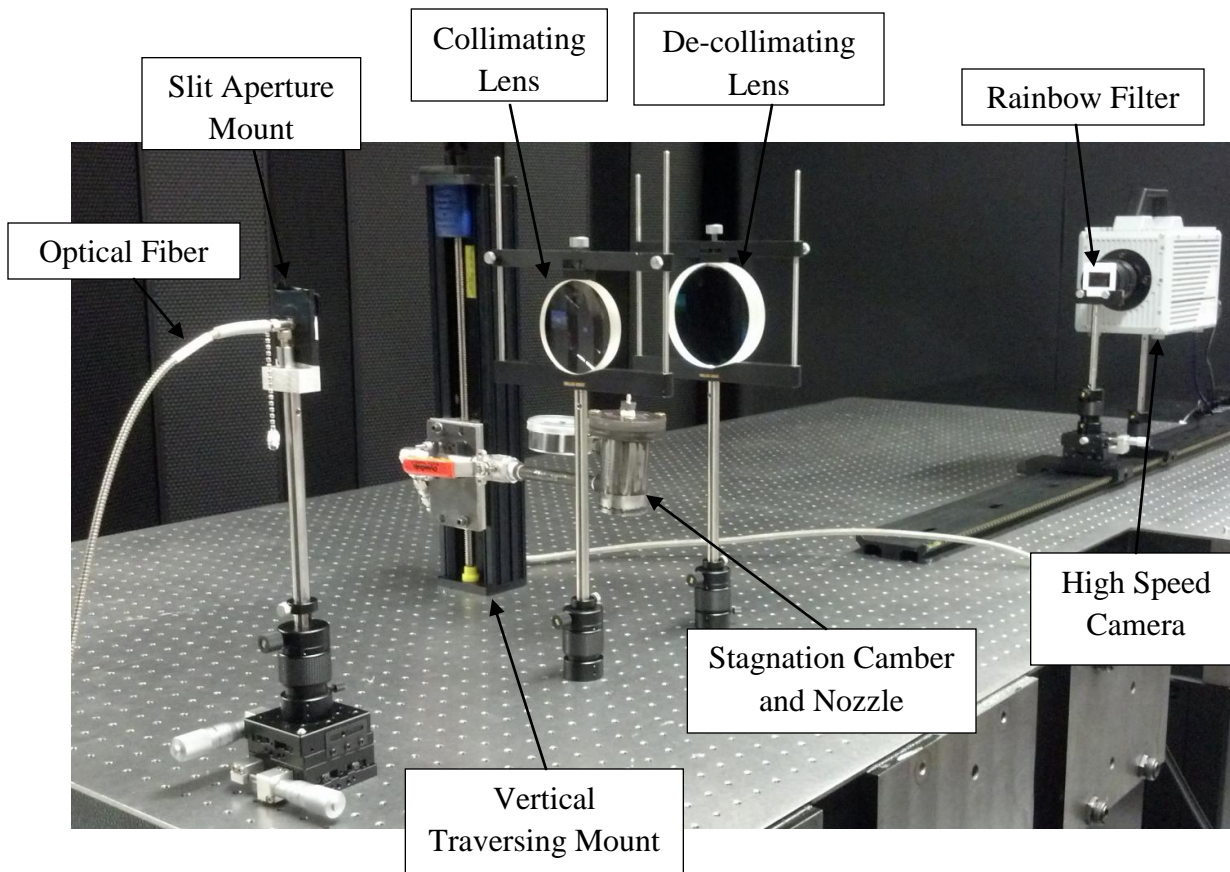


Figure 3.7 Optical System Setup

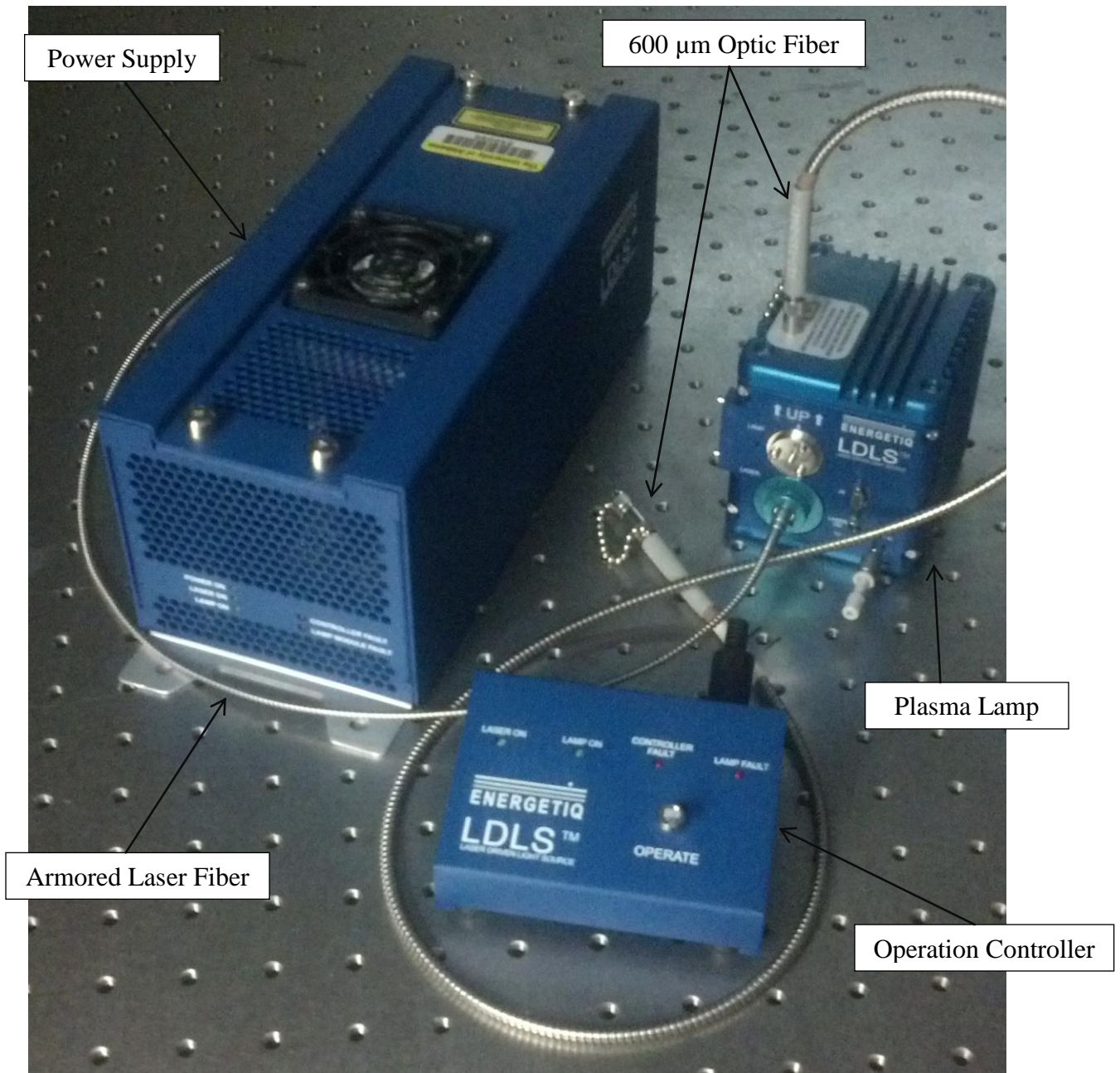


Figure 3.8 Energetiq LDLS Light source controls (bottom left), Lazer and power supply (right), and light distribution box (left)

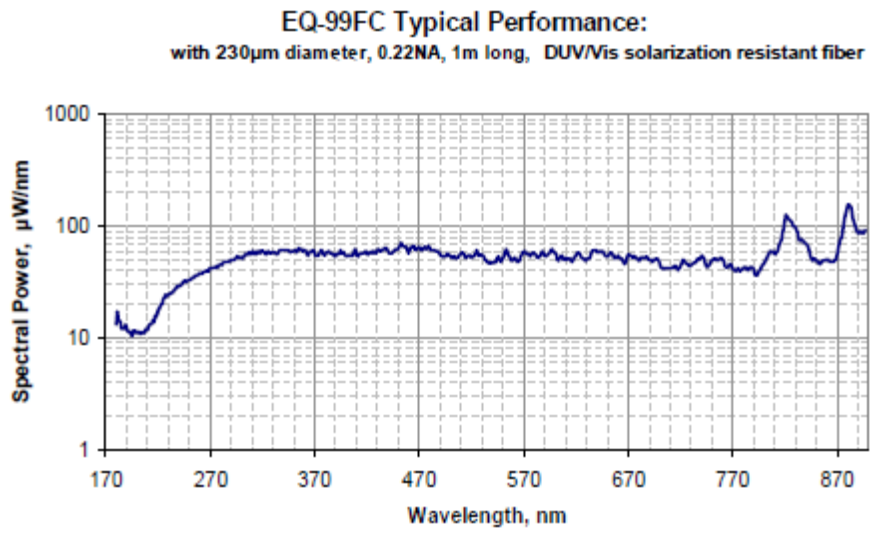


Figure 3.9 Performance spectrum of the Energetiq LDLS system.

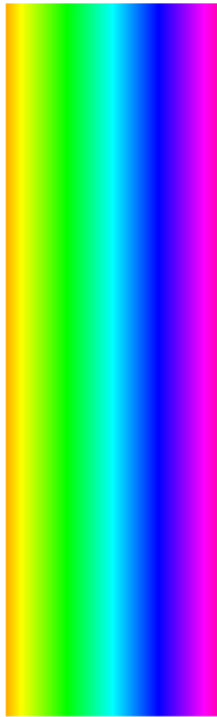


Figure 3.10 Asymmetric 0.5 mm rainbow filter.



Figure 3.11 Rainbow filter and camera setup

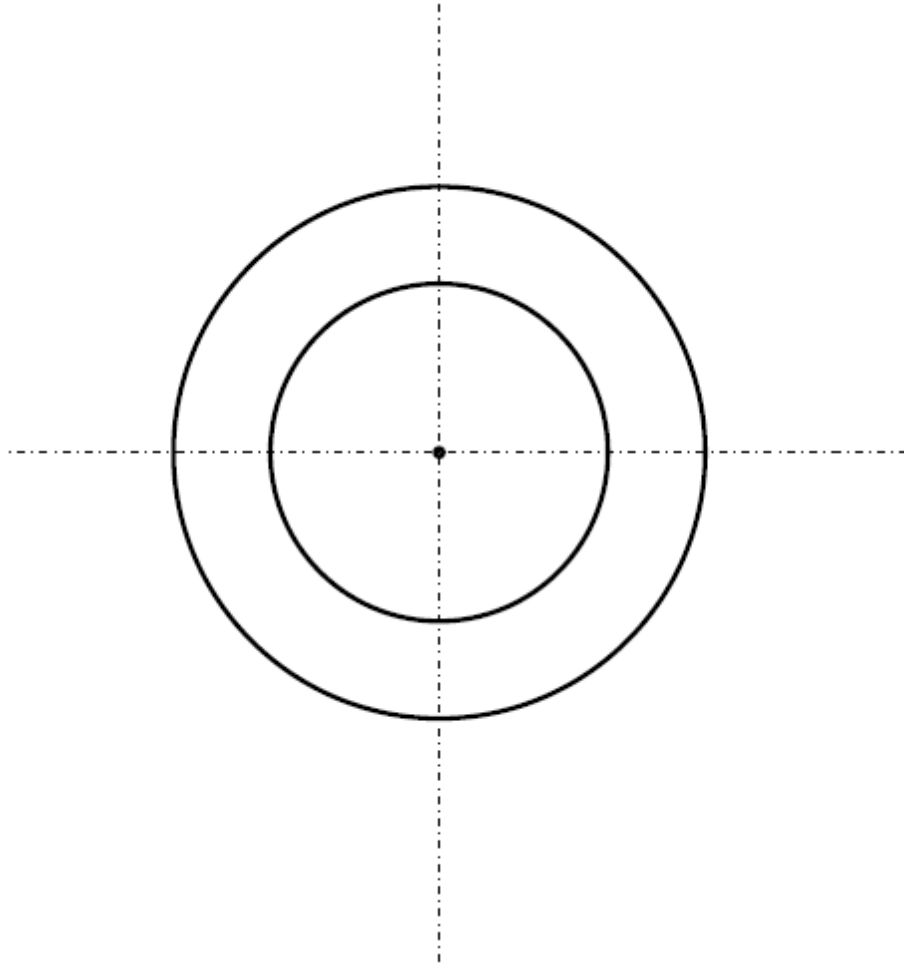


Figure 3.12 Alignment guide example



Figure 3.13 Example of background schlieren images at different traversing distances across the filter.

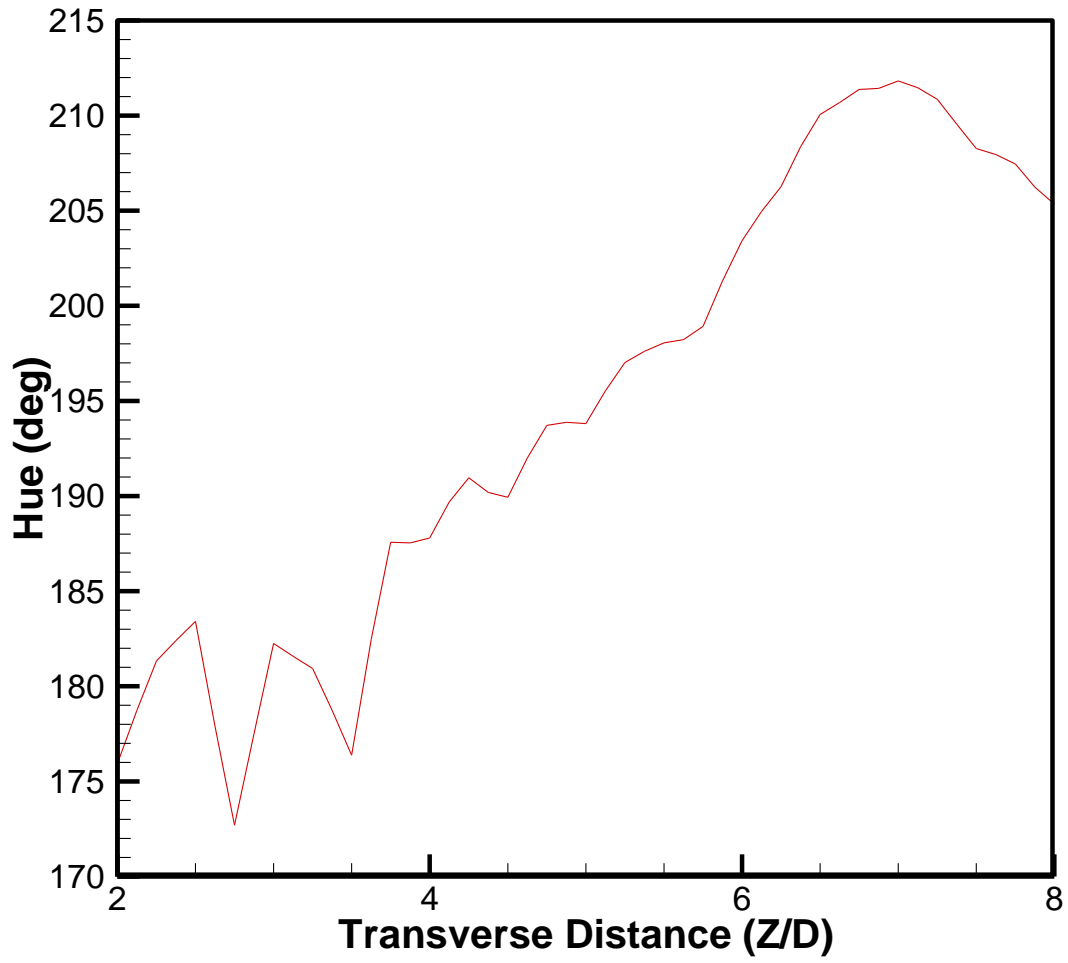


Figure 3.14 Filter calibration curves based on average image hue at a pixel.

## CHAPTER 4

### RESULTS AND DISCUSSION

#### Overview

UHS-RSD technique developed in this research provides real time images that allow insightful visual representations of acoustic field around supersonic jets. Different analysis techniques have been used to understand the guiding fundamental principles behind noise generation in these supersonic jets. First observations are made from visually inspecting the color schlieren images, which offers general insight into the jet flow characteristics. Acoustic Mach wave angle can be determined and a convective Mach speed can be predicted. Next analysis technique relies on statistics of hue difference between experimental and background images. Here, mean and standard deviation of hue difference will be computed to draw conclusions about the turbulent flow field. These statistics will also aid in determining optimal locations to place the rainbow filter and help in identifying filter regions where noise to signal ratio can be poor. Finally the Fast Fourier Transform (FFT) of hue difference will be used to obtain the frequency content of sound waves emanating from the jet flow. FFT analysis would aid in characterizing acoustic waves and their strength at various locations in the field of view.

## Visual Observations

Several observations can be made by inspection of the raw schlieren images. In figure 4.1 a sequence of schlieren images is shown to visually illustrate sound wave propagations. The field of view in these images is limited by the diameter of the smallest achromatic lens utilized in the experimental setup, which is the 52 mm de-collimating lens. The jet flow field is located on the far right of the schlieren images and the sound waves are shown as propagating to the left of the jet flow field. Only one side of the flow field is present in the schlieren images to maximize the observable acoustic zone. A sound probe is positioned on the far left of the images and can be seen as a small black rectangle on the edge of the image. However, because of poor signal to noise ratio no sound probe measurement data are presented in this research.

The images were captured at 210,000 frames per second (fps) and a pixel resolution of 406 microns per pixel. The nozzle utilized in this experiment was a two millimeter throat diameter and three millimeter exit diameter converging diverging (C-D) nozzle. Two separate axial views were acquired for these experiments. Figure 4.1a presents a view from  $Z/D$  of 19 to 27 and figure 4.1b shows a upstream view from  $Z/D$  of 9 to 18. Figure 4.1 shows a visual representation of the acoustic field around the jet flow. The jet flow on the right hand side of the images is represented by the light red and white color strip. The system is not optically optimized to view the jet flow field, and hence, the jet flow is not visually resolved. At the jet shear layer boundary Mach waves are formed at consistent intervals and propagate away from the main jet flow. Strong directional waves are observed emanating to the far field at a consistent Mach angle.

In figure 4.1a highly directional acoustic waves are present, but interference occurs when waves from random small eddie formations interact with the directional waves. In figure 4.1b

highly directional acoustic waves are shown to propagate outward in a curved fashion at a given angle away from the jet flow field. These Mach waves can be identified by the angle of separation from the main flow known as the Mach angle. The Mach angle from these images was estimated to be 56 degrees separation from the vertical shear layer of the jet. The Mach waves are traveling at the speed of sound which is about 340 m/s. Once the Mach angle of the sound waves is determined the convective Mach speed of the jet flow can be estimated. The convective Mach number is the speed of the turbulent structures formed in the shear layer of the jet flow. The convective Mach speed will be less than the nozzle exit Mach number which was calculated to be 1.85 previously. The convective Mach speed of the jet in these experiments is estimated to be 1.74.

The schlieren images in figure 4.1 were corrupted by significant measurement noise. In this research the measurement noise is defined as the combination of electrical interference, optical uncertainties, and small light fluctuation from the source light that cause the actual acoustic signal to be diminished. The signal to noise ratio was improved by incorporating a new high power solid state plasma light source as described in Chapter 3. To best utilize this light source the de-collimating lens was changed to a 101 mm diameter and 1000 mm focal length lens. The framing rate was increased to 262,500 frames per second (fps) which increased the spatial resolution to 475 microns per pixel. The C-D nozzle was the same as in the previous experiment. The stagnation pressure was maintained at 2,400 kPa (350 psi). A sequence of resulting schlieren images are presented in Figure 4.2 and 4.3. The jet flow field is nearly centered on the right hand side of the images, but the sound probe has been removed from the experimental setup. The field of view of the flow field is such that the outer limits of the circular lens can no longer be seen.

Figure 4.2 shows the sequence of schlieren images for  $Z/D = 0$  to 15. Two distinct wave types exist. First type of wave form originates at random locations in the jet flow and propagates outward in random directions. These waves are most pronounced in the top right corner of the schlieren images. These waves are believed to be generated from the small eddies in the jet shear layer. The second dominant wave type is the directional Mach waves originating in the shear layer of the jet flow between  $Z/D = 3$  to 5 and propagate downstream. Figure 4.3 shows experimental images acquired for  $Z/D = 15$  to 30. In this figure the turbulence breaks down the jet flow structure and dominant directional Mach waves appear to originate at an upstream location. Broadband acoustic emissions from small-scale eddies cannot be observed in these images. These images illustrate that acoustic waves originate upstream of the jet breakdown point.

The directional Mach waves are produced in an intermittent manner. Video images show several waves generated in a repeated manner, followed by a period of no wave generation before another sequence with wave fronts emerges. Figure 4.4 shows schlieren images acquired at random time intervals during an experimental run. These images illustrate the intermittency of the directional Mach waves. Each image shows a different number of grouped wave fronts. This repeatable process produces packets of three to ten wave fronts at one time. These waves are believed to originate from large scale vortical structures in the jet flow as discussed in previous research. The directional Mach waves propagated at 45 degree angle from the jet flow. Thus the convective Mach number associated with large scale structures is estimated as 1.41. This result signifies that the jet flow is indeed supersonic.

Images presented in figures 4.2 and 4.3 are a small sample set of thousands of images acquired in this experiment. While wave interactions are complex, certain trends repeat in a

predictable manner. The wave developing from the large turbulent structures are highly directional with respect to the jet flow direction. These waves are generated in small packets of three to ten wave fronts with a small intermittency window which repeat in a consistent manner. These waves originate in the near field at about  $Z/D = 3$  to  $5$  and dominate the flow up to  $Z/D \approx 20$  where the jet flow structure breaks down. The directional Mach waves propagate at a fixed angle with respect to the jet flow. In contrast, small scale turbulent structures produce lower intensity acoustic waves that propagate from throughout the jet shear layer upstream of the turbulent breakdown point. These waves can however be dominated by the directional waves.

### Hue Statistics

Analysis of schlieren images involves calculation of statistical parameters to gain insight into the acoustic field. For an experimental run, the hue at each pixel location is computed from schlieren images without and with test media. The mean and standard deviation of hue is then computed for each data set. Mean hue of the background image indicates the sensitivity of the rainbow filter. Figure 4.5 shows the mean hue acquired with no test media. It is observed that in the range of  $R/D = 1$  to  $7$  at fixed axial locations the hue variation is relatively linear. For  $R/D > 7$  non-linear fluctuations occur in the background hue at fixed axial locations.

Standard deviation of hue for the background images offers insight into optical aberrations and electronic noise present in the system without the flow field. Figure 4.6 shows a contour plot of the standard deviation of hue using 33,000 background images. In this and subsequent figures the radial axis at  $R/D = 0$  is shown on the left side. Thus the jet flow field is represented on the left hand side of the contour plots. Figure 4.6 shows that the hue variance in the background images is within two degrees in the region where the acoustic flow field would

be present with test media. Higher hue variation of up to four and five degrees occurs in the region coinciding with the jet flow field. The higher hue variation is attributed to the nonlinearities in the rainbow filter. The rainbow filter was positioned to minimize hue variation in the acoustic region of schlieren images with test media, necessary to improve the signal to noise ratio.

It will be shown later that the hue variance with test media is up to an order of magnitude greater than the background hue variance. However, hue variance for  $R/D = 6$  is nearly the same for background and experimental images and hence, these regions would provide poor signal to noise ratio adversely affecting the analysis.

Next, figures 4.7 and 4.8 show mean hue difference contours for experimental images to illustrate the jet flow and acoustic fields. The hue difference is the difference in hue at each pixel location with and without test media. As expected the hue varies greatly within the jet flow field. Large density variation in the jet flow field cause large ray deflections and thus, extensive color shifts as shown in figure 4.7. Large ray deflections in the jet flow region exceed the filter range used in this study, and thus cannot be quantified for analysis. In figure 4.8, a larger hue difference occurs in the jet shear layer region where density gradients are the largest. Farther downstream the jet flow breaks down by turbulence, which decreases density gradients and hence the hue difference gradients. Figures 4.9 and 4.10 show the same data but with a different scale for hue difference to highlight the acoustic regime. In the acoustic regime beyond  $R/D > 6$  the hue difference is nearly zero. Thus the hue difference between background and experimental data is within the noise floor. Thus, like concluded previously, the experimental noise for  $R/D > 6.0$  is too large for accurate analysis.

Figures 4.11 and 4.12 show the standard deviation (STD) of the hue difference with test media. As expected, the STD of hue difference is highest in the jet flow field. High STD signifies large turbulent fluctuations in the flow field which generate the acoustic field. Figures 4.13 and 4.14 show the same data but with a finer scale to illustrate the acoustic regime. The figures show significant STD of hue difference in the acoustic field region until about  $R/D = 6$ . Outside this range, significant noise seems to corrupt the measurements.

Veltin et al [<sup>20</sup>] OD signal along the lipline of a fully expanded jet of Mach number equal to 1.75 are presented in figure 4.15. An initial comparison of hue difference root mean square (RMS) in figure 4.16 and 4.17 can be made with RMS of the OD signal measured by Veltin. The RMS signal increases along the lipline direction to  $Z/D = 8$ . Then the RMS signal decreases in the downstream direction. This trend is also observable in the hue difference RMS presented in figures 4.16 and 4.17 along the lipline ( $R/D = 2$ ) of the jet. Correspondingly, the RMS hue difference also increases steadily along the lipline of the jet. The RMS hue difference reaches a maximum at approximately  $Z/D = 22$  along the lipline. The RMS hue difference then decreases at a similar rate to the result presented in figure 4.15. The axial location for the peak hue difference variance depends upon the jet exit Mach number which is expected to be higher for the present study.

The mean and STD of hue difference reveal basic features of the jet flow field. The above results are used to indicate areas in the field of view where quantitative analysis can be performed. For  $R/D > 6.0$ , the signal to noise ratio is too poor for quantitative analysis. The hue difference RMS is obtained by the UHS-RSD technique and is also consistent with RMS of the OD signals acquired by Veltin et al [<sup>20</sup>].

## FFT Analysis

The frequency content of the acoustic signal offers insight into the acoustic wave characteristics at a specific location. Thus, fast Fourier transform (FFT) analysis of hue difference was performed at various locations throughout the flow field.

Figure 4.18 shows power spectra of the OD signal at different radial locations for fixed  $Z/D = 5.5$  presented by Veltin [<sup>20</sup>]. Veltin presented data for  $R/D$  from 0.48 to 2.5 because the noise floor was reached for  $R/D > 2.5$ . In contrast UHS-RSD technique allows measurements between  $R/D$  of 2 and 6. The overlapping radial direction between  $R/D$  2 to 3 shows a strong correlation with Veltin's power spectra when compared to the power spectra presented in figure 4.33. There is a high frequency peak that is present in both plots located at  $Z/d = 5.5$  and  $R/D = 2.5$ .

Figures 4.19 to 4.45 show the frequency spectra of hue difference for various locations in the field of view. In each of the figures 4.19 to 4.30 the axial location ( $Z/D$ ) is fixed while the radial location is varied between  $R/D = 2$  to 6. Figures 4.19 to 4.25 show frequency spectra for the field of view of  $Z/D = 0$  to 12.5. Figure 4.19 shows the frequency spectra at the nozzle exit i.e.  $Z/D = 0$ . Results show nearly flat spectra indicating weak acoustic signal at the jet exit. Figure 4.20 for  $Z/D = 2.5$  shows a gradual increase in the spectral power for frequencies around 50,000 Hz. High acoustic power is observed within a narrow frequency band. The spectral power is shown to decrease in the radial direction. This result is consistent with previous literature documenting similar decrease in acoustic power. (Veltin 2011) Figures 4.21, 4.22, and 4.23 shows a gradual increase in the power spectra centered around 50,000 Hz with increasing axial distance. In figure 4.24 for  $Z/D = 12.5$  the 50,000 Hz frequencies dominate for  $R/D = 3$  to 5. At  $R/D = 2$  the spectra levels out and it is believed that this location corresponds with the jet flow

shear layer as the flow expands outward in the radial direction farther downstream. In figure 4.25 for  $Z/D = 15.0$  the spectral power at 50,000 Hz range is highest for  $R/D = 6$ . Figures 4.26 to 4.30 show the spectra for the field of view of  $Z/D = 15$  to 27.5. In each successive figure the jet flow interactions reduce the occurrence of high frequency peak power in the signal. High frequency peaks are no longer observed except for  $R/D = 6$  as shown in figure 4.30.

Figures 4.31 to 4.38 show frequency spectra for different axial locations in a plot for a fixed radial coordinate in the field of view of  $Z/D = 0$  to 15. Results show a steady increase in the spectral power of hue difference in the axial direction. However, the signal is diminished at  $R/D = 6$ . This result shows that the noise floor has been reached. These results are consistent with previous studies by Veltin (2011) as explained later.

Figure 4.39 to 4.45 show frequency spectra for different axial locations in a plot for a fixed radial coordinate for the field of view of  $Z/D = 15$  to 27.5. In the shear layer of the jet at  $R/D = 3$  the spectra are nearly the same for all axial locations presented in figure 4.39. Each successive figure shows a decrease in the spectra power for downstream locations. The signal power is reduced to a minimum at  $R/D = 6$  as shown in figure 4.45.

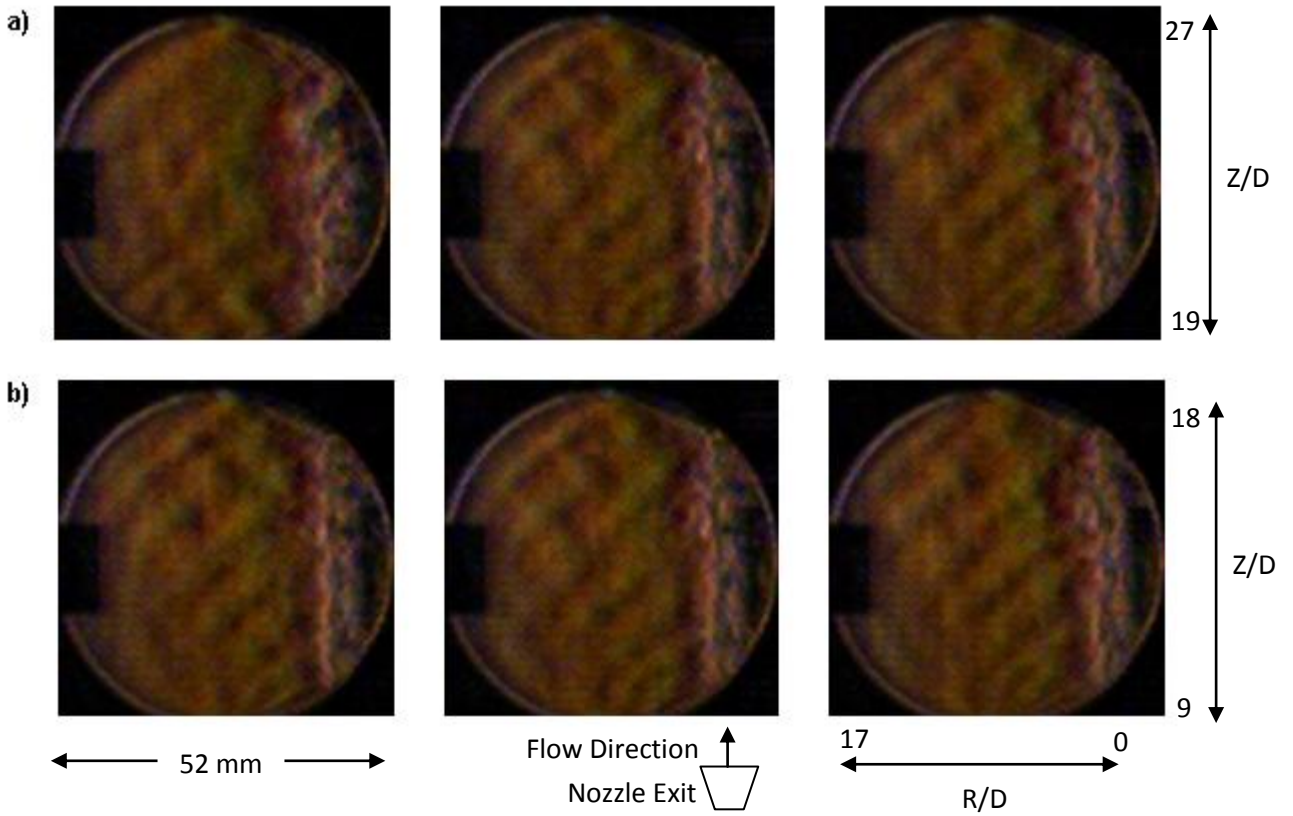


Figure 4.1 Actual image captures from the UHS-RSD technique. From left to right is single frame progression equal to 5 microseconds a)  $Z/D$  between 19 and 27, more interference from small scale turbulent structures propagating upstream and downstream. b)  $Z/D$  between 9 and 18, dominate wave in downstream direction from large scale turbulent structures.

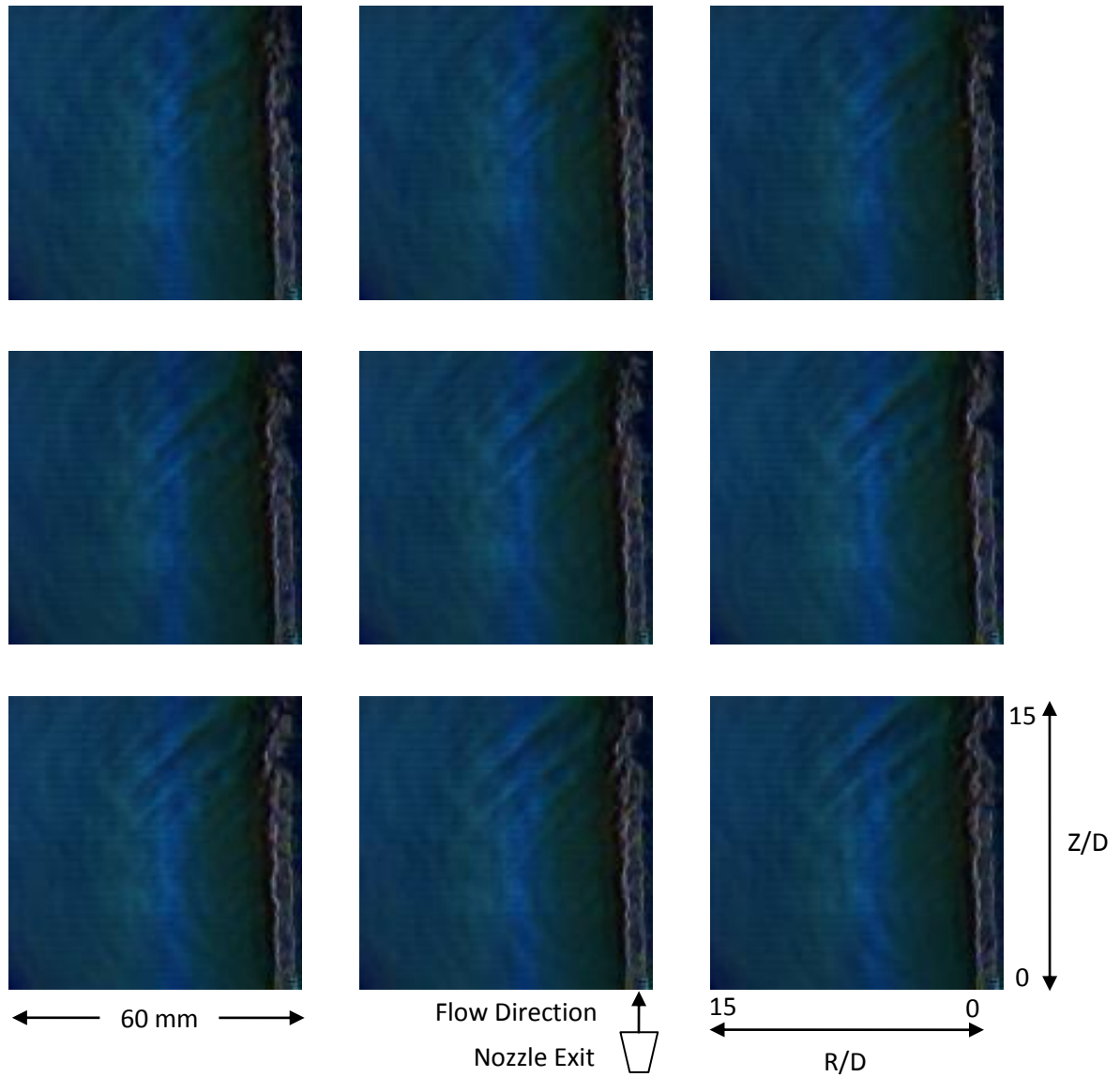


Figure 4.2 Actual schlieren image captures from the UHS-RSD technique. from left to right is single frame progression equal to 3.8 microseconds.  $Z/D$  between 0 and 15, dominate wave in positive direction from large scale turbulent structures.

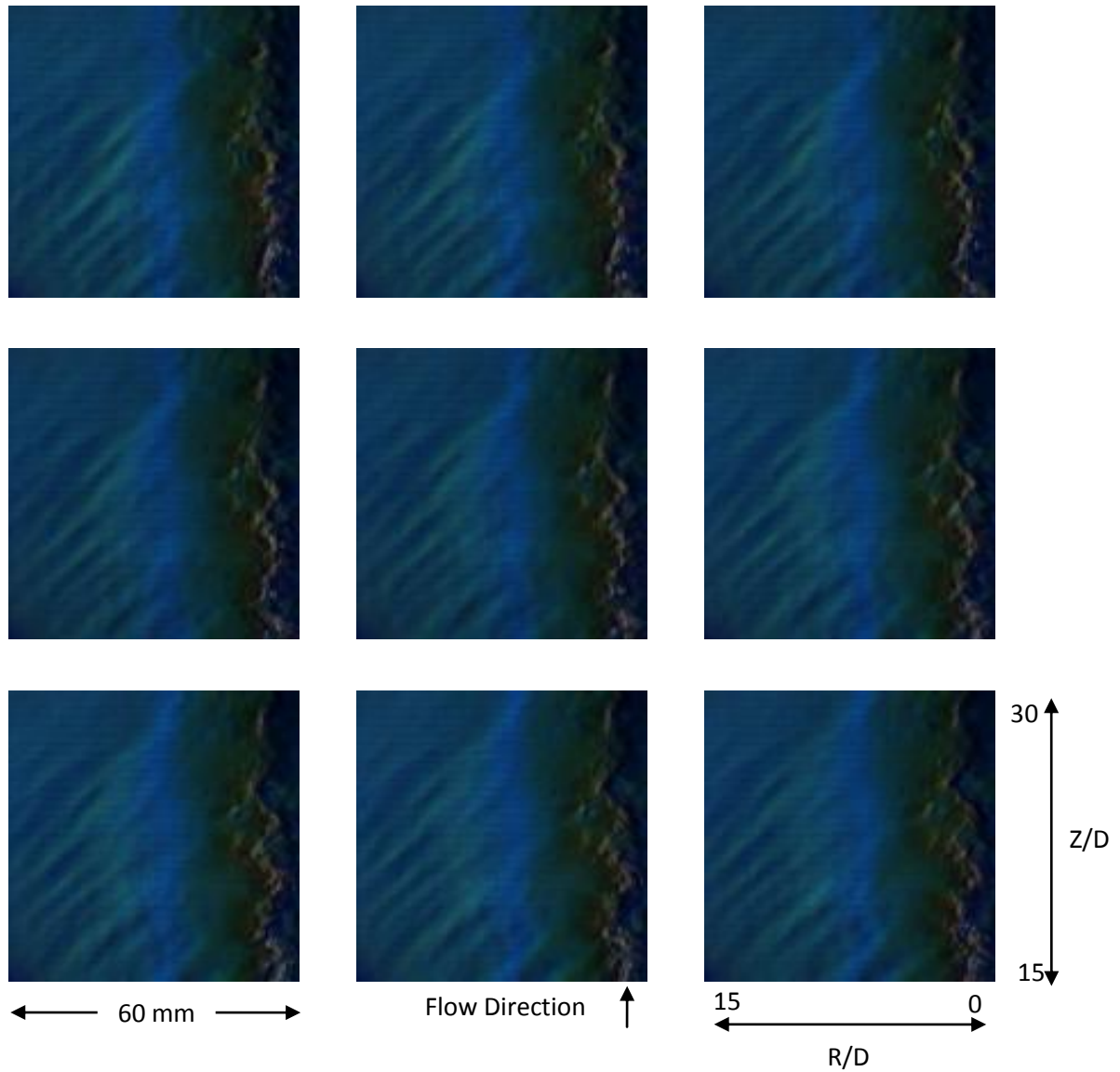


Figure 4.3 Actual image captures from the UHS-RSD technique. from left to right is single frame progression equal to 3.8 microseconds.  $Z/D$  between 15 and 30, dominate wave in positive direction from large scale turbulent structures.

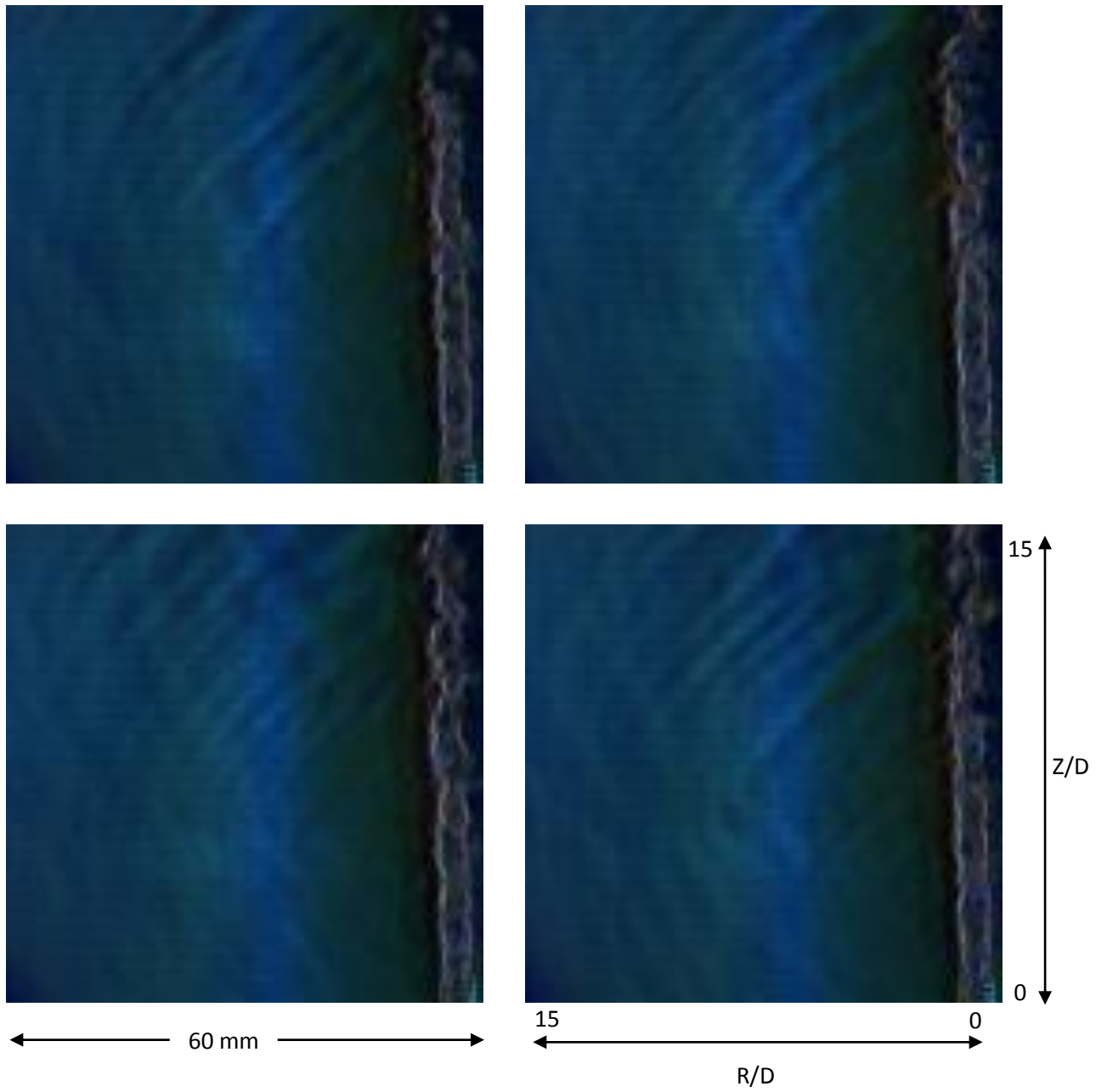


Figure 4.4 Schlieren images acquired at various random time steps used to illustrate intermittency.

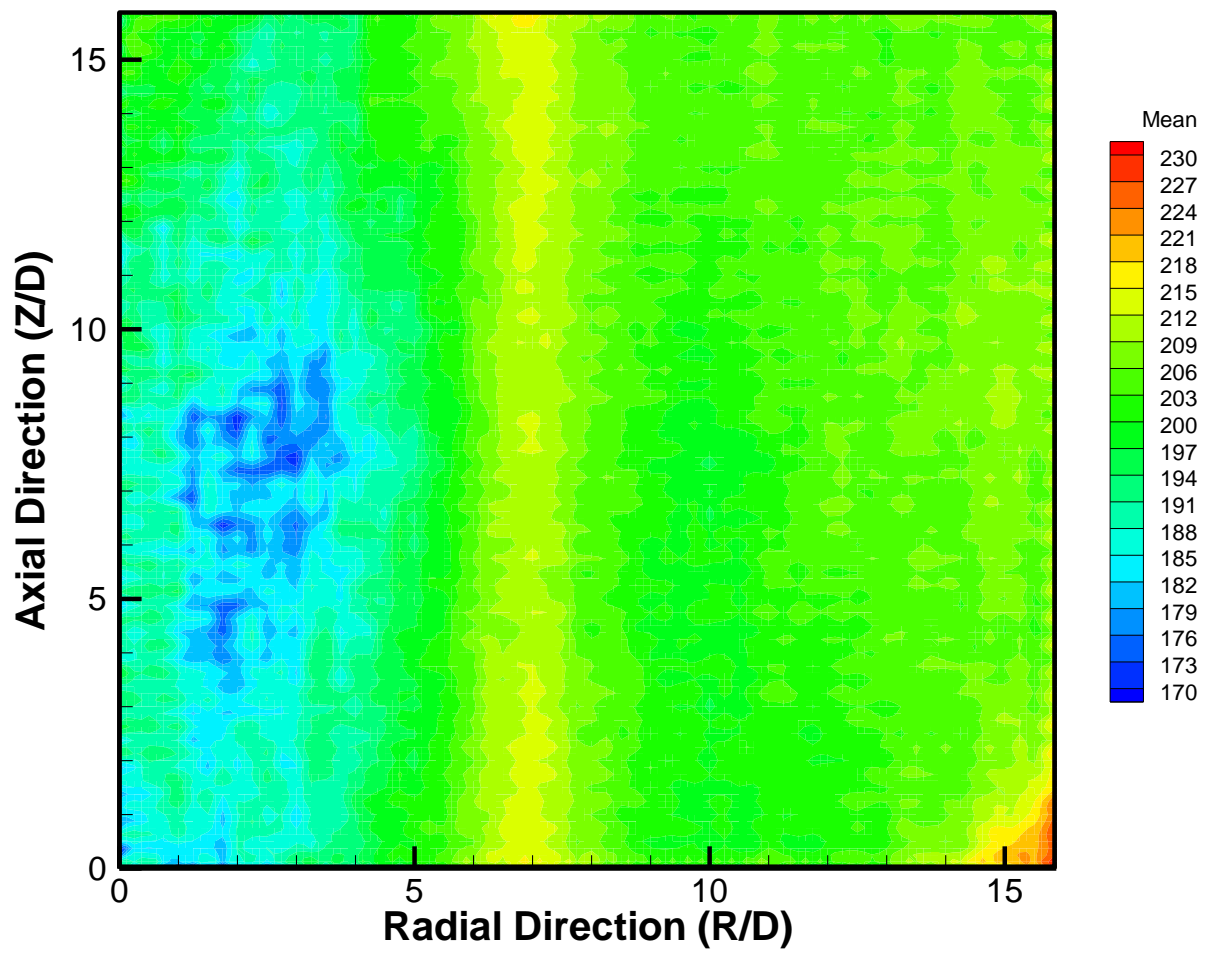


Figure 4.5 Mean Hue of background images. Images captured with no flow to help determine uniformity of background image.

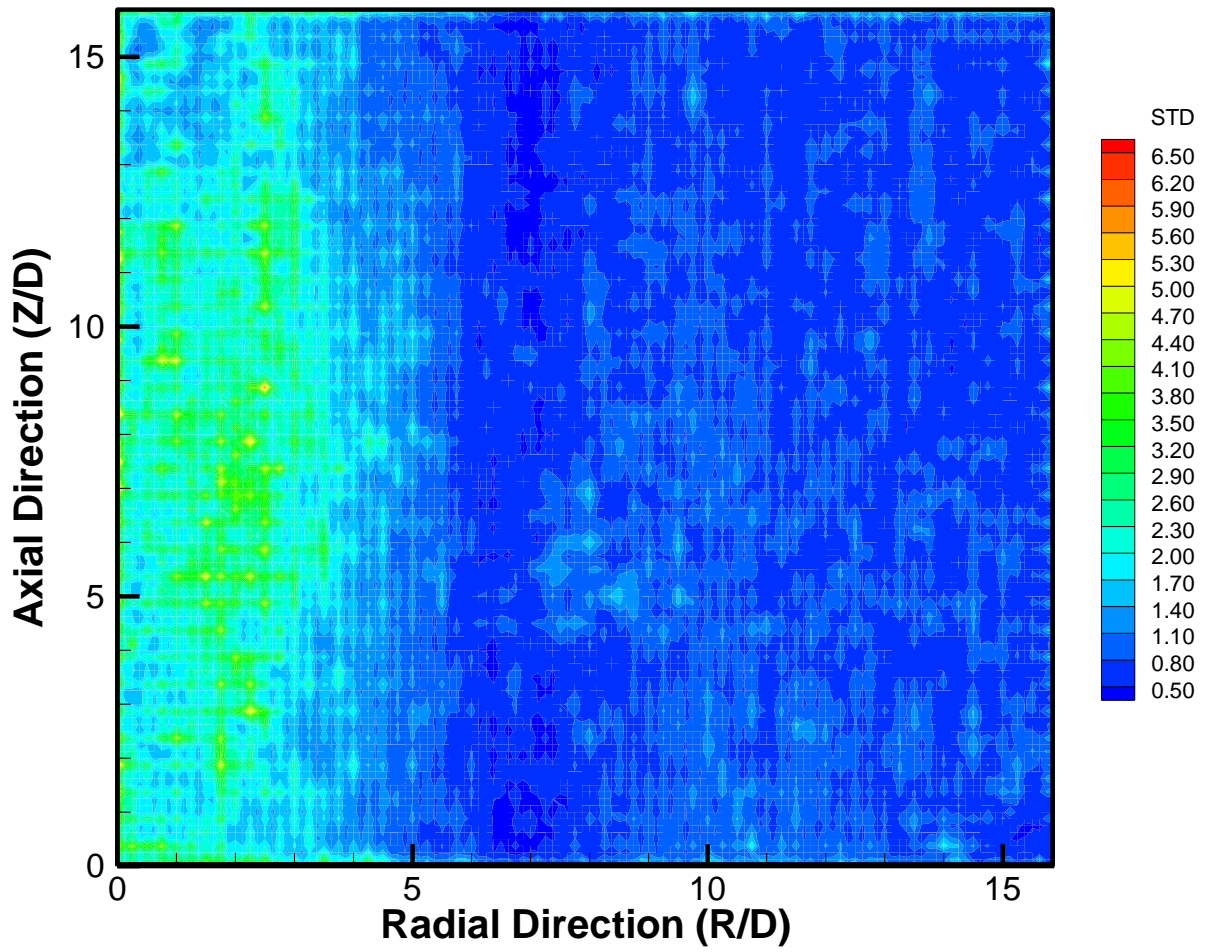


Figure 4.6 Standard deviation from the mean hue of background images. Images captured with no flow to help determine relative background noise.

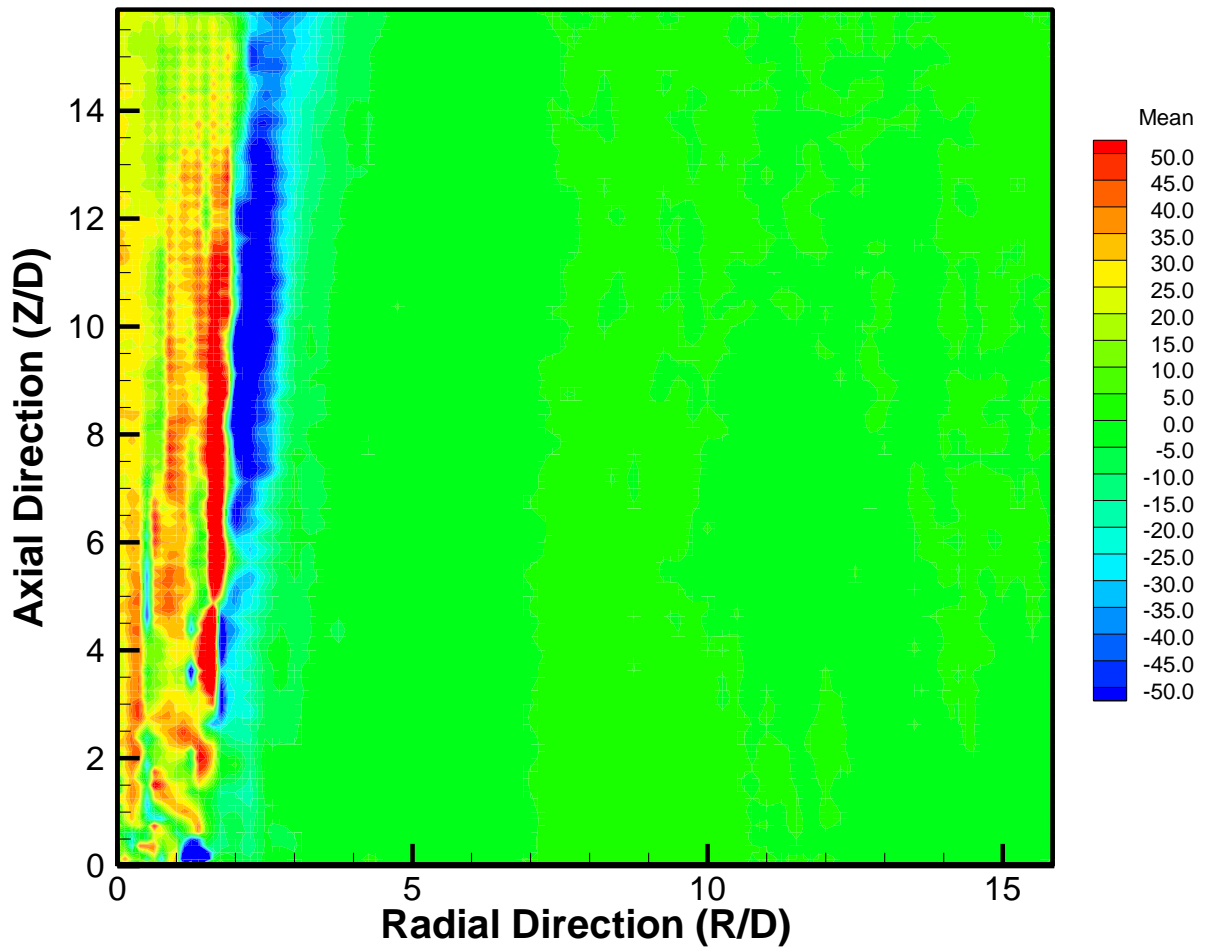


Figure 4.7 Mean hue difference over the total field of view at Z/D direction from 0 to 15. Course hue difference range spans 100 degrees hue

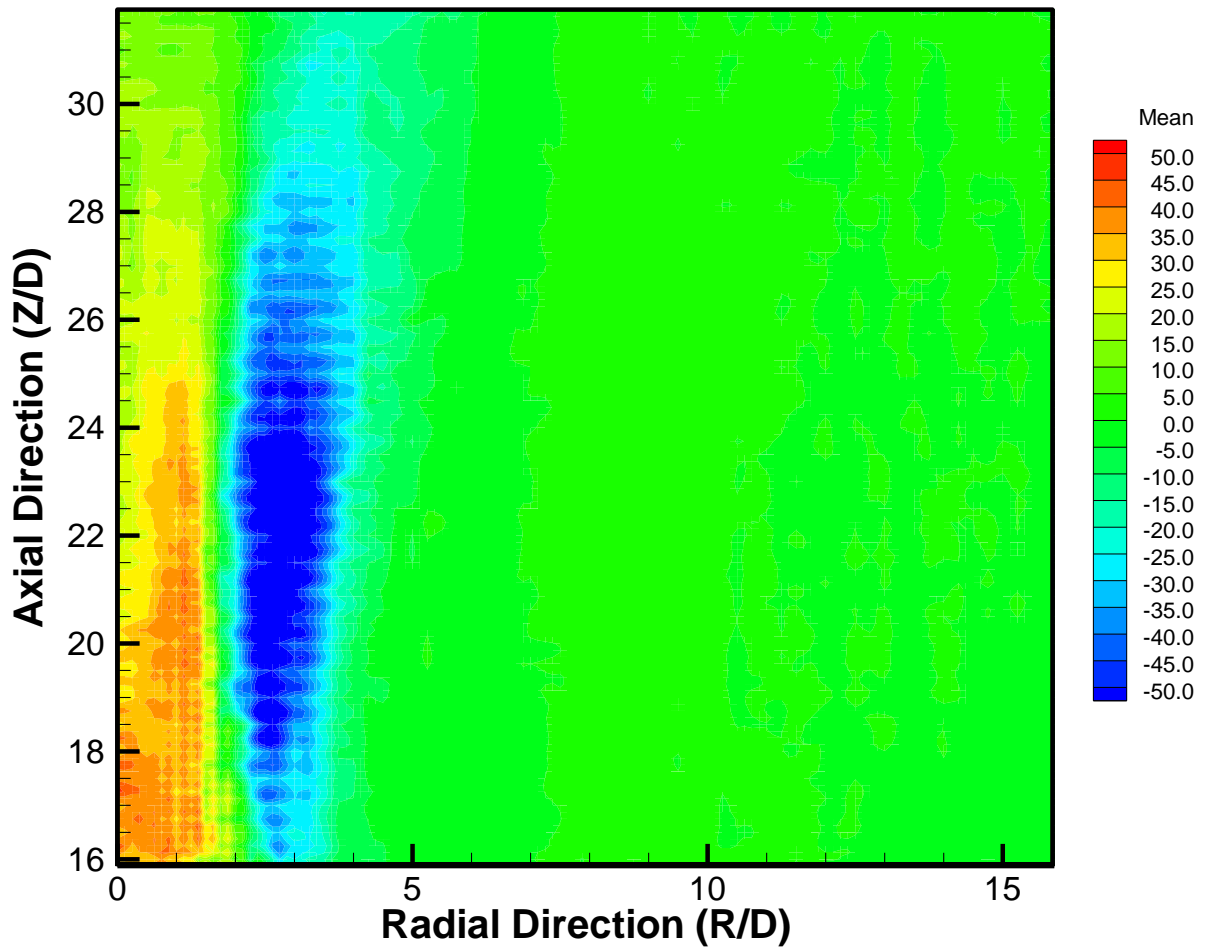


Figure 4.8 Mean hue difference over the total field of view at Z/D direction from 15 to 30.

Course hue difference range spans 100 degrees hue

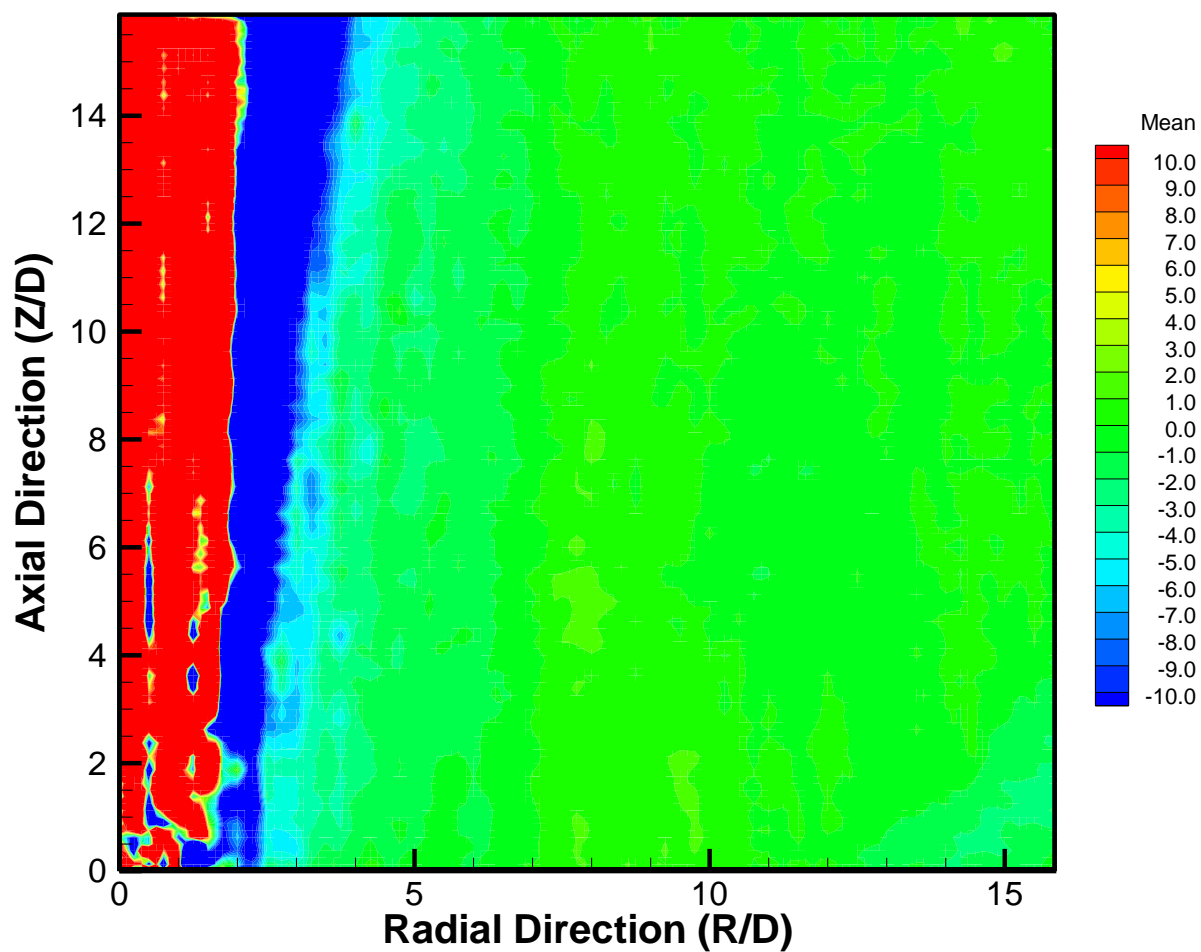


Figure 4.9 Mean hue difference over the total field of view at Z/D direction from 0 to 15. Fine hue difference range spans 20 degrees hue to see hue difference variation in acoustic regime

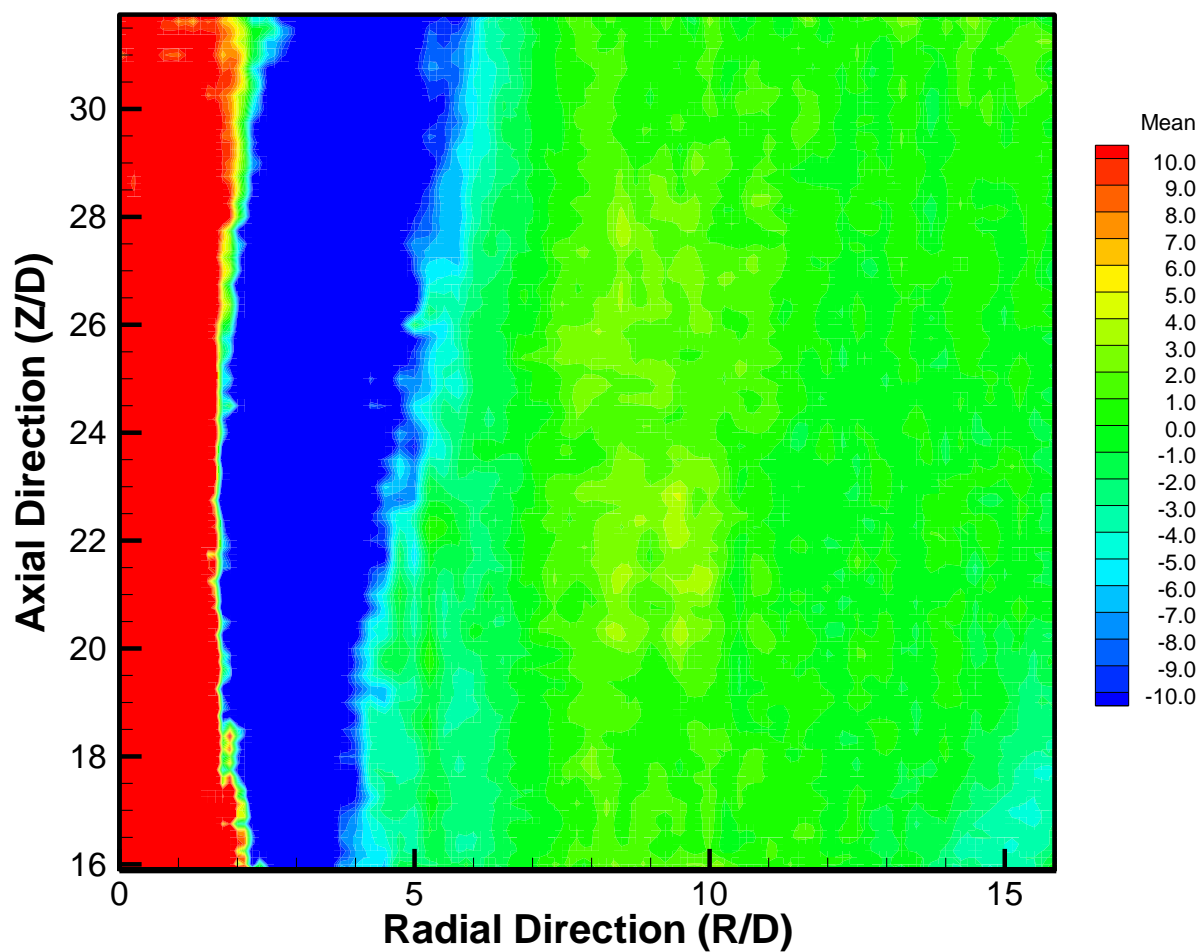


Figure 4.10 Mean hue difference over the total field of view at Z/D direction from 15 to 30. Fine hue difference range spans 20 degrees hue to see hue difference variation in acoustic regime

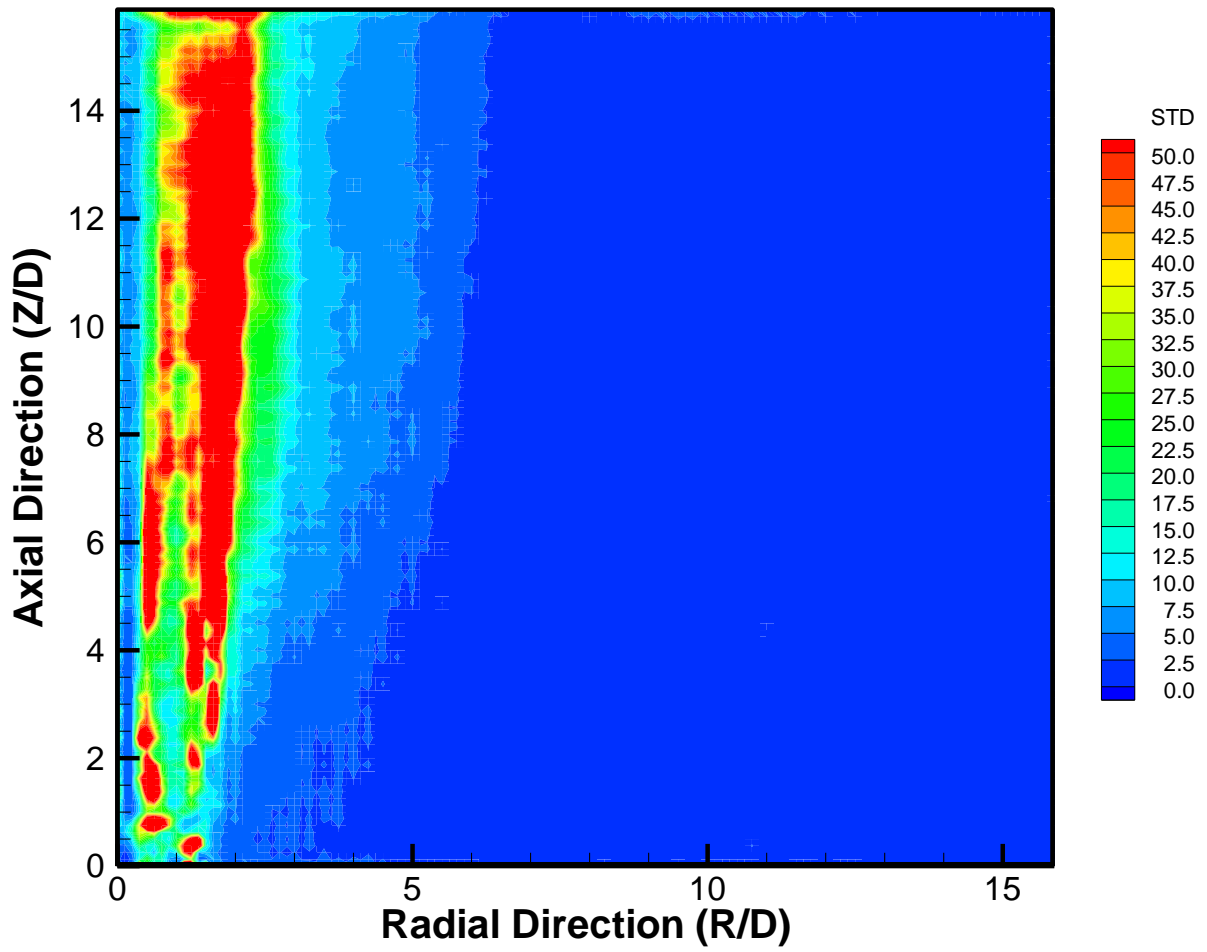


Figure 4.11 Standard deviation from mean hue difference over the total field from  $Z/D = 0$  to 15.

Course degree deviation range spans 50 degrees

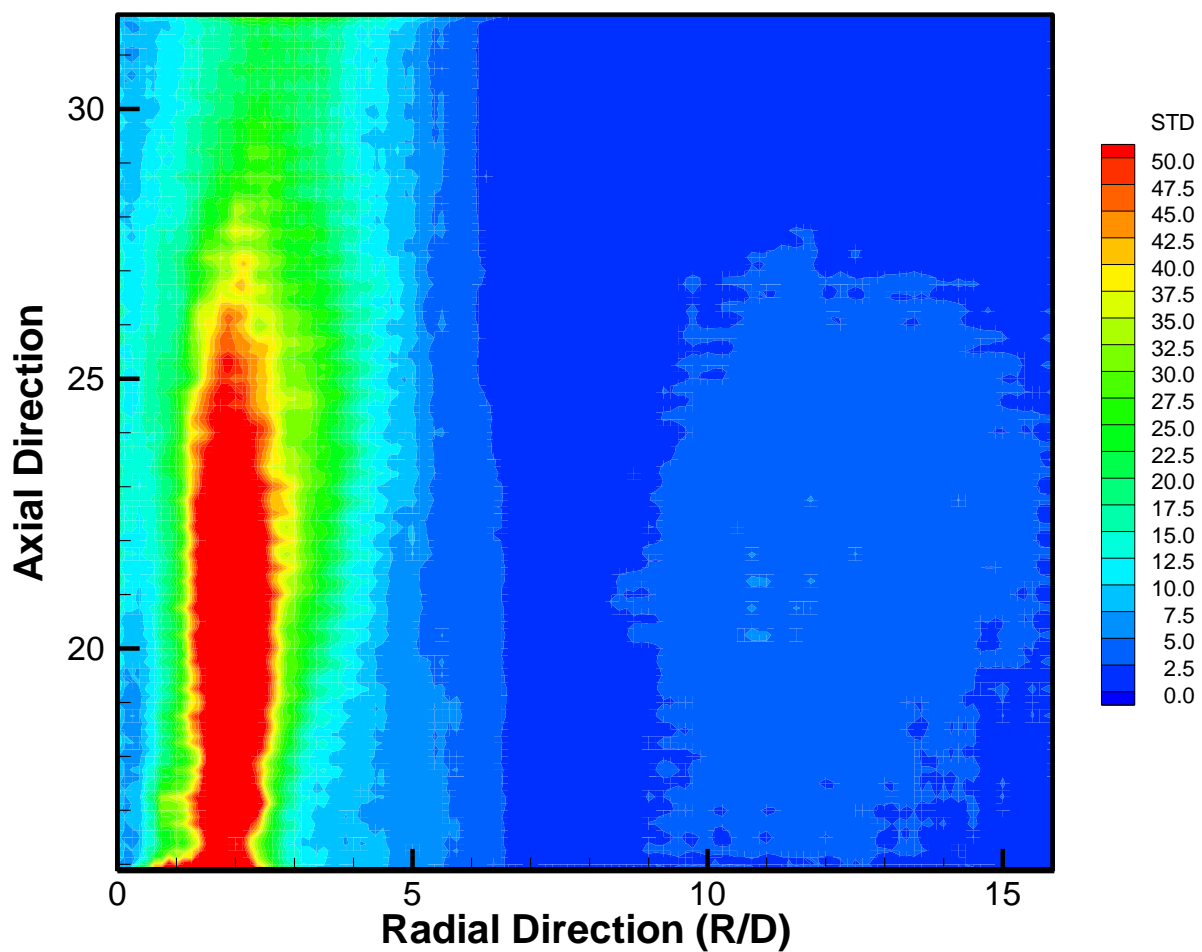


Figure 4.12 Standard deviation from mean hue difference over the total field from  $Z/D = 15$  to 30. Course degree deviation range spans 50 degrees

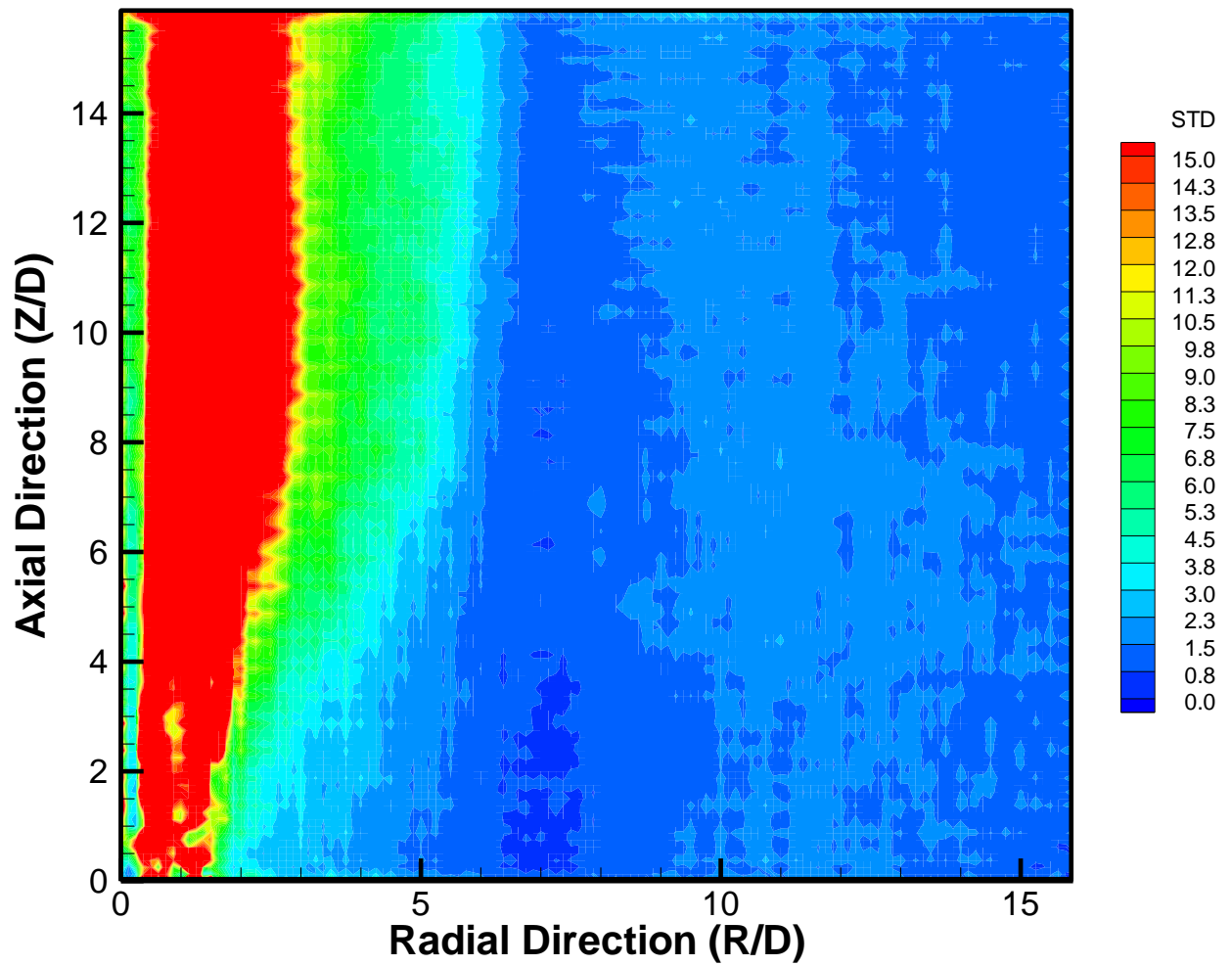


Figure 4.13 Standard deviation from mean hue difference over the total field from  $Z/D = 0$  to 15.

Fine degree deviation range spans 15 degrees.

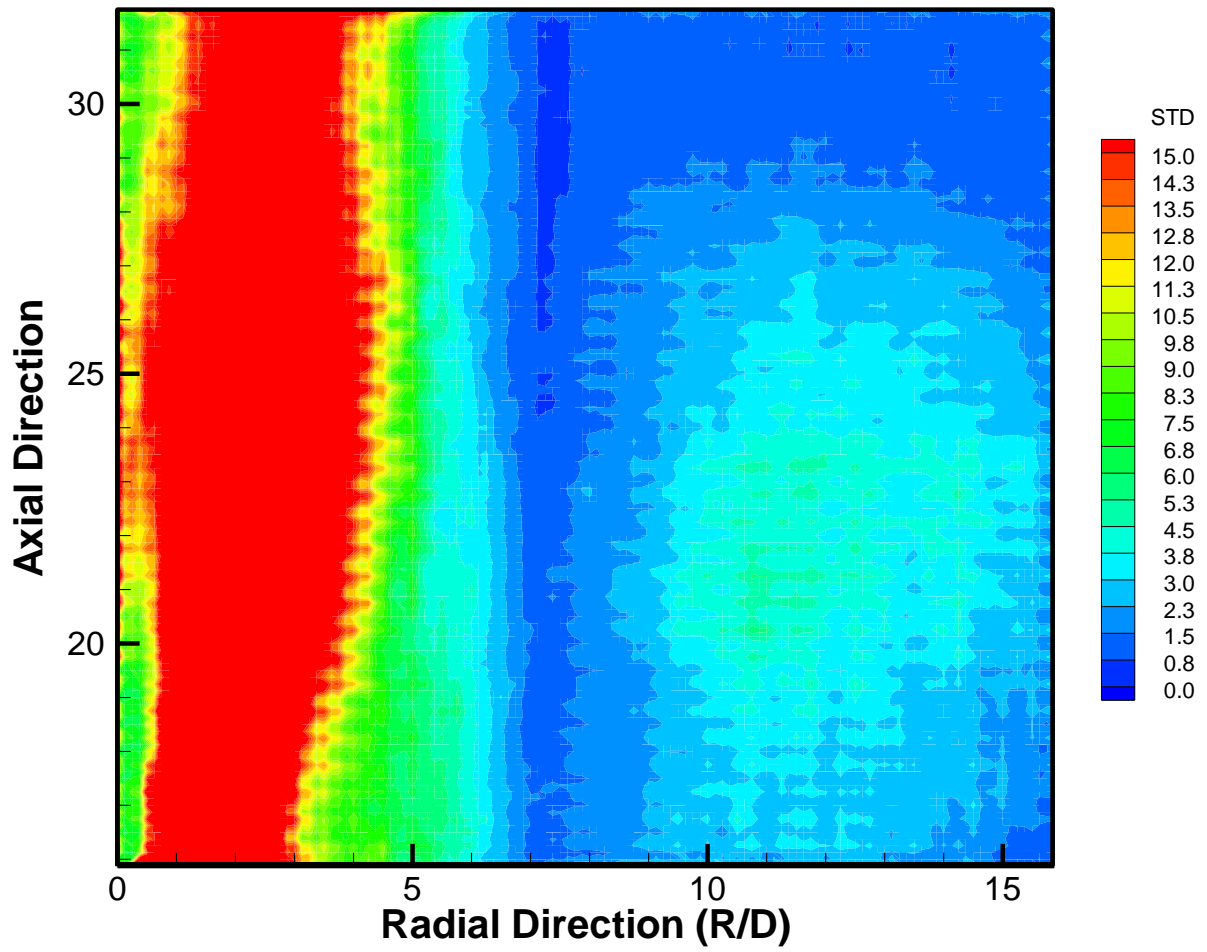


Figure 4.14 Standard deviation from mean hue difference over the total field from  $Z/D = 15$  to 30. Fine degree deviation range spans 15 degrees.

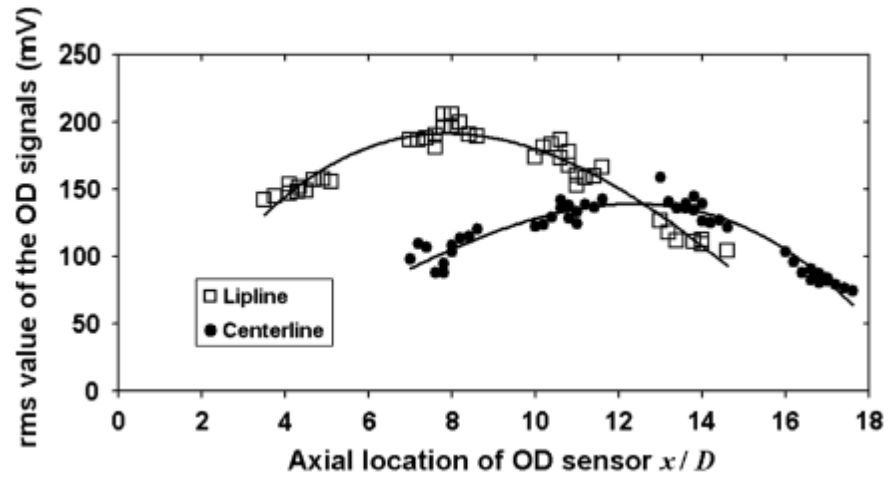


Figure 4.15 RMS values of the OD signals along the axial direction in a fully expanded,  $M_j = 1.75$  jet presented in Veltin (2011).

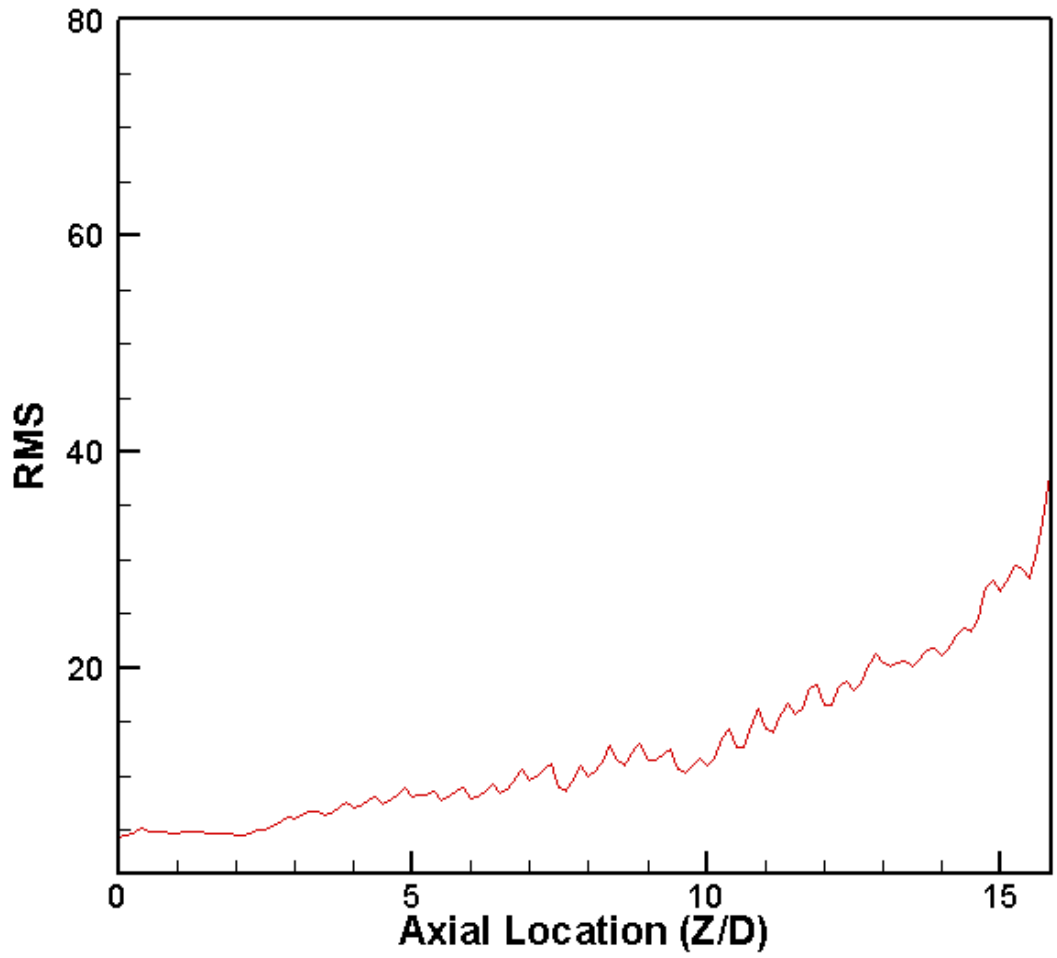


Figure 4.16 Hue difference RMS values of UHS-RSD along the lipline ( $R/D = 2$ ) for the axial locations of  $Z/D = 0$  to 15.

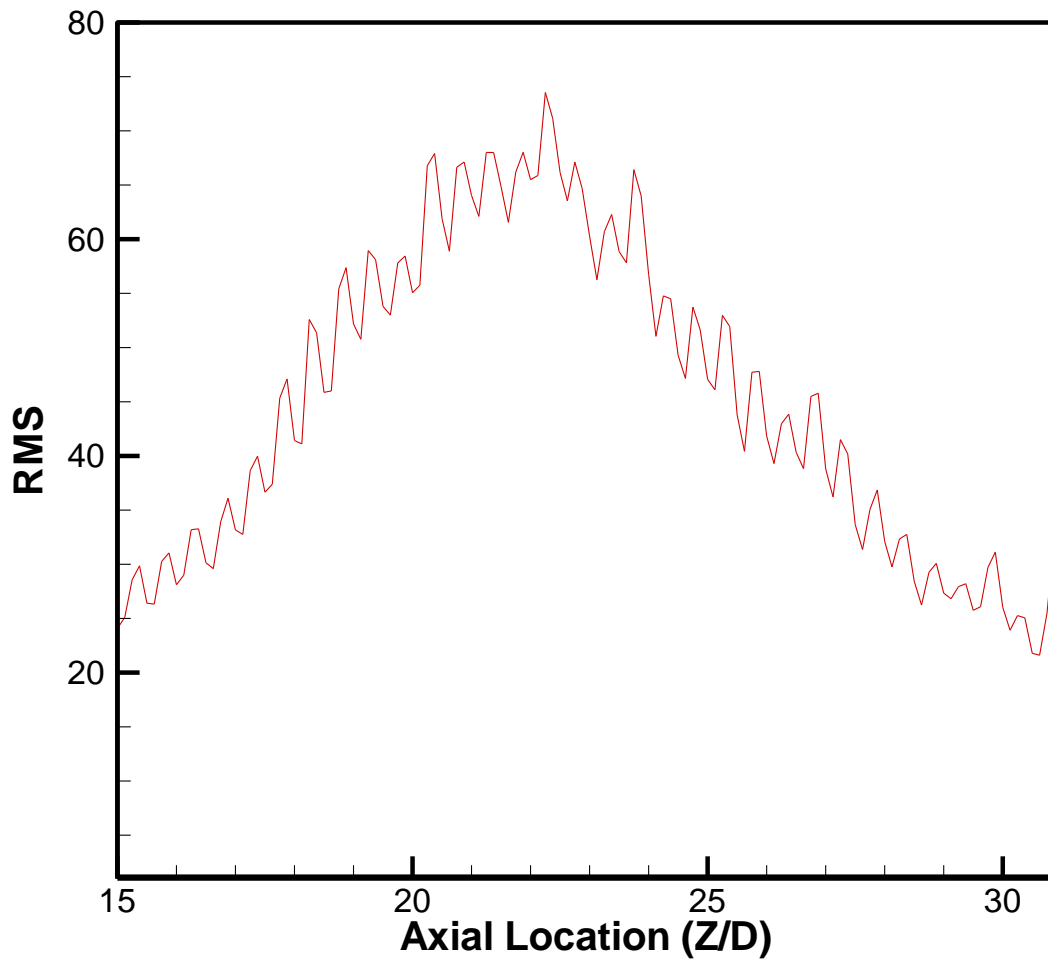


Figure 4.17 Hue difference RMS values of UHS-RSD along the lipline ( $R/D = 2$ ) for the axial locations of  $Z/D = 15$  to  $30$ .

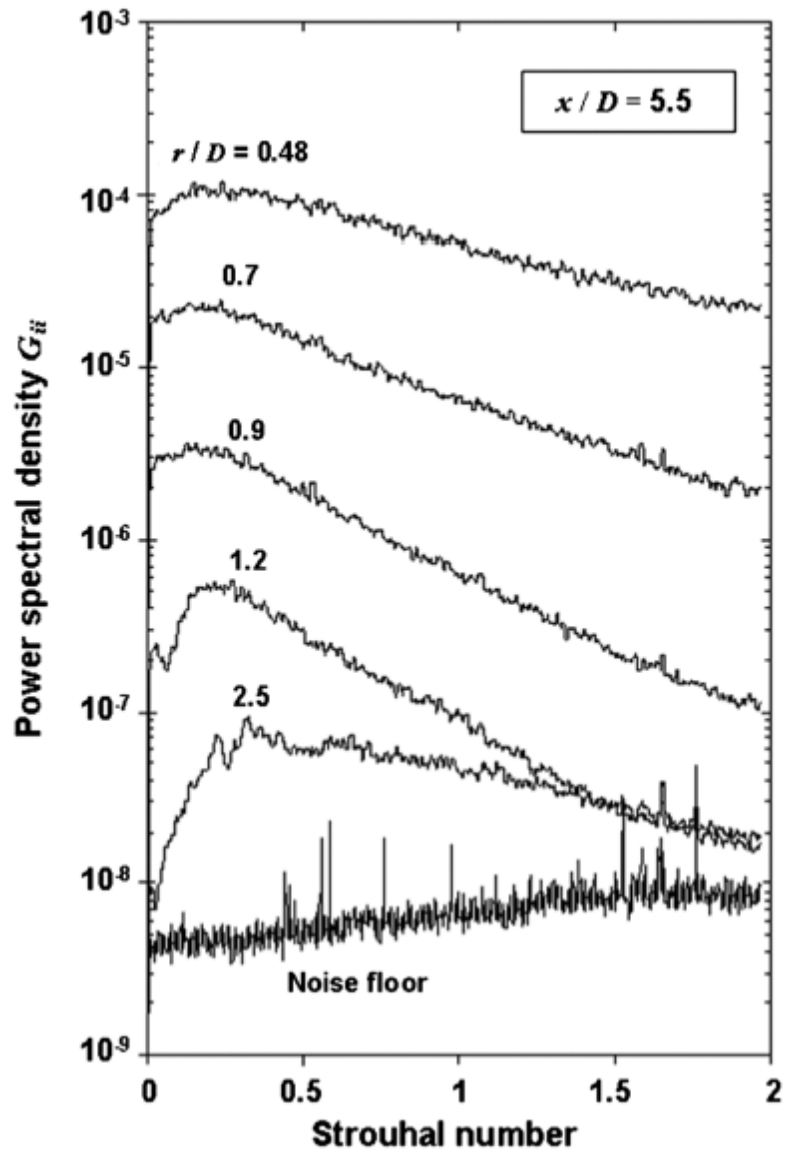


Figure 4.18  $M = 1.75$  jet power spectral density measured at different radial location and at  $x/D$  ( $Z/D$ ) = 5.5 presented by Veltin (2011)

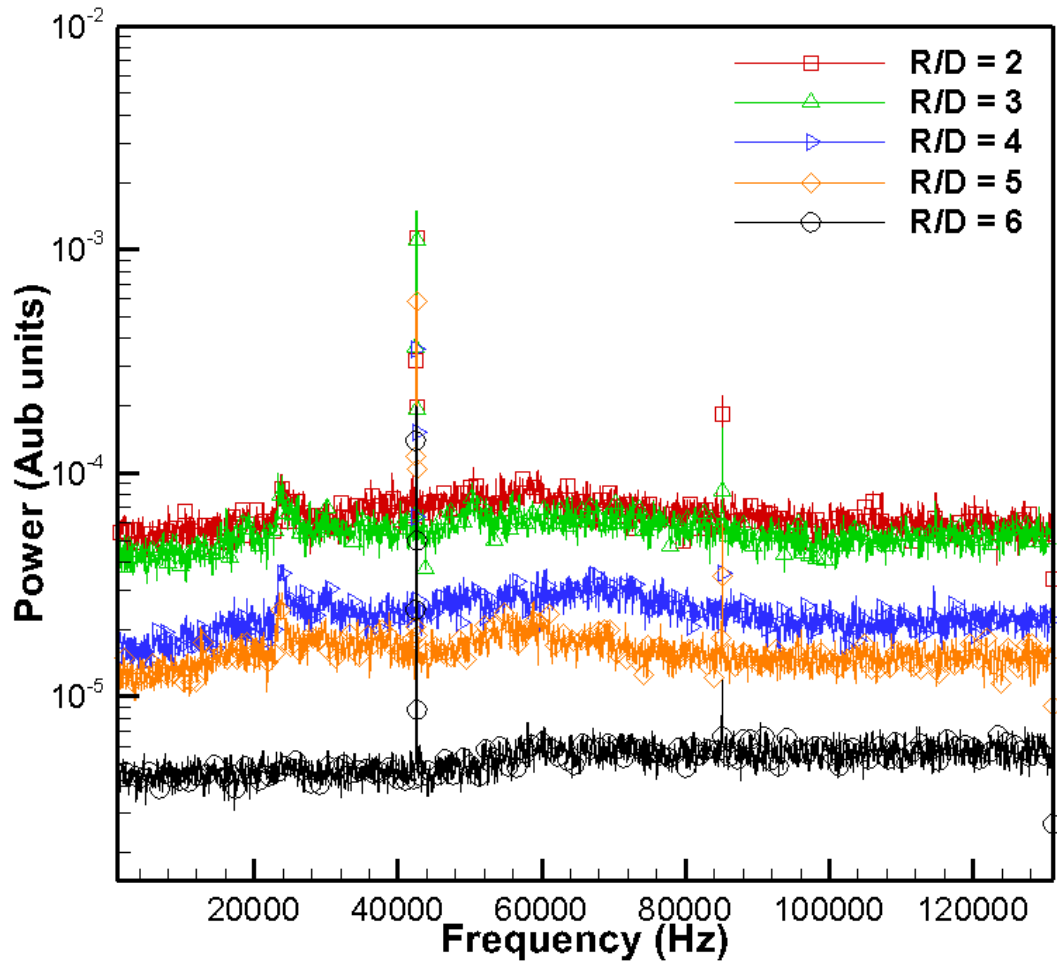


Figure 4.19 Frequency spectrum at  $Z/D = 0$

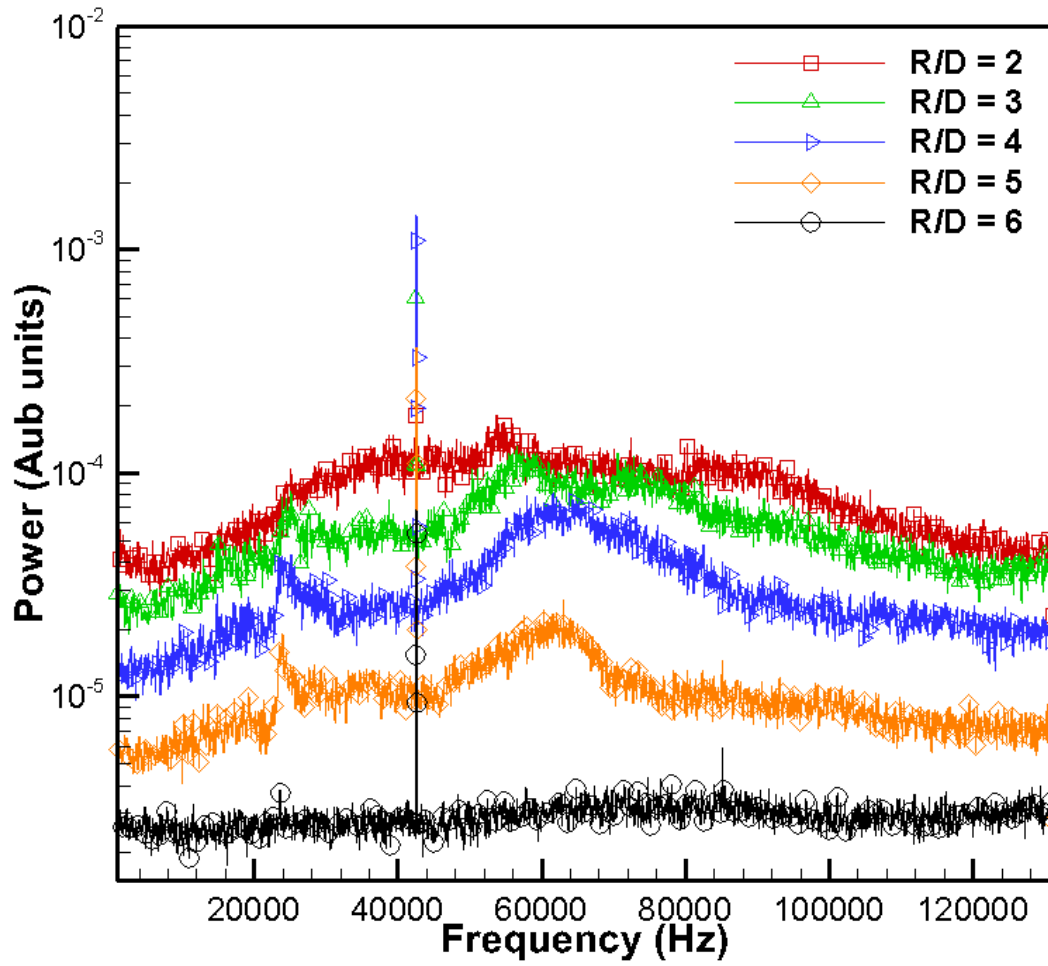


Figure 4.20 Frequency spectrum at  $Z/D = 2.5$

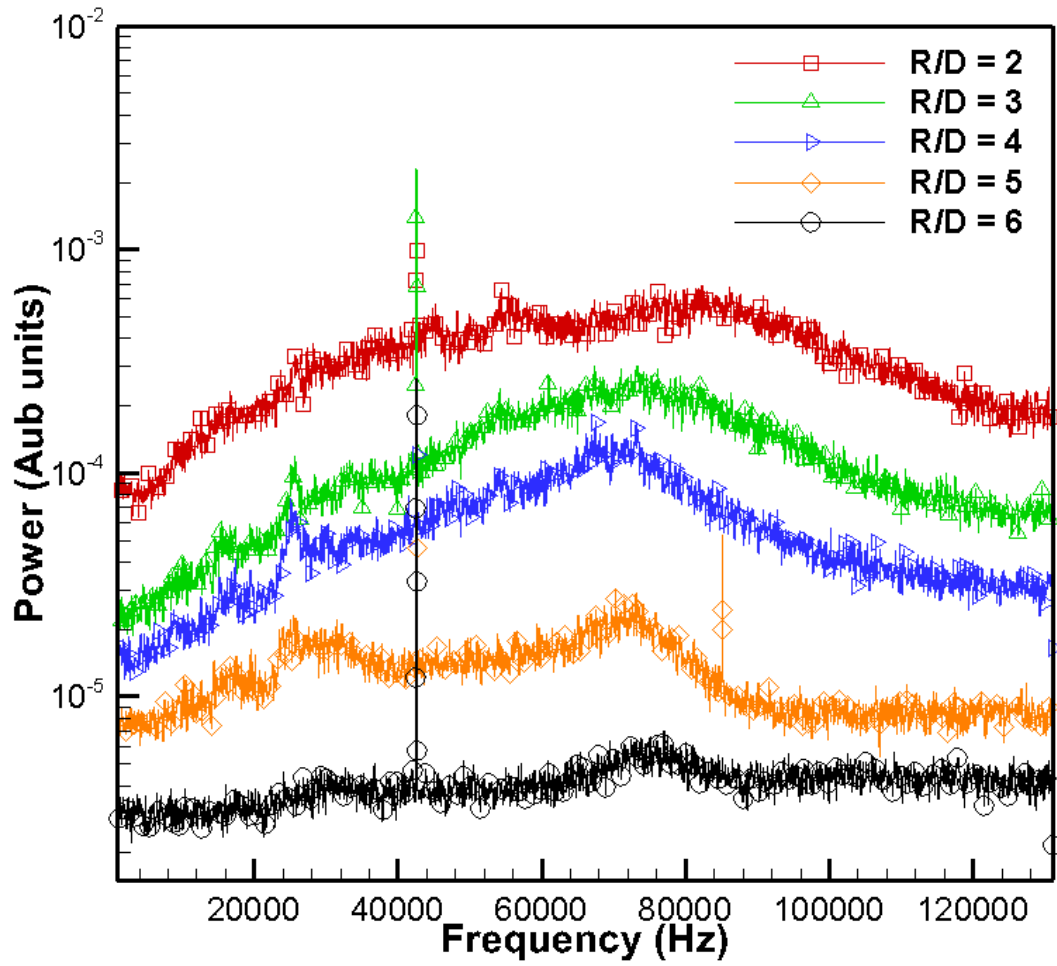


Figure 4.21 Frequency spectrum at  $Z/D = 5$

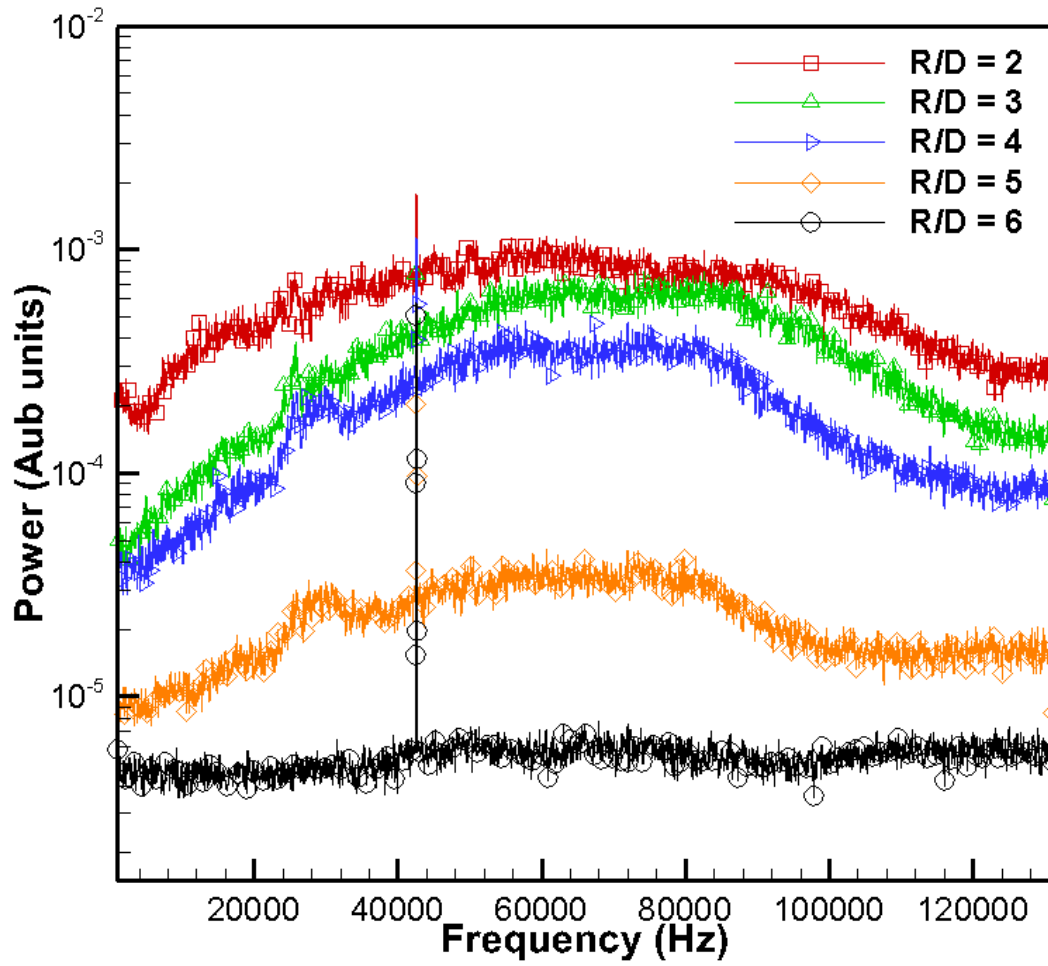


Figure 4.22 Frequency spectrum at  $Z/D = 7.5$

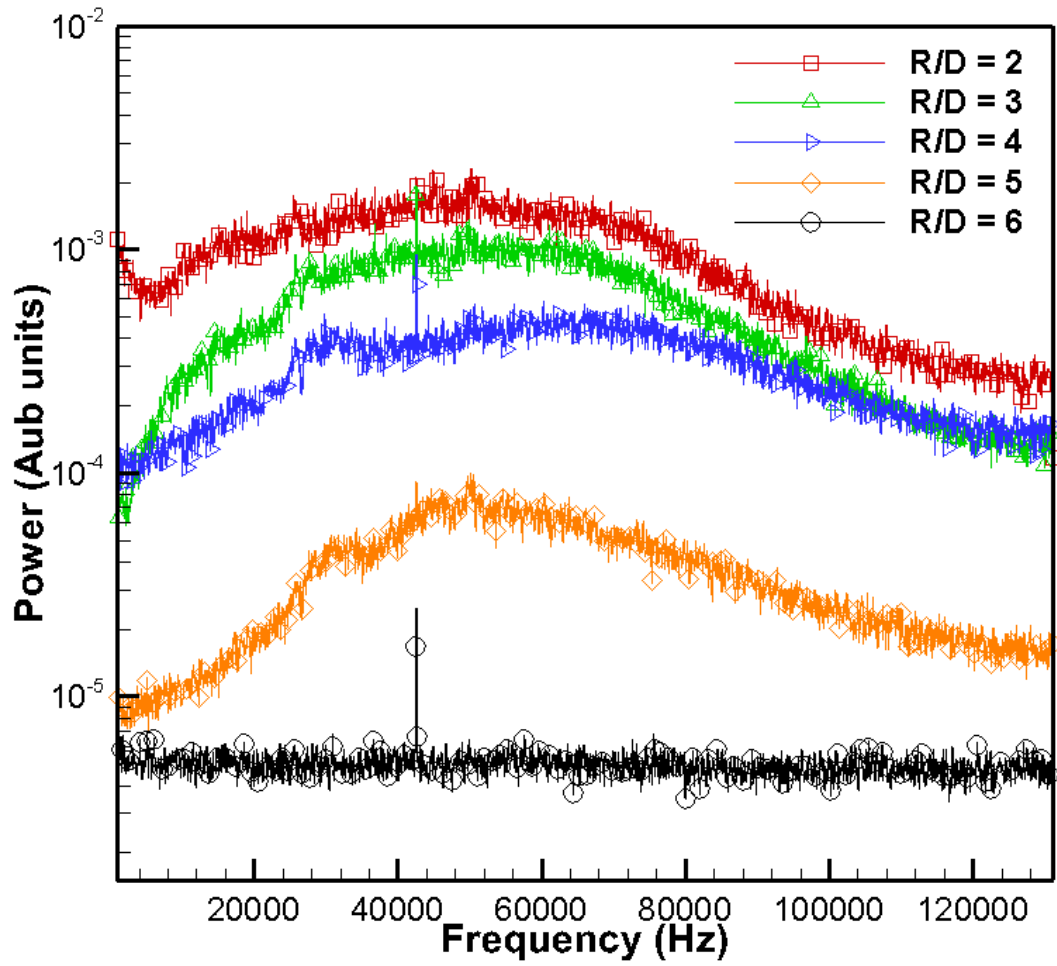


Figure 4.23 Frequency spectrum at  $Z/D = 10$

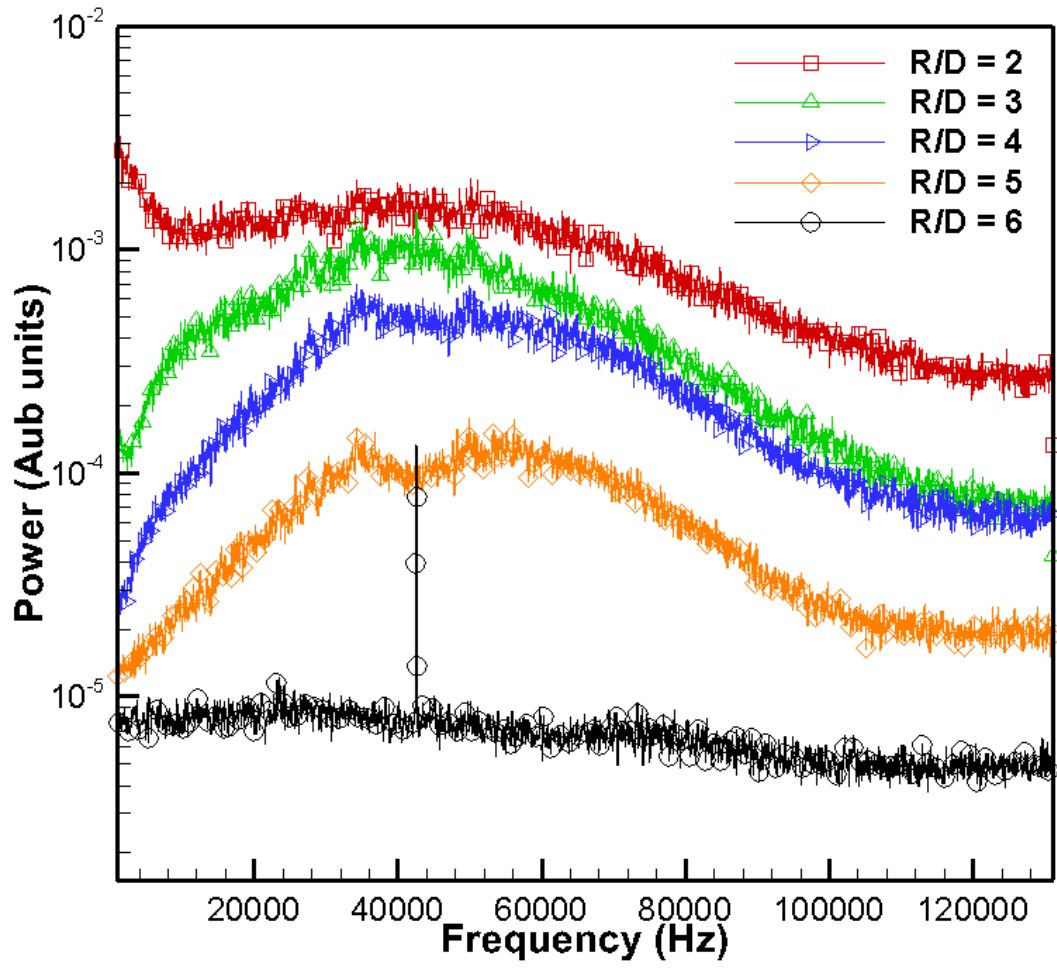


Figure 4.24 Frequency spectrum at  $Z/D = 12.5$

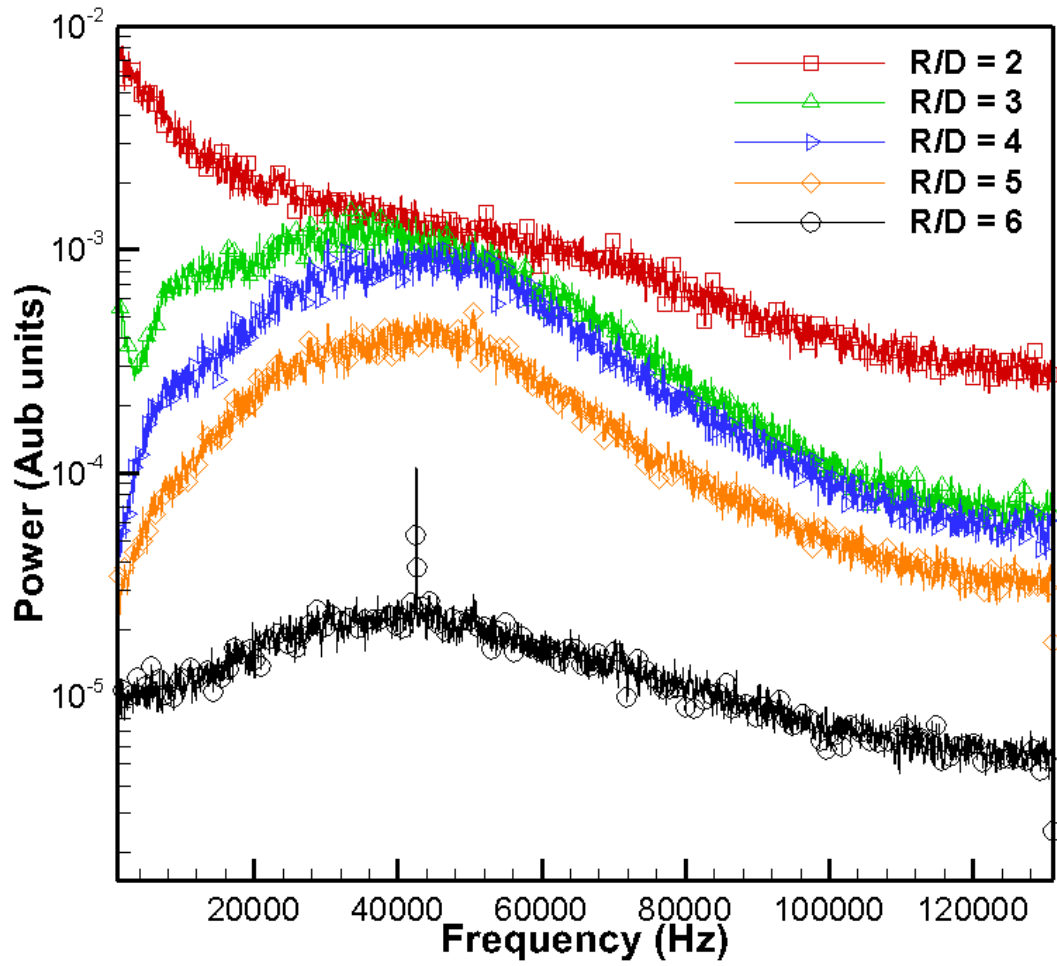


Figure 4.25 Frequency spectrum at  $Z/D = 15$

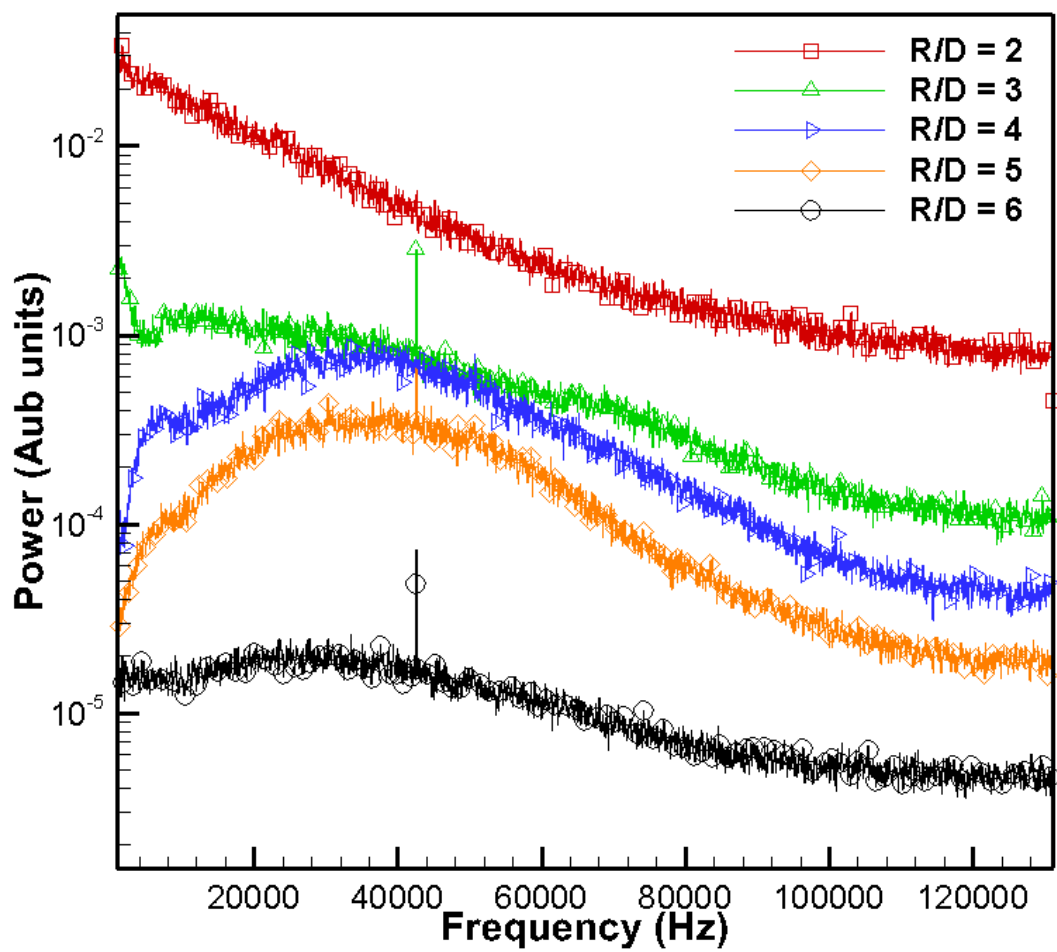


Figure 4.26 Frequency spectrum at  $Z/D = 17.5$

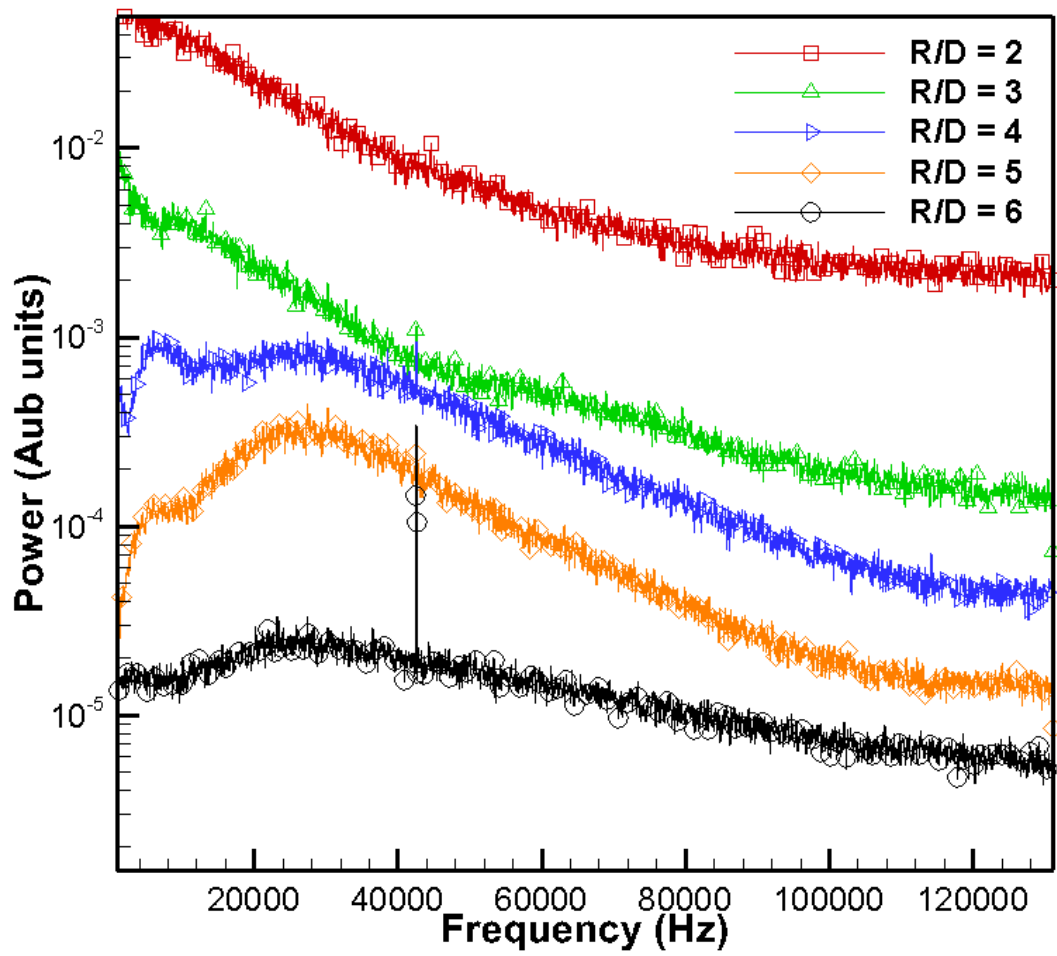


Figure 4.27 Frequency spectrum at  $Z/D = 20$

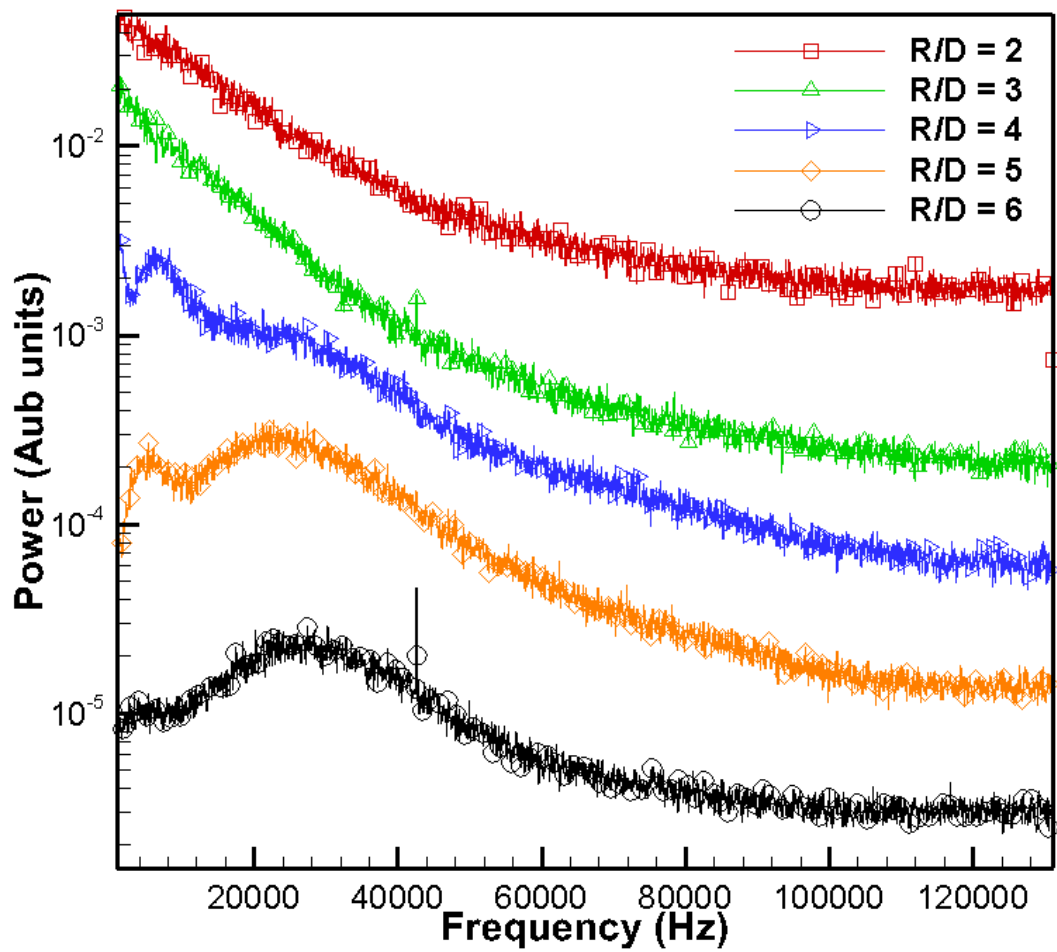


Figure 4.28 Frequency spectrum at  $Z/D = 22.5$

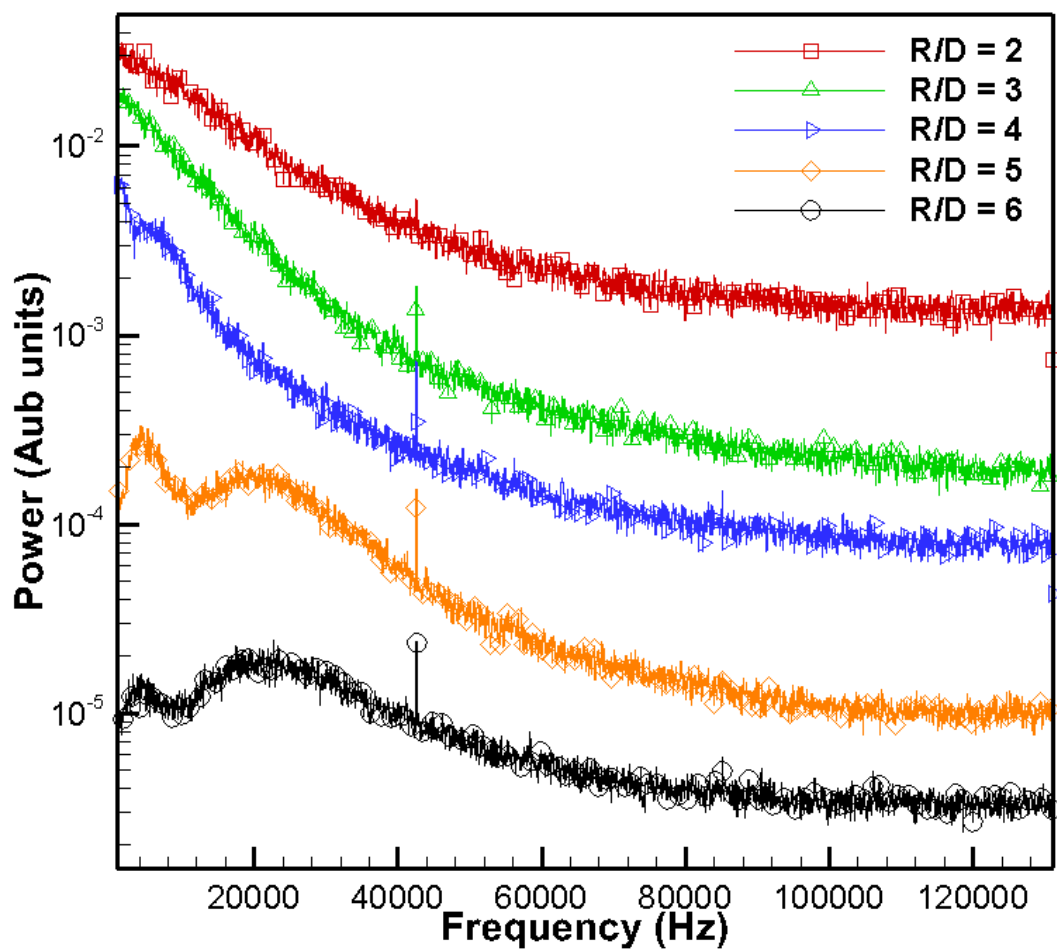


Figure 4.29 Frequency spectrum at  $Z/D = 25$

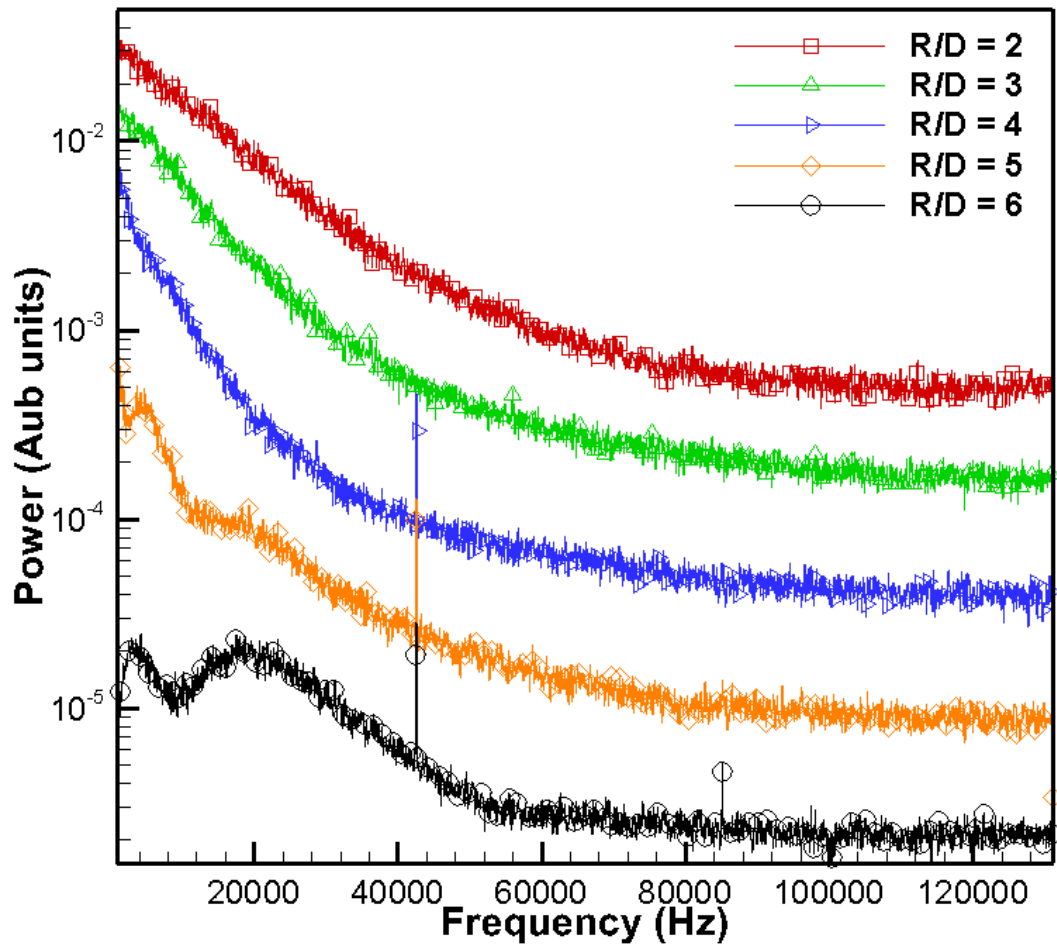


Figure 4.30 Frequency spectrum at  $Z/D = 27.5$

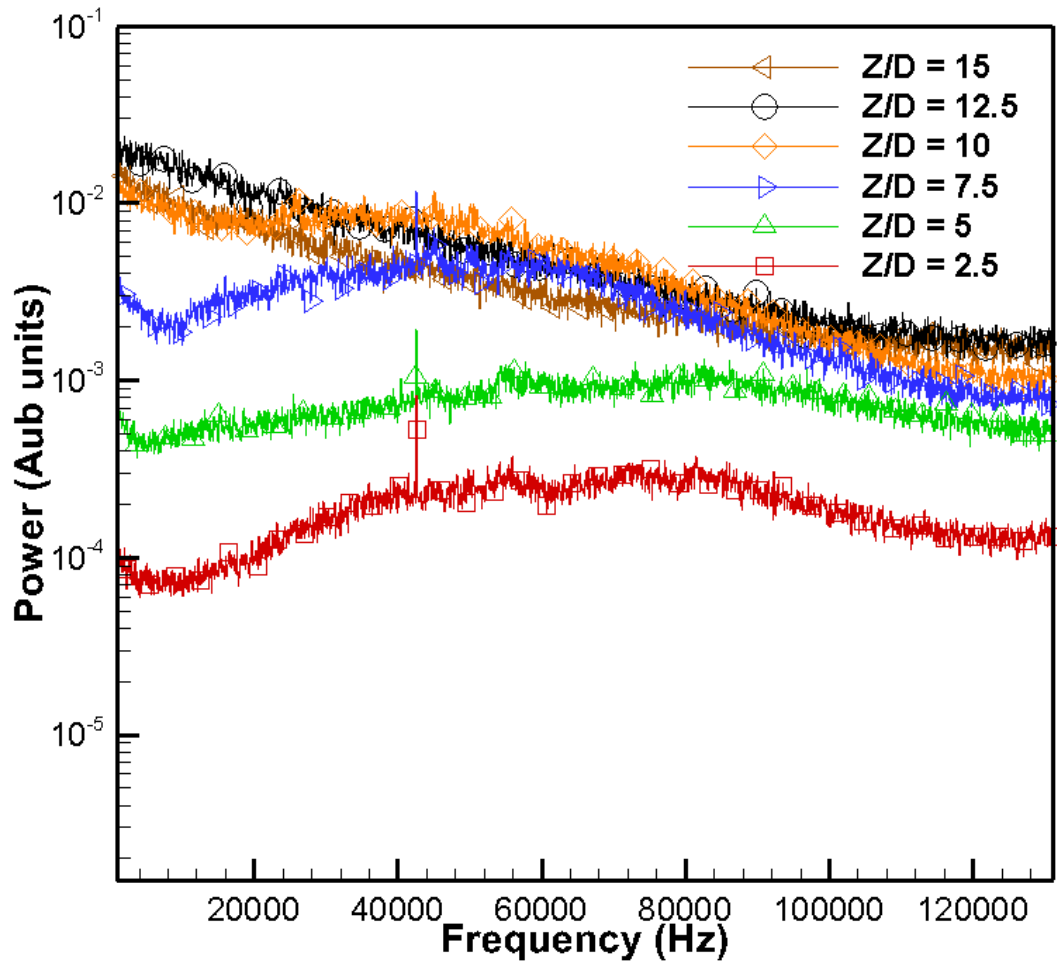


Figure 4.31 Frequency spectrum at  $R/D = 1.5$  for  $Z/D = 2.5$  to 15.

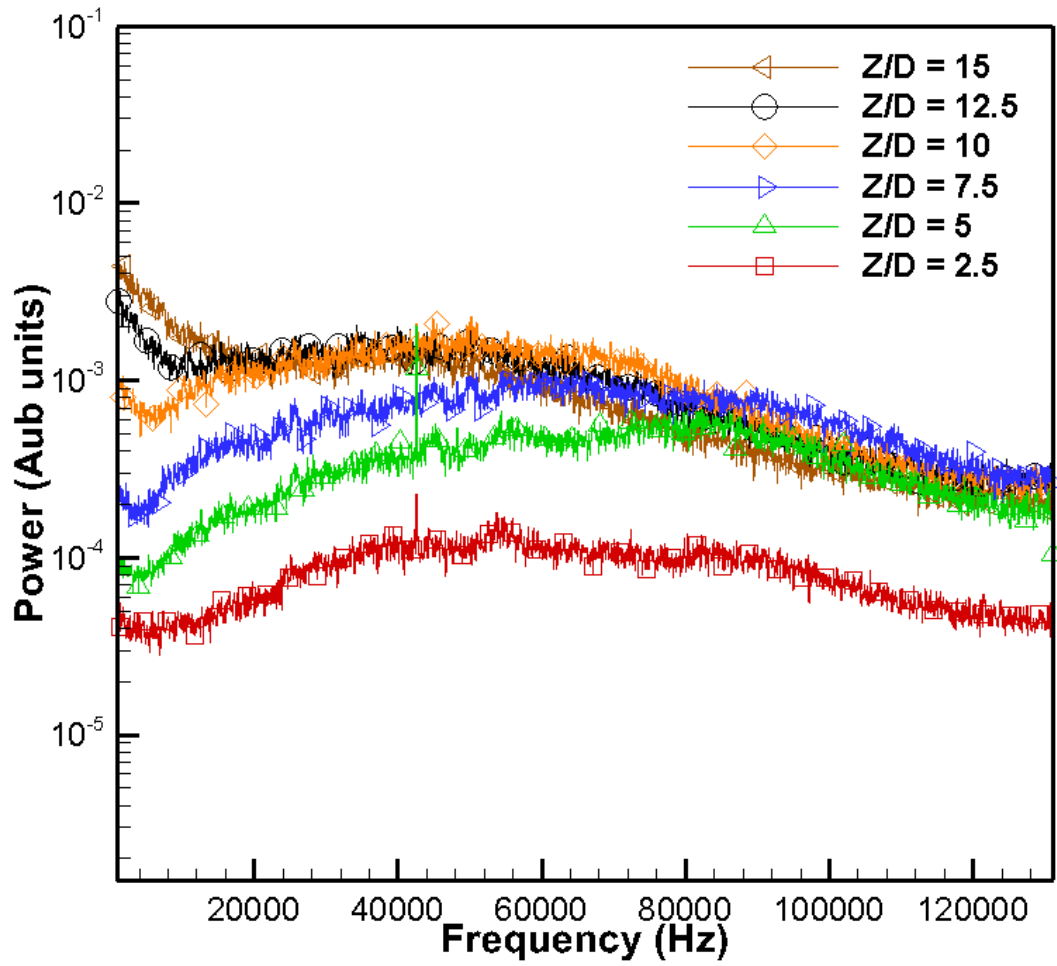


Figure 4.32 Frequency spectrum at  $R/D = 2$  for  $Z/D = 2.5$  to 15.

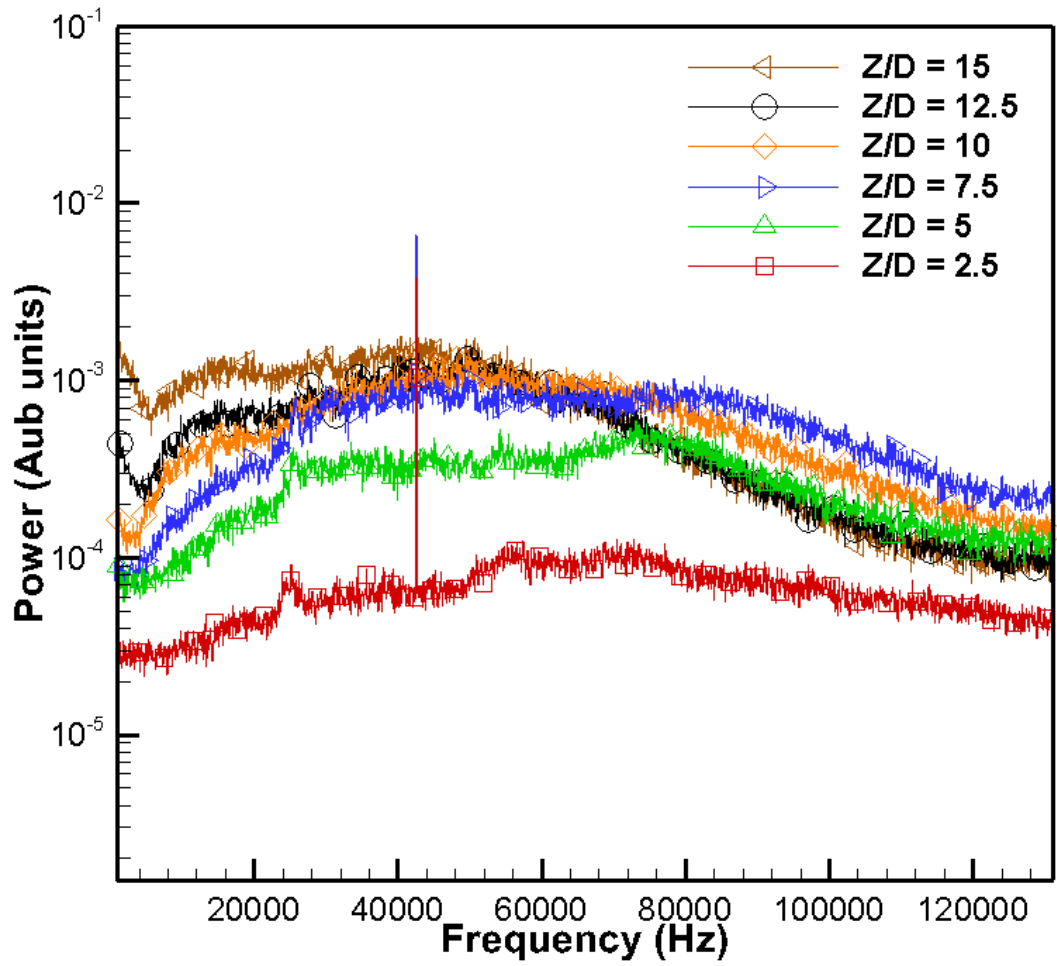


Figure 4.33 Frequency spectrum at  $R/D = 2.5$  for  $Z/D = 2.5$  to 15.

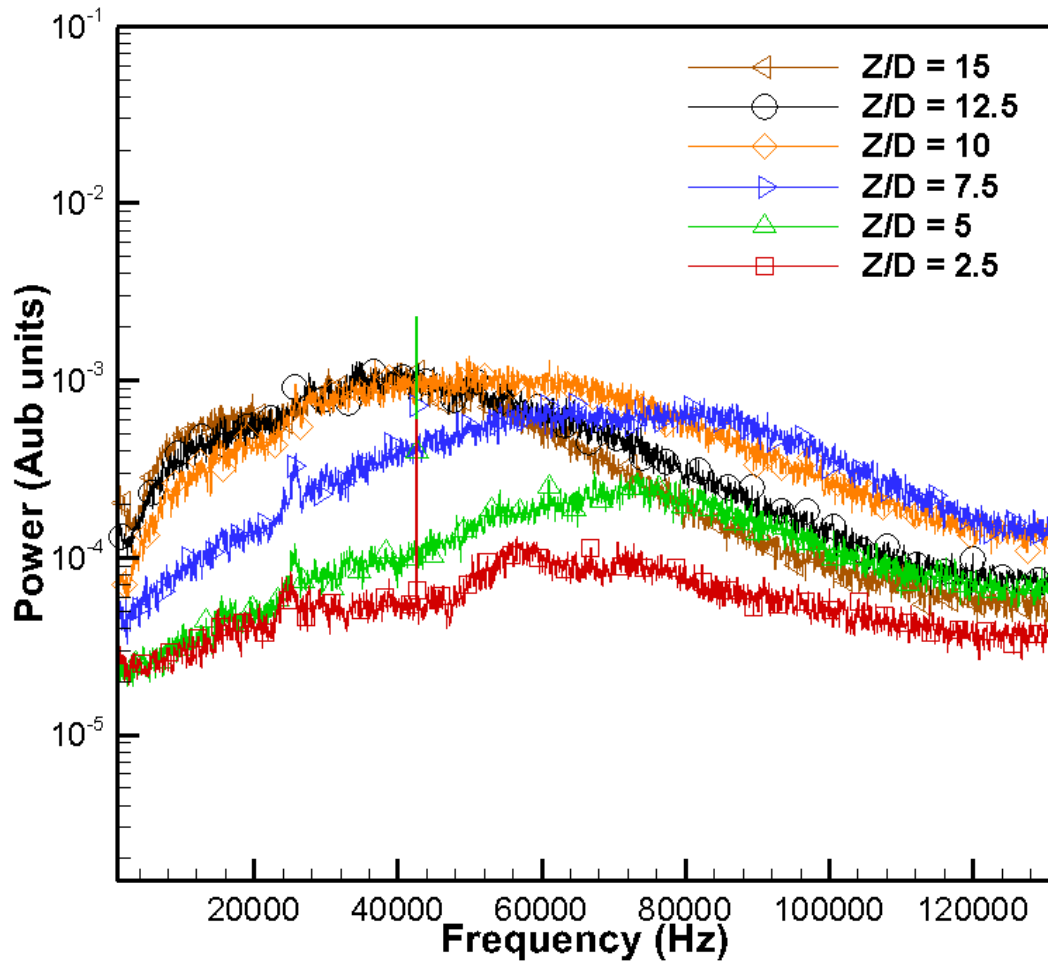


Figure 4.34 Frequency spectrum at  $R/D = 3$  for  $Z/D = 2.5$  to 15.

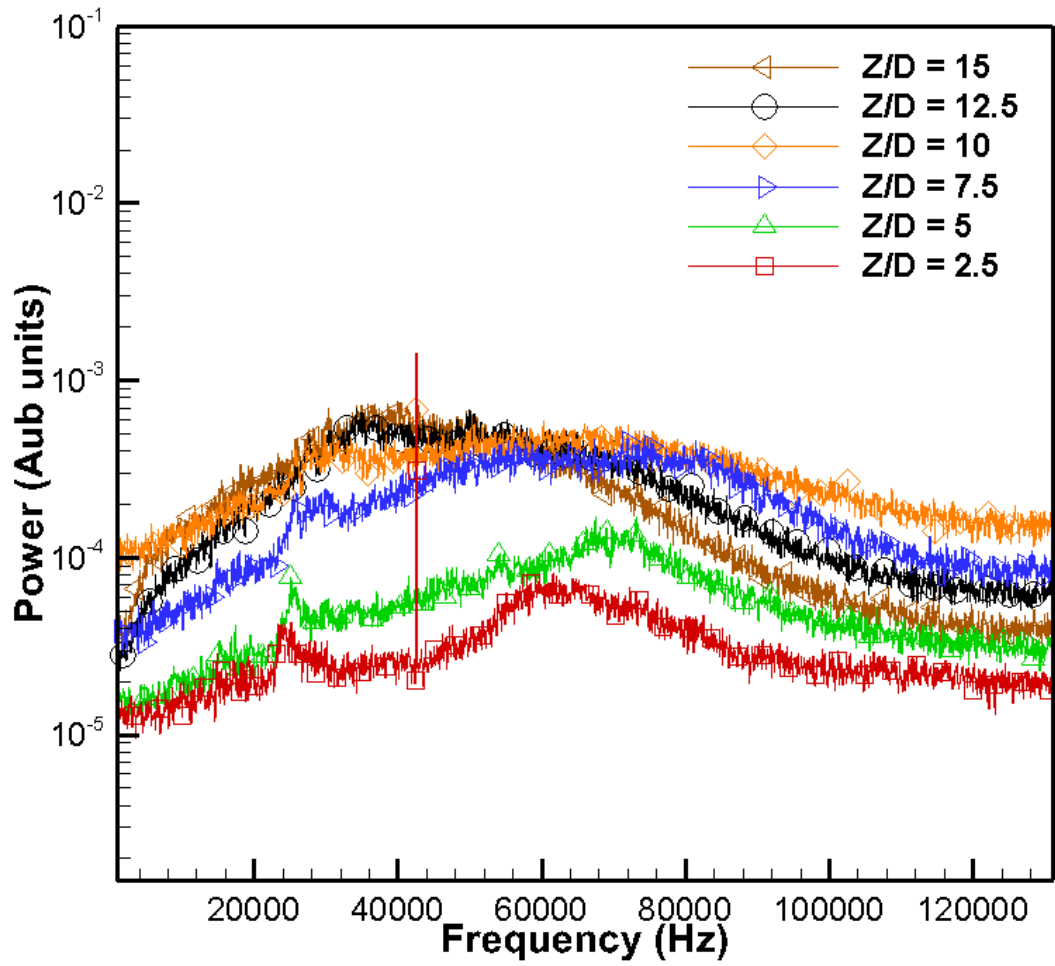


Figure 4.35 Frequency spectrum at  $R/D = 4$  for  $Z/D = 2.5$  to 15.

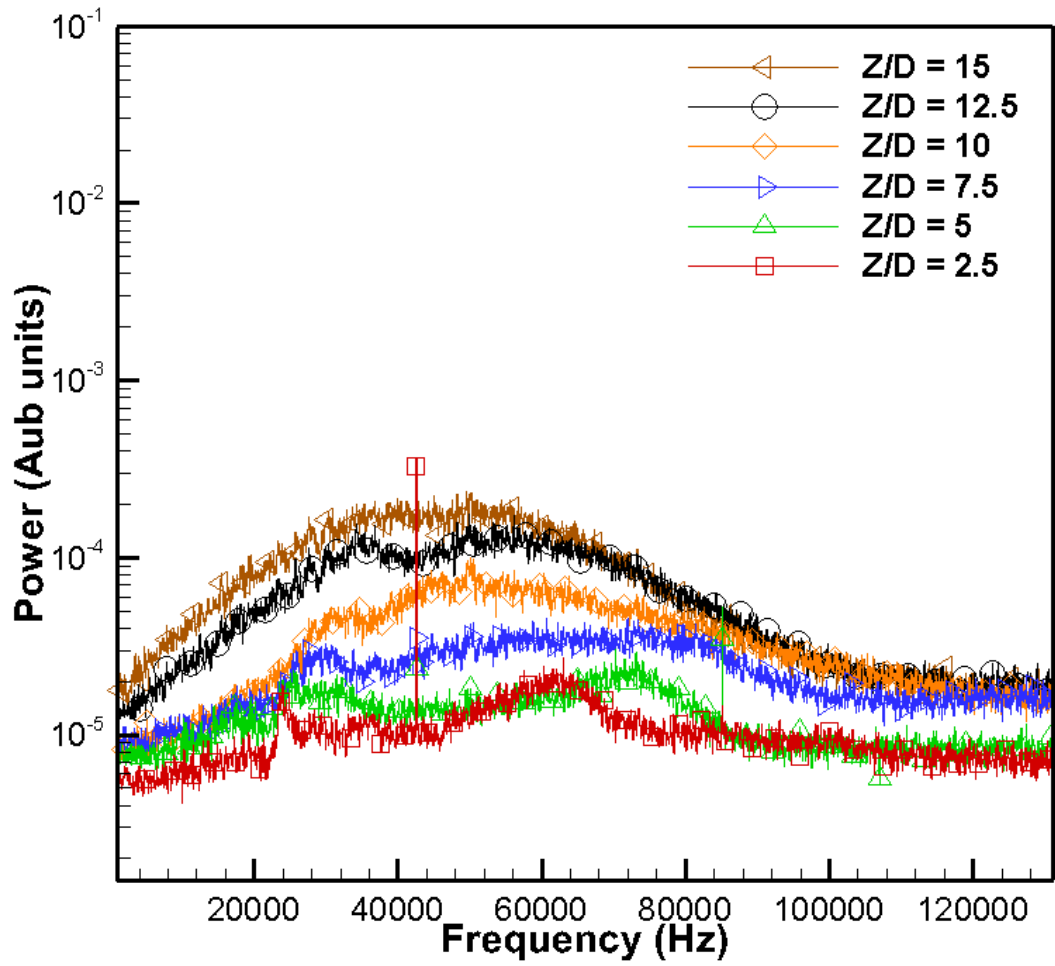


Figure 4.36 Frequency spectrum at  $R/D = 5$  for  $Z/D = 2.5$  to 15.

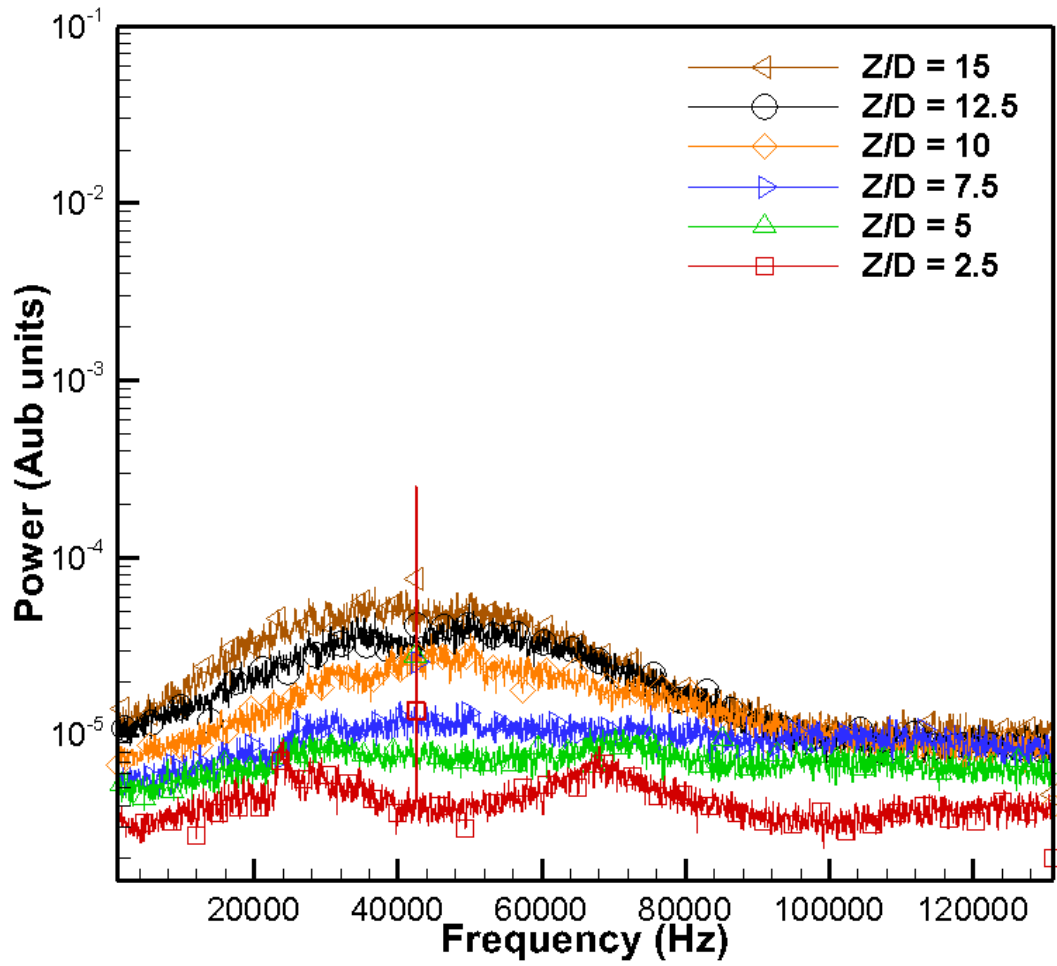


Figure 4.37 Frequency spectrum at  $R/D = 5.5$  for  $Z/D = 2.5$  to 15.

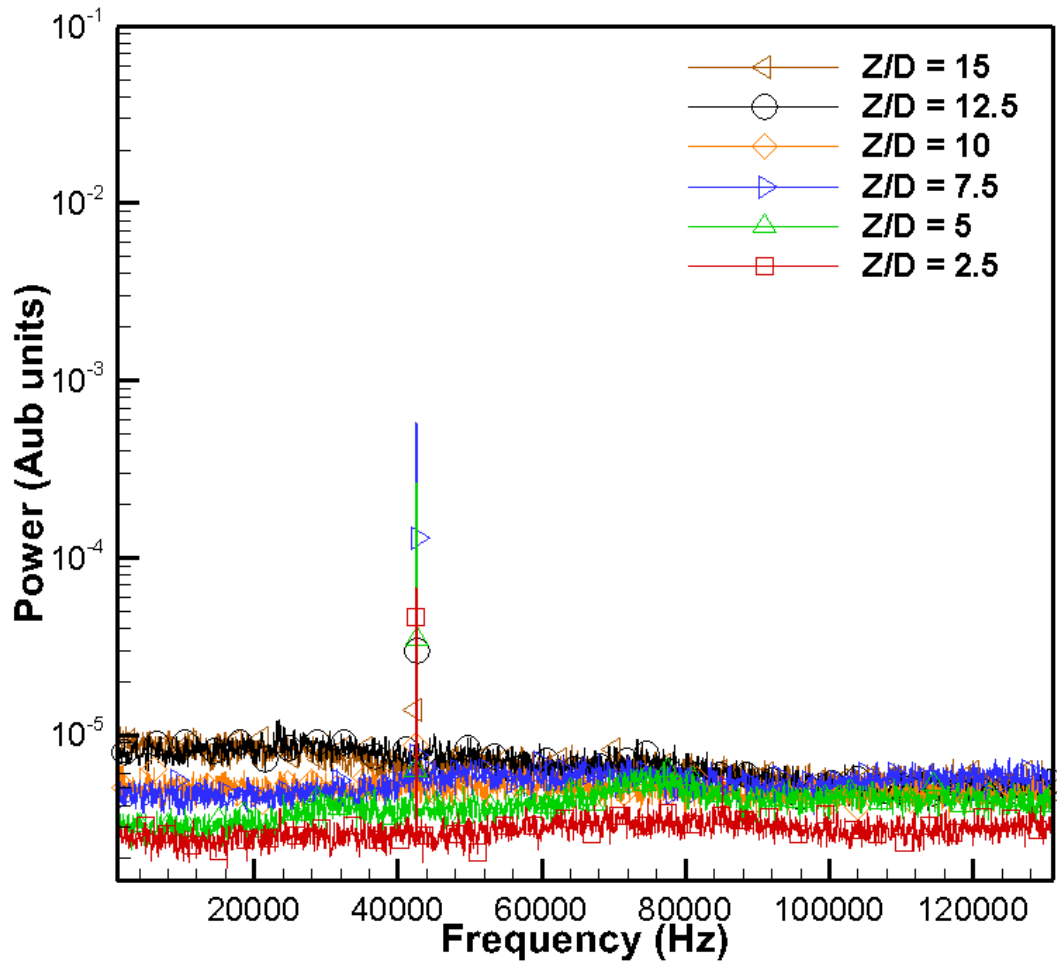


Figure 4.38 Frequency spectrum at  $R/D = 6$  for  $Z/D = 2.5$  to 15.

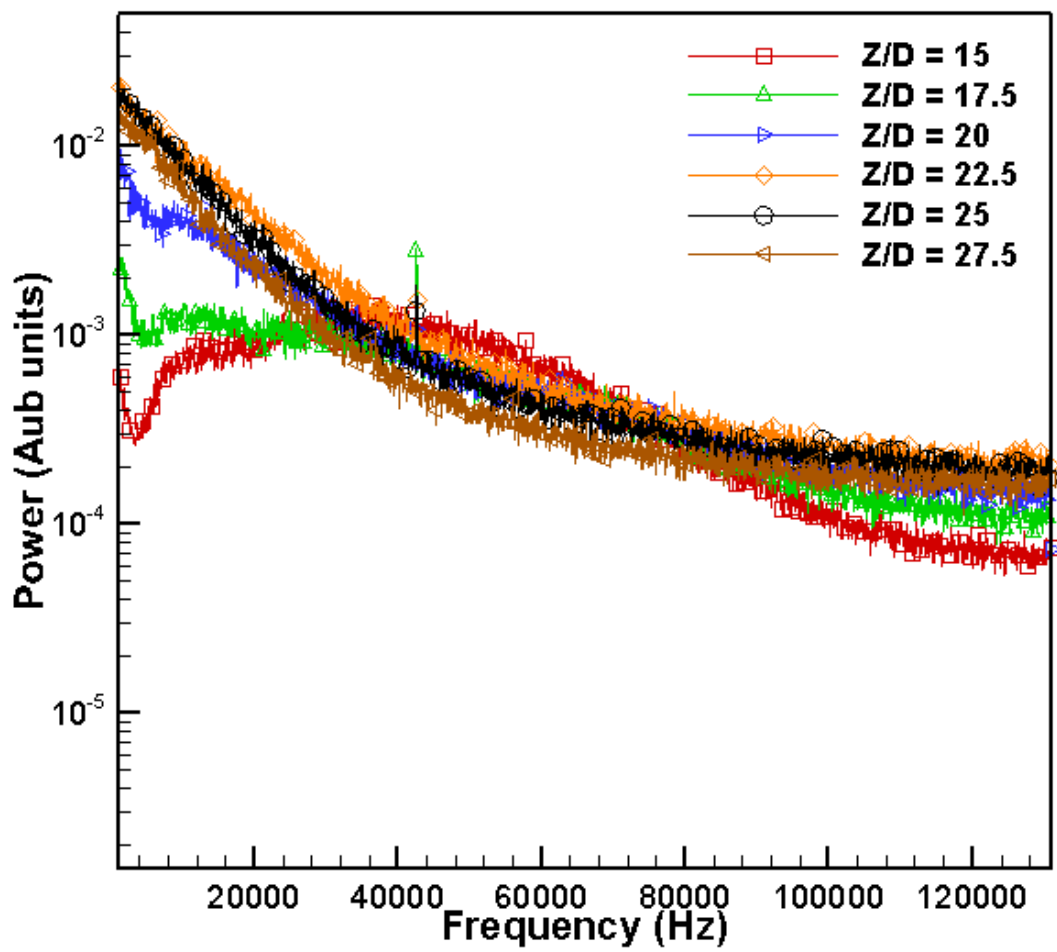


Figure 4.39 Frequency spectrum at  $R/D = 3$  for  $Z/D = 15$  to  $27.5$ .

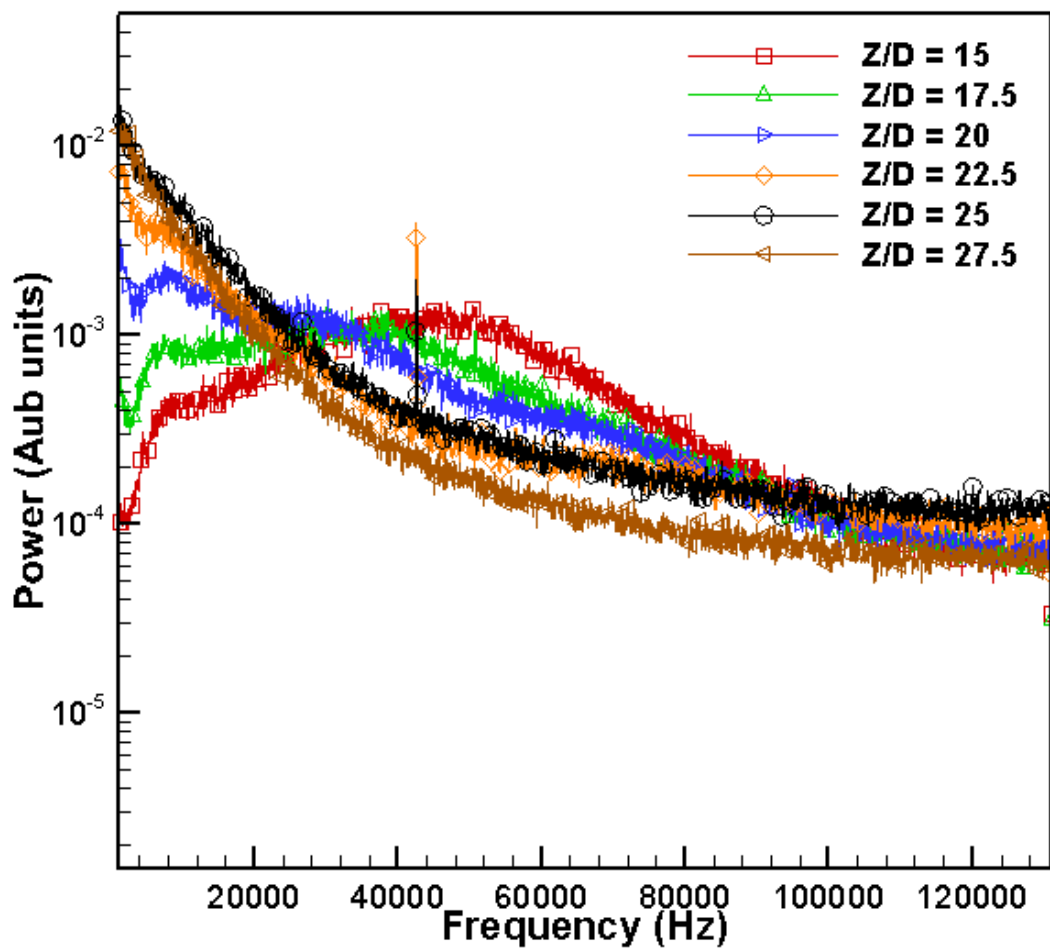


Figure 4.40 Frequency spectrum at  $R/D = 3.5$  for  $Z/D = 15$  to  $27.5$ .

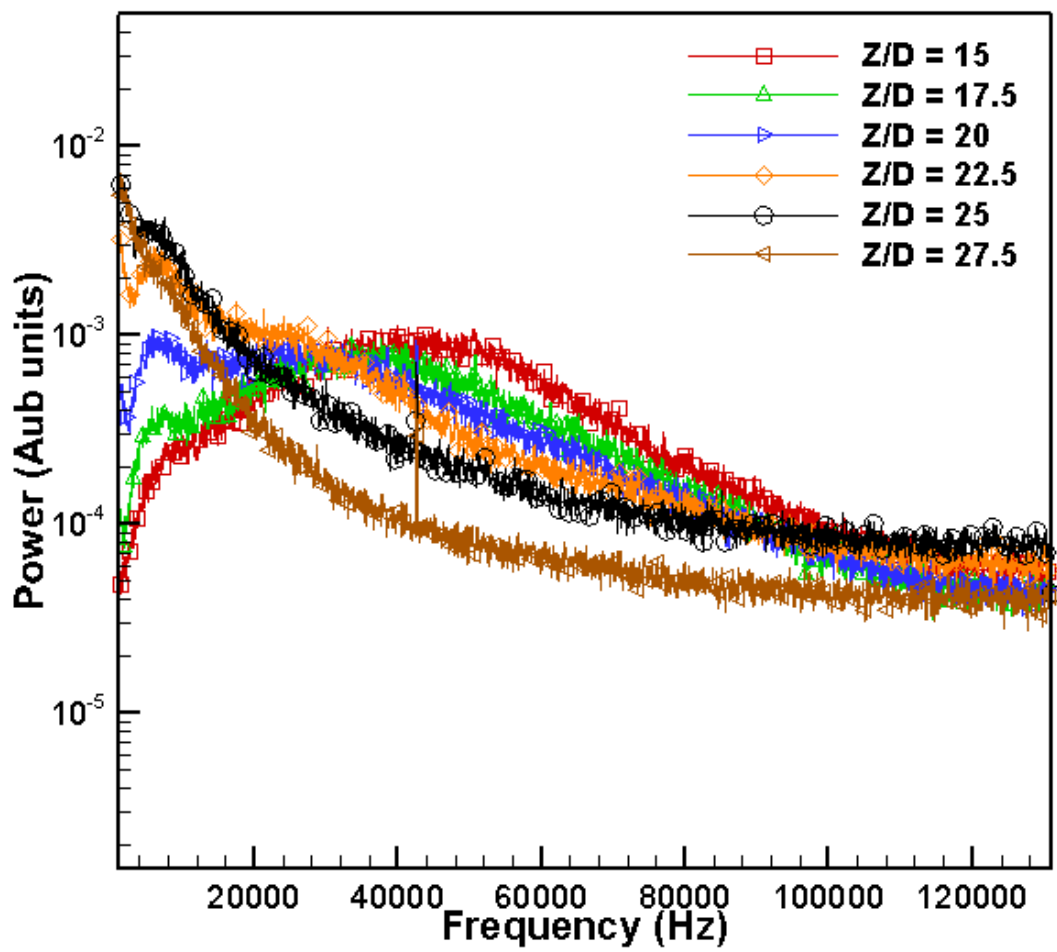


Figure 4.41 Frequency spectrum at  $R/D = 4$  for  $Z/D = 15$  to  $27.5$ .

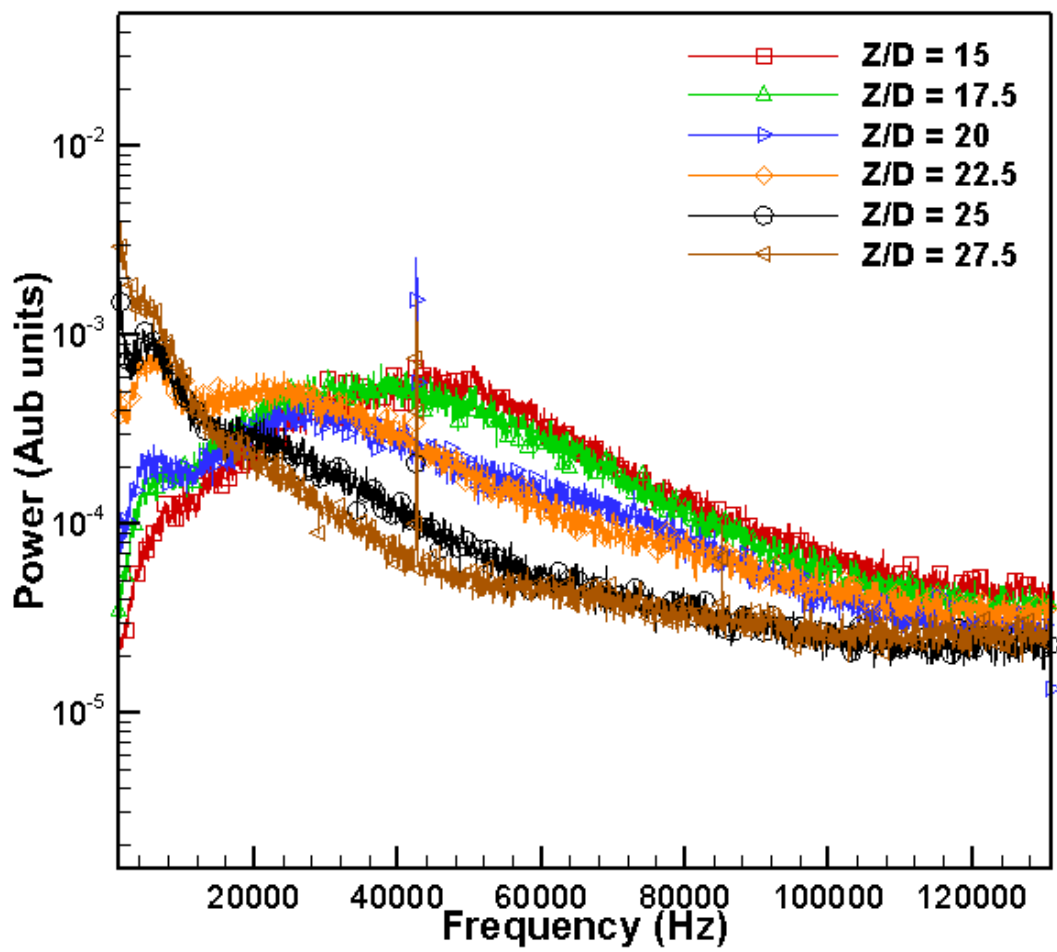


Figure 4.42 Frequency spectrum at  $R/D = 4.5$  for  $Z/D = 15$  to  $27.5$ .

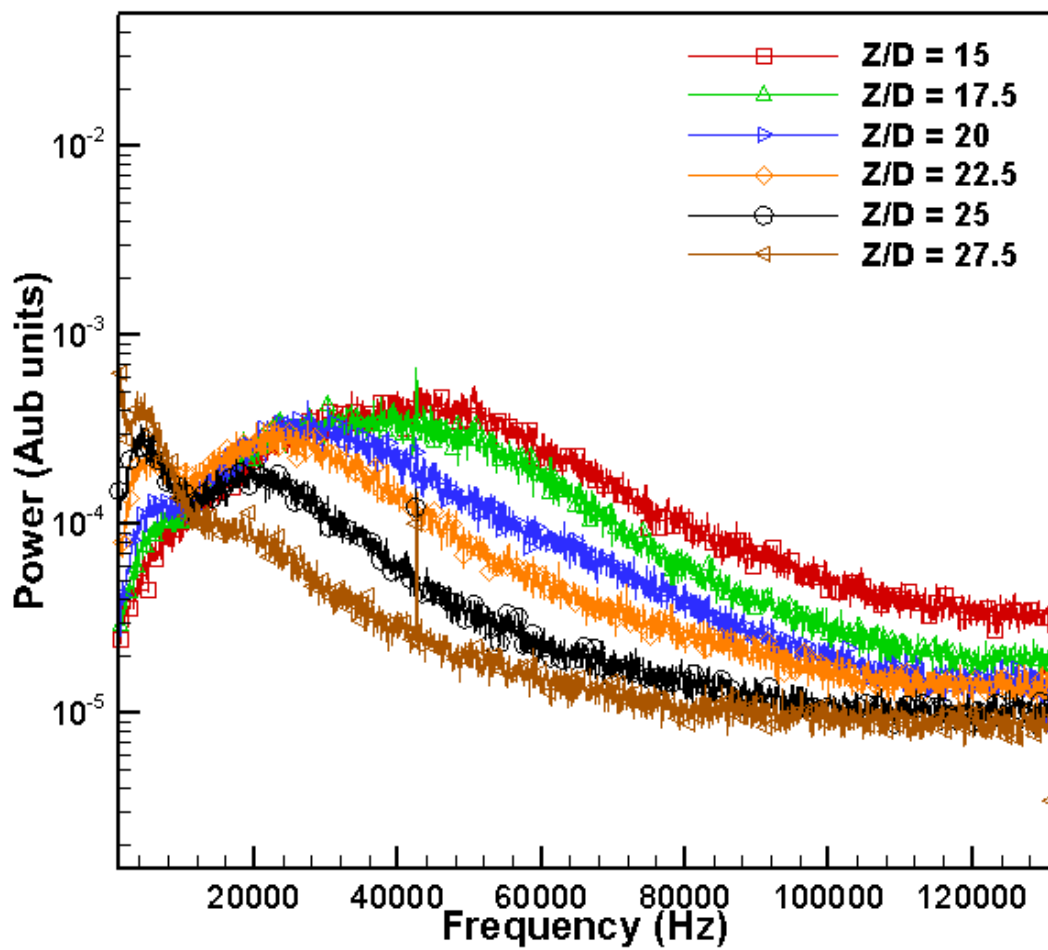


Figure 4.43 Frequency spectrum at R/D = 5 for Z/D = 15 to 27.5.

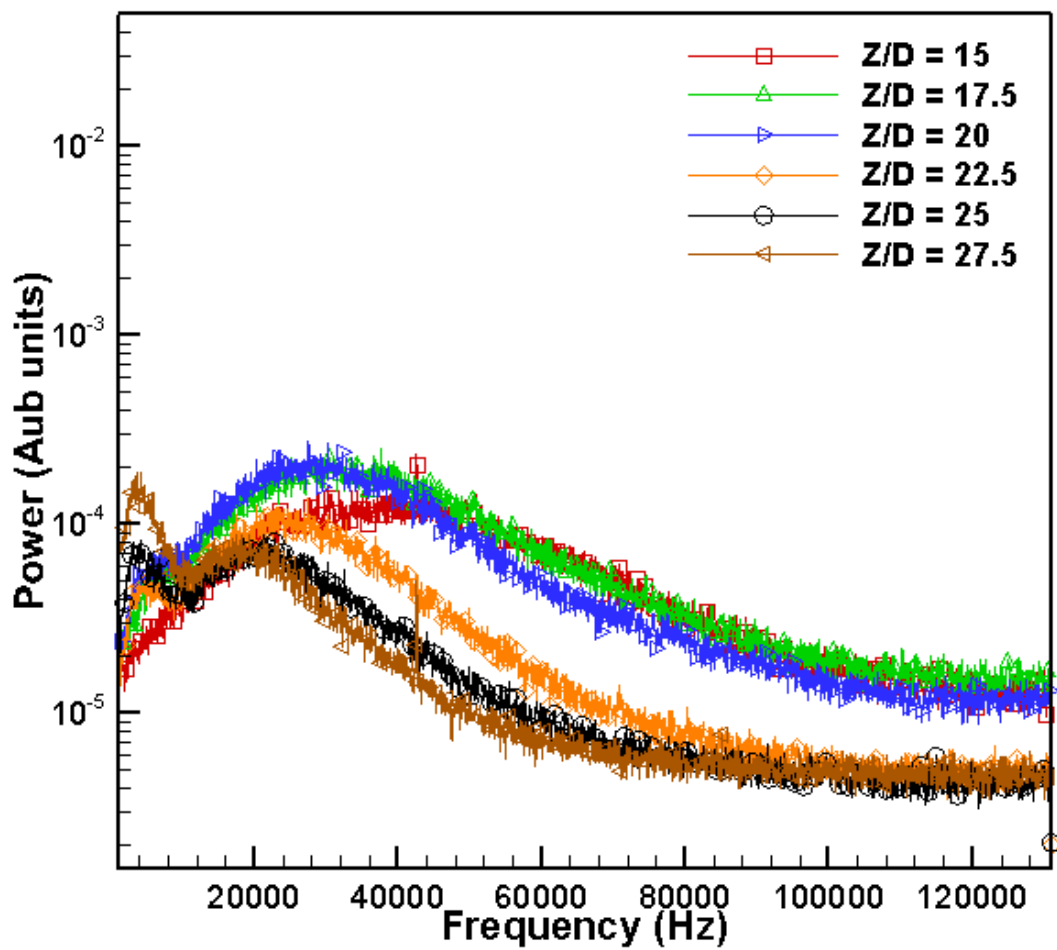


Figure 4.44 Frequency spectrum at  $R/D = 5.5$  for  $Z/D = 15$  to 27.5.

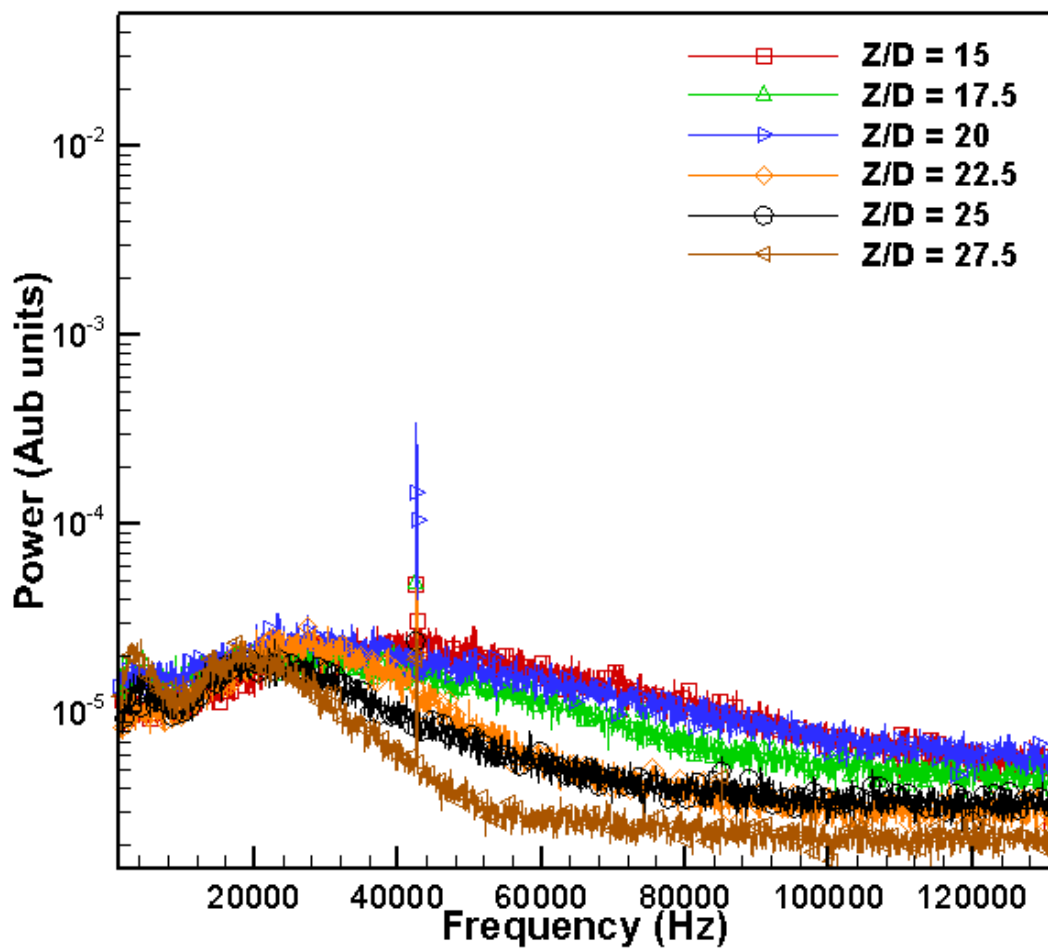


Figure 4.45 Frequency spectrum at  $R/D = 6$  for  $Z/D = 15$  to  $27.5$ .

## CHAPTER 5

### CONCLUSION AND RECOMMENDATIONS

#### Conclusion

A UHS-RSD system was developed to measure the density fluctuations that are produced as a supersonic cold air jet is expelled into ambient air. This technique allows the study of sound wave propagation produced from high speed jets. Measurements made by the aero-acoustic community support the direct visual representations of the flow field that are seen in captured image videos from the UHS-RSD technique. Mach waves that detected in several past experiments can be observed. These waves are characteristic of strong directional large turbulent effects and small scale turbulent broadband waves.

Initial analysis reveals the UHS-RSD system is detecting Mach waves that propagate out from a jet flow of convective Mach speed of 1.41. The waves are travelling at fixed Mach angles of 45 degrees from the flow field direction. It is also observed that wave fronts are being generated in small packets of two to ten waves with a small intermittency window.

Analysis of mean and standard deviation of hue difference allows for determination of radial range that signal noise is clear enough for detailed analysis. Results suggest that radial extent of  $R/D < 2$  is corrupted by jet flow and radial location of  $R/D > 6$  encounter high measurement noise to signal ratios and thus the noise floor is reached past these locations. Hue

difference data are consistent with measurements along the lipline of the jet flow by Veltin (2011).

Fast Fourier transform (FFT) analysis in the near field acoustic regime outside the jet flow field shows peak fluctuations in frequency range of 40,000 to 50,000 Hz contained in the acoustic signal. It is likely that these ultrasonic waves also have an audible acoustic component not observed visually. FFT analysis also shows strong correlations in power spectra density plots in overlapping radial directions compared with Veltin (2011).

This research has shown that the UHS-RSD technique offers the capability to measure acoustic waves emanating from supersonic jets in real time.

### Recommendations

This research involving an experimental study of acoustic waves provides a scope for several future improvements as listed below:

- The extent of the usable region of data is only from R/D of two to six. Future optimization of the experimental setup could extend this range, but would require higher quality optics and alignment.
- Past research has already shown turbulent shear layer in the flow field from R/D = 0 to 2. Future studies could measure both the jet flow field and the acoustic field simultaneously.
- Spectral analysis techniques need refinement to quantitatively analyze the acoustic field with poor signal to noise ratio.

- Cross correlation algorithms can be applied to track the acoustic wave propagation direction. Then the signal can be backtracked to relate the noise generation source and its effects on the acoustic field away from the flow field.
- Further work can seek to interpret the interference patterns between waves. This would aide in discovering wave interactions induced by turbulent flow fields.
- Finally, schlieren measurements can be correlated with sound probe measurements.

## REFERENCES

- [<sup>1</sup>] Lighthill, M. J. 1952 On sound generated aerodynamically: I. General theory. Proc. R. Soc. Lond. A 211, 564-581.
- [<sup>2</sup>] Davies, P. O. A. L., Fisher, M. J., and Barratt, M. J., "The Characteristics of the Turbulence in the Mixing Region of a Round Jet," *Journal of Fluid Mechanics*, Vol. 15, No. 3, 1963, pp. 337–367.
- [<sup>3</sup>] Bradshaw, P., Ferriss, D. H., and Johnson, R. F., "Turbulence in the Noise-Producing Region of a Circular Jet," *Journal of Fluid Mechanics*, Vol. 19, No. 4, 1964, pp. 591–624.
- [<sup>4</sup>] Crow, S. C., and Champagne, F. H., "Orderly Structure in Jet Turbulence," *Journal of Fluid Mechanics*, Vol. 48, No. 3, 1971, pp. 547–591.
- [<sup>5</sup>] Tam C. K. W., Viswanathan K., Ahuja K. K., and Panda J, 2008, "The sources of jet noise: experimental evidence," *J. Fluid Mech.*, 615, 253–292.
- [<sup>6</sup>] Panda, J., Seasholtz, R. G., and Elam, K. A., 2005, "Investigation of Noise Sources in High-Speed Jets via Correlation Measurements," *J. Fluid Mech*, 537(1), 349–385.
- [<sup>7</sup>] Panda, J., and Seasholtz, R. G., 2002, "Experimental Investigation of Density Fluctuations in High-Speed Jets and Correlation with Generated Noise," *J. Fluid Mech*, 450(1), 97–130.
- [<sup>8</sup>] McLaughlin, D. K., Morrison, G. L., and Troutt, T. R., "Experiments on the Instability Waves in a Supersonic Jet and Their Acoustic Radiation," *Journal of Fluid Mechanics*, Vol. 69, No. 1, 1975, pp. 73–85.
- [<sup>9</sup>] Troutt, T. R., and McLaughlin, D. K., "Experiments on the Flow and Acoustic Properties of a Moderate Reynolds-Number Supersonic Jet," *Journal of Fluid Mechanics*, Vol. 116, No. 1, 1982, pp. 123–156.
- [<sup>10</sup>] Lau, J. C., "Laser Velocimeter Correlation Measurements in Subsonic and Supersonic Jets," *Journal of Sound and Vibration*, Vol. 70, No. 1,
- [<sup>11</sup>] Kerhervé, F., Jordan, P., Gervais, Y., Valiere, J.-C., and Braud, P., "Two-Point Laser Doppler Velocimetry Measurements in a Mach 1.2 Cold Supersonic Jet for Statistical Aeroacoustic Source Model," *Experiments in Fluids*, Vol. 37, No. 2, 2004, pp. 419–437.

- [<sup>12</sup>] Bridges, J., “Effect of Heat on Space-Time Correlations in Jets,” AIAA Paper 2006-2534-924, 2006.
- [<sup>13</sup>] Kastner, J., Kim, J. H., and Samimy, M., “Correlation of Large Scale Structure Dynamics and Far-Field Radiated Noise in a Mach 0.9 Jet,” AIAA Paper 2007-830, 2007.
- [<sup>14</sup>] Seasholtz, R. G., Panda, J. & Elam, K. A., 2001, “Rayleigh scattering diagnostics for dynamic measurement of velocity fluctuations in high speed jets,” *AIAA Paper 2001-0847*.
- [<sup>15</sup>] Seasholtz, R. G., Panda, J. & Elam, K. A., 2002, “Rayleigh scattering diagnostics for measurement of velocity and density fluctuation spectra,” *AIAA Paper 2002-0827*.
- [<sup>16</sup>] Panda, J., and Seasholtz, R. G., 2002, “Experimental Investigation of Density Fluctuations in High-Speed Jets and Correlation with Generated Noise,” *J. Fluid Mech*, **450**(1), 97–130.
- [<sup>17</sup>] Panda, J., Seasholtz, R. G., and Elam, K. A., 2005, “Investigation of Noise Sources in High-Speed Jets via Correlation Measurements,” *J. Fluid Mech*, **537**(1), 349–385.
- [<sup>18</sup>] Doty, M. J., and McLaughlin, D. K., “Space Time Correlation Measurements of High-Speed Axisymmetric Jets Using Optical Deflectometry,” *Experiments in Fluids*, Vol. 38, No. 4, 2005, pp. 415– 425.
- [<sup>19</sup>] Papamoschou, D., Morris, P. J., and McLaughlin, D. K., “Beamformed Flow-Acoustic Correlations in High-Speed Jets,” AIAA Paper 2009- 3212, 2009.
- [<sup>20</sup>] Veltin J., Day B. J., and McLaughlin D. K., 2011, “Correlation of Flowfield and Acoustic Field Measurements in High-Speed Jets,” *AIAA Journal*, 49(1), 150-163.
- [<sup>21</sup>] Greenberg P. S, Klimek R. B., and Buchele D. R, 1995, “Quantitative rainbow schlieren deflectometry”, *Appl. Opt.*, 34, 3819-3822.
- [<sup>22</sup>] Agrawal, A. K., Albers, B. W., and Griffin, D. W., “Abel Inversion of Deflectometric Measurements in Dynamic Flows,” *Applied Optics*, Vol. 38, No. 15, 1999, pp. 3394–3398. doi:10.1364/AO.38.003394
- [<sup>23</sup>] Greenberg, P. S., Klimek, R. B., and Buchele, D. R., “Quantitative Rainbow Schlieren Deflectometry,” *Applied Optics*, Vol. 34, No. 19, 1995, pp. 3810–3822.
- [<sup>24</sup>] Agrawal, A. K., Albers, B. W., “schlieren analysis of an oscillating gas jet diffusion flame” *Combustion and Flame*, 119:84-94,1999, The Combustion Institute.
- [<sup>25</sup>] Agrawal, A. K., Alammar, K. N., and Gollahalli, S. R., “Application of rainbow schlieren Deflectometry to measure temperature and oxygen concentration in laminar gas-jet diffusion flame”, *Experiments in Fluids*, Vol 32, 2002, pp. 689-691.

- [<sup>26</sup>] Agrawal, A. K., Wong, T., “Quantitative measurements in an unsteady flame using high-speed rainbow schlieren deflectometry”, *Measurement Science and Technology*, Vol 17, 2006, pp. 1503-1510.
- [<sup>27</sup>] Kolhe P. S., 2009, “Statistical Tomography for Scalar Turbulence Measurements Using Line of Sight Optical Techniques”, PhD. Dissertation, University of Alabama, Tuscaloosa Alabama.
- [<sup>28</sup>] Kolhe P. S., Agrawal A. K., 2009b, “Density measurements in a supersonic microjet using miniature rainbow schlieren deflectometry,” *AIAA Journal*, 47(4), 830-838.
- [<sup>29</sup>] Kolhe P. S., Agrawal A. K., 2010, “Investigation of the Cross-beam Correlation Algorithm to Reconstruct Local Field Statistics from Line-of-sight Measurements in Turbulent Flows”, *Flow Turbulence Combustion*, Vol 84, 2010, pp. 617-638

## APPENDIX A

### MATLAB ALGORHYTHMS

#### Input File

```
function [inputFileName] = createInputFile()
%%
inputFileName = 'Input1.mat';

%% %%%%%%%%%%% Command Input %%%%%%%%%%%

%Image Pre-Processing
HueDifference = 0;
RefractiveIndexDifference = 0;

%Image Post-Processing
DownSampleImg = 1;

ApplyFilter = 0;

FFT = 1;
PowerLvl = 0;
Correlation = 0;
Coherence = 0;

%% %%%%%%%%%%% Image Pre-Processing Input %%%%%%%%%%%
%%
rawBkrDataFileName = 'rawBkrData.mat';
rawImgDataFileName = 'rawImgData.mat';
rawCalDataFileName = 'rawCalData.mat';

%% Image Info
imgName = 'Img_C001H001S0001/Img_C001H001S0001'; %ImgPath/BaseFileName
bkrName = 'Bkr_C001H001S0001/Bkr_C001H001S0001'; %BkrPath/BaseFileName
calName = 'Call/Call1'; %CalPath/BaseFileName

% Background Image Setup info
bkrsFrm = 1; %starting frame
bkrincFrm = 1; %frame increment
bkrnFrm = 35000; %number of frames
```

```

bkrsaveWin = 4096; % how many images to process at a time before saving into
% results
bkrnFrmWin = 8; % number of frame windows. ( note: saveWin*nFrmWin <= nFrms )

% Experimental Image Setup info
Fs = 262500; %framing rate
sFrm = 1; %starting frame
incFrm = 1; %frame increment
nFrm = 349269; %number of frames
saveWin = 4096; % how many images to process at a time before saving into
% results
nFrmWin = 64; % number of frame windows. ( note: saveWin*nFrmWin <= nFrms )

%% Image region of interest

sRow = 1; %inspection starting row of image
incRow = 1;
eRow = 128; %inspection ending row of image
nRow = eRow - sRow + 1;

sCol = 1; %inspection starting column of image
incCol = 1;
eCol = 128; %inspection ending column of image
nCol = eCol - sCol + 1;

%% %%%%%%%%%%%%%%% Image Post-Processing Input %%%%%%%%%%%%%%%
%%
caseFileName = 'Case1.mat';

%% Down Sampling input
nozzDia = 8; % nozzle diameter in pixels

sr = 127; % starting row
dr = -.5*nozzDia; % incremental row distance
nr = 30; % number of rows

sc = 120; % starting col
dc = -.5*nozzDia; % incremental col distance
nc = 25; % number of col

st = 1; % starting time
dt = 1; % incremental time
nt = 64; % number of time steps. ( note: saveWin*nt <= nFrms )

%% frequency high pass filter

Fst = 500; %(Hz) Freq at end of stopband
Fp = 750; %(Hz) Freq at start of passband
Ast = 120; %(units?) attenuation in stopband
Ap = 1; %amount of ripple in passband

%% Segmented FFT input

segWin = 4096;

```

```

ovrLap = 0.5;

%% corralation input

rI = 110; %start row for auto corralation
cI = 100; %start col for autocorrattation

%% %%%%%%%%%%%%%%%%%%%%%%%%%%%%%%%%%%%%%%%%% Save Inputs %%%%%%%%%%%%%%%%%%%%%%%%%%%%%%%%%%%%%%%%%

% pre-processing
save(inputFileName, 'inputFileName');
save(inputFileName, '-
append', 'HueDifference', 'RefractiveIndexDifference', 'DownSampleImg', 'ApplyFilter', 'FFT', 'PowerLvl', 'Correlation', 'Coherence');
save(inputFileName, '-
append', 'rawBkrDataFileName', 'rawImgDataFileName', 'rawCalDataFileName');
save(inputFileName, '-
append', 'imgName', 'bkrName', 'calName', 'Fs', 'sFrm', 'incFrm', 'nFrm', 'saveWin', 'nFrmWin');
save(inputFileName, '-
append', 'bkrsFrm', 'bkrincFrm', 'bkrnFrm', 'bkrsaveWin', 'bkrnFrmWin');
save(inputFileName, '-
append', 'sRow', 'incRow', 'eRow', 'nRow', 'sCol', 'incCol', 'eCol', 'nCol');

% post-processing
save(inputFileName, '-append', 'caseFileName');
save(inputFileName, '-append', 'sr', 'dr', 'nr', 'sc', 'dc', 'nc', 'st', 'dt', 'nt');
save(inputFileName, '-append', 'Fst', 'Fp', 'Ast', 'Ap');
save(inputFileName, '-append', 'segWin', 'ovrLap');
save(inputFileName, '-append', 'rI', 'cI')

end

```

## Main Code

```
function [] = Main()
%% %%%%%%%%%% Input File Setup %%%%%%%%%%
tStartSript = tic;
[inputFileName] = createInputFile();
fprintf('finished setupFiles \n')
load(inputFileName)

%% %%%%%%%%%% Image Pre-Processing %%%%%%%%%%
%%

if HueDifference == 1
    createRawBkrDataFile(inputFileName)
    createRawHueDiffDataFile(inputFileName)
    fprintf('Finished Pre-Processing Images to Obtain Hue Difference. \n')
    fprintf('Continuing to Post-Processing. \n')

elseif RefractiveIndexDifference == 1
    createRawBkrDataFile(inputFileName)
    % To Do % *****
    %createRawCalDataFile(inputFileName)
    %createRawRefIndexDiffDataFile(inputFileName)
    % *****
    fprintf('Finished Pre-Processing Images to Obtain Refractive Index
Difference. \n')
    fprintf('Continuing to Post-Processing. \n')

else
    fprintf('No Pre-Processing Options Selected. \n')
    fprintf('Continuing to Post-Processing. \n')
end

%% %%%%%%%%%% Image Post-Processing %%%%%%%%%%
%% Down Sample Data

if DownSampleImg == 1
    downSampleData(inputFileName)
    fprintf('Finished Down Sampling Data \n')
else
    fprintf('No Down Sampling Options Selected \n')
end

%% Apply Signal Filters

if ApplyFilter == 1
    filterSignalHighPass(inputFileName)
    fprintf('Finished High Pass Filtering of Data \n')
else
    fprintf('No Filtering Options Selected \n')
end
```

```

%% post process anaylsis

if FFT == 1
    calculateFFT(inputFileName)
    fprintf('Finished Calculating FFT \n')
else
    fprintf('No FFT Options Selected \n')
end

%% Power Level

if PowerLvl == 1
    % To Do *****
    %setupPowerLevel2(ImgInputFile1,caseFile1)
    fprintf('Finished Calculating Power Levels \n')
else
    fprintf('No Power Level Options Selected \n')
end

%% coorotation

if Correlation == 1
    % To Do *****
    %setupxcorr(ImgInputFile1,caseFile1)
    fprintf('Finished Calculating Correlations \n')
else
    fprintf('No Correlation Options Selected \n')
end

%% coherence

if Coherence == 1
    % To Do *****
    %setupCohere(ImgInputFile1,caseFile1)
    fprintf('Finished Calculating Coherence \n')
else
    fprintf('No Coherence Options Selected \n')
end

fprintf('Finished Running Main Script \n')

tElapsedScript = toc(tStartSript);
fprintf('Total time = %5.5g minutes \n',tElapsedScript/60)

end

%% %%%%%%%%%%%%%%% Script Support Functions %%%%%%%%%%%%%%%

```

```

%%

function [] = createRawBkrDataFile(inputFileName)
tic
%% Load Input File
load(inputFileName)

%% Initilize Image Data file

% Initilizes raw data file
ImgData = zeros(nRow, nCol, bkrsaveWin);
save(rawBkrDataFileName, 'ImgData')
matobj = matfile(rawBkrDataFileName, 'Writable', true);

% adds zero matrix data to create data location place holder
ifile = bkrsFrm;
while ifile - bkrsFrm + 1 <= bkrsaveWin*bkrnFrmWin
    matobj.ImgData(:, :, ifile:ifile+bkrsaveWin-1) = ImgData(:, :, :);
    ifile = ifile + bkrsaveWin;
end
clear ImgData
fprintf('Finished Background Initilazation\n')
toc

%% get Image Data

hueData = zeros(nRow, nCol, bkrsaveWin);
tic
ifile = bkrsFrm;
Win = 1;

while ifile - bkrsFrm + 1 <= bkrsaveWin*bkrnFrmWin
    for iWin = 1:bkrsaveWin % captures single segment (size = saveWin)
        if ifile < 10
            file = strcat(bkrName, '0000', int2str(ifile), '.tif');
        elseif (ifile >= 10) && (ifile < 100)
            file = strcat(bkrName, '000', int2str(ifile), '.tif');
        elseif (ifile >= 100) && (ifile < 1000)
            file = strcat(bkrName, '00', int2str(ifile), '.tif');
        elseif (ifile >= 1000) && (ifile < 10000)
            file = strcat(bkrName, '0', int2str(ifile), '.tif');
        elseif (ifile >= 10000) && (ifile < 100000)
            file = strcat(bkrName, '', int2str(ifile), '.tif');
        elseif (ifile >= 100000) && (ifile < 1000000)
            file = strcat(bkrName, int2str(ifile), '.tif');
        end
        [Img] = imread(file, 'tif', 'PixelRegion', {[sRow incRow eRow], [sCol
incCol eCol]});
        [Img] = rgb2hsv(Img);
        hueData(:, :, iWin) = 360.*Img(:, :, 1);
        ifile = ifile + 1;
    end
    fprintf('Working on Bkr Img frame %5.4g \n', ifile)
    matobj.ImgData(:, :, ifile - bkrsaveWin - bkrsFrm + 1: ifile - bkrsFrm) =
hueData(:, :, :);

```

```

    for rdx = 1:nRow
        for cdx = 1:nCol
            tempMeanData(rdx,cdx,Win) = mean(hueData(rdx,cdx,:),3);
            tempRmsData(rdx,cdx,Win) = rms(hueData(rdx,cdx,:),3);
            tempStdData(rdx,cdx,Win) = std(hueData(rdx,cdx,:),0,3);
        end
    end
    %A = tempMeanData(1:5,1:5,Win)
    %B = tempRmsData(1:5,1:5,Win)

    Win = Win + 1;

    fprintf('Finished Bkr Img frame %5.4g \n',ifile)
    toc
    tic
end

%% Calculate Mean and RMS of Data Set
Mean = zeros(nRow,nCol);
RMS = zeros(nRow,nCol);
STD = zeros(nRow,nCol);

for rdx = 1:nRow
    for cdx = 1:nCol
        Mean(rdx,cdx) = mean(tempMeanData(rdx,cdx,:),3);
        RMS(rdx,cdx) = rms(tempRmsData(rdx,cdx,:),3);
        STD(rdx,cdx) = mean(tempStdData(rdx,cdx,:),3);
    end
end

save(rawBkrDataFileName, '-append', 'RMS', 'Mean', 'STD')

fprintf('Finished get Bkr Data Routine \n')
end

function [] = createRawHueDiffDataFile(inputFileName)
tic
%% Load Input File
load(inputFileName)
load(rawBkrDataFileName, 'Mean')
bkrMean = Mean;
clear Mean
%% Initialize Image Data file

% Initializes raw data file
ImgData = zeros(nRow, nCol, saveWin);
save(rawImgDataFileName, 'ImgData')
matobj = matfile(rawImgDataFileName, 'Writable', true);

% adds zero matrix data to create data location place holder
ifile = sFrm;

```

```

while ifile - sFrm + 1 <= saveWin*nFrmWin
    matobj.ImgData(:,:,ifile:ifile+saveWin-1) = ImgData(:,:,:);
    ifile = ifile + saveWin;
end
clear ImgData
fprintf('Finished Img Initalazation\n')
toc

%% get Image Data

hueData = zeros(nRow,nCol,saveWin);
tic
ifile = sFrm;
Win = 1;

while ifile - sFrm + 1 <= saveWin*nFrmWin
    for iWin = 1:saveWin % captures single segment (size = saveWin)
        if ifile < 10
            file = strcat(imgName,'00000',int2str(ifile),'.tif');
        elseif (ifile >= 10)&&(ifile < 100)
            file = strcat(imgName,'0000',int2str(ifile),'.tif');
        elseif (ifile >= 100)&&(ifile < 1000)
            file = strcat(imgName,'000',int2str(ifile),'.tif');
        elseif (ifile >= 1000)&&(ifile < 10000)
            file = strcat(imgName,'00',int2str(ifile),'.tif');
        elseif (ifile >= 10000)&&(ifile < 100000)
            file = strcat(imgName,'0',int2str(ifile),'.tif');
        elseif (ifile >= 100000)&&(ifile < 1000000)
            file = strcat(imgName,int2str(ifile),'.tif');
        end
        [Img] = imread(file,'tif','PixelRegion', {[sRow incRow eRow], [sCol
incCol eCol]});
        [Img] = rgb2hsv(Img);
        hueData(:,:,iWin) = 360.*Img(:,:,1) - bkrMean;
        ifile = ifile + 1;
    end
    fprintf('Working on Img frame %5.4g \n',ifile)
    matobj.ImgData(:,:,ifile - saveWin - sFrm + 1: ifile - sFrm) =
hueData(:,:,:);

    for rdx = 1:nRow
        for cdx = 1:nCol
            tempMeanData(rdx,cdx,Win) = mean(hueData(rdx,cdx,:),3);
            tempRmsData(rdx,cdx,Win) = rms(hueData(rdx,cdx,:),3);
            tempStdData(rdx,cdx,Win) = std(hueData(rdx,cdx,:),0,3);
        end
    end

    Win = Win + 1;

    fprintf('Finished Img frame %5.4g \n',ifile)
    toc
    tic
end

```

```

%% Calculate Mean and RMS of Data Set
Mean = zeros(nRow,nCol);
RMS = zeros(nRow,nCol);
STD = zeros(nRow,nCol);

for rdx = 1:nRow
    for cdx = 1:nCol
        Mean(rdx,cdx) = mean(tempMeanData(rdx,cdx,:),3);
        RMS(rdx,cdx) = rms(tempRmsData(rdx,cdx,:),3);
        STD(rdx,cdx) = mean(tempStdData(rdx,cdx,:),3);
    end
end

save(rawImgDataFileName, '-append', 'RMS', 'Mean', 'STD')

fprintf('Finished get Img Data Routine \n')

end

function [] = downSampleData(inputFileName)
%% Input Data

load(inputFileName)
tic

%% Initilize Image Data file
sampleData = zeros(nr,nc,saveWin);
save(caseFileName, 'sampleData')
matobjRaw = matfile(rawImgDataFileName);
matobjCase = matfile(caseFileName, 'Writable', true);

ifile = 1;
while ifile <= saveWin*nt
    matobjCase.sampleData(:, :, ifile:ifile+saveWin-1) = sampleData(:, :, :);
    ifile = ifile + saveWin;
end
fprintf('Finished Initilazation of Segments. \n')
toc

%% Start main code
tData = zeros(nRow,nCol,saveWin);
tic

%hueData = zeros(nRow,nCol,saveWin);
sWin = 1;
while sWin <= saveWin*nt
    tData(:, :, 1:saveWin) = matobjRaw.ImgData(:, :, sWin:sWin+saveWin-1);
    for iWin = 1:saveWin
        for rdx = 1:nr
            for cdx = 1:nc
                sampleData(rdx,cdx,iWin) = tData(sr+(rdx-1)*dr,sc+(cdx-
1)*dc,iWin);
            end
        end
    end
end

```

```

        end
    end
    sWin = sWin + 1;
end

matobjCase.sampleData(:, :, sWin-saveWin:sWin-1) = sampleData(:, :, :);
fprintf('Finished transfer sWin = %5.5g \n', sWin)
toc
tic
end

end

```

```

function [] = filterSignalHighPass(inputFileName)

load(inputFileName)
tic

matobj = matfile(caseFileName, 'Writable', true);
sampleData = matobj.sampleData;
[nR, nC, nT] = size(sampleData);
% Fst = (Hz) Freq at end of stopband
% Fp = (Hz) Freq at start of passband
% Ast = (units?) attenuation in stopband
% Ap = amount of ripple in passband

d = fdesign.highpass('Fst,Fp,Ast,Ap', Fst, Fp, Ast, Ap, Fs);

Hd = design(d, 'equiripple');

%FilterParameters = [Fst,Fp,Ast,Ap,Fs];

%% Old Method (omitted)
%fcutoff=500; %Hz
% ns = round(fcutoff*2*nFrm/Fs);
% ne = nFrm - ns + 1;
% %sampleData = zeros(nR,nC,nT);
% for rdx = 1:nR
%     for cdx = 1:nC
% a = fft(sampleData(rdx,cdx,:));
% b = reshape(a,nT,1);
% b(1:ns) = 0;
% b(ne:nFrm) = 0;
% sampleData(rdx,cdx,:) = real(ifft(b));
%     end
% end
% save(caseFile, '-append', 'sampleData')

%% New Method
for rdx = 1:nR

```

```

    for cdx = 1:nC

        sampleData(rdx,cdx,:) = filter(Hd,sampleData(rdx,cdx,:));

    end
end
save(caseFileName,'-append','sampleData')

end

function [] = calculateFFT(inputFileName)
%% Input Data
load(inputFileName)

matobj = matfile(caseFileName,'Writable',true);
Data = matobj.sampleData;
[nR,nC,nT] = size(Data);
FFT = zeros(nR,nC,(2^nextpow2(nT))/2 + 1);
segFFT = zeros(nR,nC,(2^nextpow2(nT))/2 + 1);
for rdx = 1:nR
    tic
    for cdx = 1:nC

        %[FFT(rdx,cdx,:)] = getFFT(Data(rdx,cdx,:),inputFileName);
        % old metoid omitted
        [Pxx(rdx,cdx,:),F(rdx,cdx,:)] =
getSegFFT(Data(rdx,cdx,:),inputFileName);

    end
    fprintf('Finished fft loop for row number = %3.3g out of %3.3g
\n',rdx,nR)
    toc
    tic
end
save(caseFileName,'-append','Pxx','F')
clear FFT segFFT

end
function [fftRes] = getFFT(Data,inputFileName)

load(inputFileName);

NFFT = 2^nextpow2(saveWin*nFrmWin);
%nFrm
 %[nR,nC,nT] = size(Data)
Data = reshape(Data,saveWin*nFrmWin,1);
fftRes = fft(Data(:,1),NFFT)/nFrm;
fftRes = 2*abs(fftRes(1:NFFT/2+1)).^2;
fftRes = reshape(fftRes,1,1,NFFT/2+1);

```

```
end
function [Pxx,F] = getSegFFT(Data,inputFileName)

load(inputFileName);
NFFT = 2^nextpow2(saveWin*nFrmWin);
Data = reshape(Data,saveWin*nFrmWin,1);
[Pxx,F] =
pwelch(Data,segWin,ovrLap*segWin,length(Data),saveWin*nFrmWin,'onesided');
[A,B] = size(Pxx);
Pxx = reshape(Pxx,1,1,A);
F = reshape(F,1,1,A);

end
```

## APPENDIX B

For sound pressure decibel level of 150 the fluctuations in pressure can be estimated using

$$150 = 20 \cdot \log_{10} \left( \frac{P_{rms}}{P_{ref}} \right)$$
$$\Rightarrow P' = P_{ref} \times 10^{\left(\frac{150}{20}\right)} = 2 \times 10^{-5} \times 10^{7.5} = 632.455 \text{ N/m}^2$$

Now, refractive index difference is given by  $\delta = \kappa \cdot \frac{P}{RT}$

$$\delta = \kappa \cdot \frac{P}{RT} = 2.3 \times 10^{-3} \cdot \frac{101325}{287 \times 288} = 2.8195 \times 10^{-4}$$

So estimating fluctuations for refractive index difference for air at ambient conditions (or STP) as follows.

$$\delta' = \kappa \cdot \frac{P'}{RT} = 2.3 \times 10^{-3} \cdot \frac{632.455}{287 \times 288} = 1.76 \times 10^{-6}$$

For 150 decibel 0.624 % change is caused in the refractive index difference.